DISSERTATION

MICROPHYSICAL RETRIEVAL IN SEVERE STORMS FROM GROUND-BASED AND SPACE-BORNE RADAR NETWORK: APPLICATION TO LA PLATA REGION IN SOUTH AMERICA

Submitted by

Iván D. Arias Hernández

Department of Electrical and Computer Engineering

In partial fulfillment of the requirements

For the Degree of Doctor of Philosophy

Colorado State University

Fort Collins, Colorado

Fall 2023

Doctoral Committee:

Advisor: V. Chandrasekar

Margaret Cheney
Indrakshi Ray
José Chávez

ABSTRACT

MICROPHYSICAL RETRIEVAL IN SEVERE STORMS FROM GROUND-BASED AND SPACE-BORNE RADAR NETWORK: APPLICATION TO LA PLATA REGION IN SOUTH AMERICA

The microphysics of severe weather is studied using a network approach from multiple platform observations. Observations acquired near the foothills of the Andes in Argentina are used in this investigation. La Plata region in Argentina is known for having some of the tallest storms on Earth. During the Austral summer of 2018, a network of radars was deployed in this region to study these storms as part of the RELAMPAGO field experiment. This network of ground-based radars, in addition to satellite and in-situ observations, is used to understand the microphysics of severe storms in this part of the world. The knowledge gained from studying the microphysics of these storms in South America is applied to understand convection more broadly. In addition, these multiple platform observations are used to understand how the storms in South America may differ from storms in other regions. The analysis from simultaneous radar observations is used to self-calibrate the radar network.

In this investigation, first, an extensive calibration of the radar network measurements was performed to obtain high-quality data for this study. The ground-based radars' dual-polarization measurements were calibrated using a network-based approach. In addition, satellite measurements from GPM radar were used as a common platform for calibrating the ground-based radars in the network. A new parameterization for the attenuation correction is developed for ground-based radar in this region as an outcome of the network calibration exercise. After careful calibration, the radar measurements in the network were used to obtain observational statistics over the RELAMPAGO campaign domain. These statistics are applied to understand the connection between the radar retrievals and to select the severe weather cases to study.

For the severe weather cases identified in the radar statistics, spectral polarimetric decomposition from radar signal samples in updraft environments is derived. First, updrafts are identified using dual Doppler analysis. Subsequently, the reflectivity, differential reflectivity, and coherence spectra are computed from radar signal samples. Practical considerations about the computation of the spectrum in updraft are also presented. The spectral analysis revealed that bimodalities in the spectrum can be found in updraft conditions. In addition, a technique to quantify the attenuation of C-band radar signals in melting ice was developed using multiple radar observations. The attenuation estimates are used to parameterize the specific attenuation in melting ice to explain the enhanced attenuation. Finally, convective permitting high-resolution simulations are compared with the radar network observations for a representative severe weather case. This comparison is conducted to test the effectiveness of downscaling to resolve better convective processes that lead to severe weather.

ACKNOWLEDGEMENTS

People and relationships are the most precious things one can have. During this part of my life, I crossed paths with many people that helped me to arrive at this point of finishing my Ph.D. I would need another chapter in this dissertation just to acknowledge all the people that made this achievement possible. I only mentioned a few of them in this acknowledgement but I also want to thank so many other people that supported and helped me in so many ways to complete my program. Gracias a todos!

First, I would like to express my deepest gratitude to my advisor, Prof. V. Chandrasekar, for all the support during my Ph.D. For providing the conditions and resources that allowed me to develop my whole potential as a graduate student. I would like to thank him for the encouragement and the critiques, for the flexibility and the firmness. For the agreement and the space to express my disagreement that always took us to a common place of mutual understanding. For giving me the freedom to start my own projects and develop my own ideas even though some of the time they did not take me to a final result. This freedom to explore and find myself as a scientist helped me to grow as a scientist and to build my academic career on more solid ground. Muchas gracias, Profesor!

I also would like to thank Dr. M. Cheney, Dr. I. Ray, and Dr. J. Chavez for their commitment to being part of my Ph.D. committee. I really appreciate their time to go through revisions, exams, and their feedback. I want to also thank other academic mentors that I found along the way. I would like to thank Dr. K. Rasmussen and Dr. T. Weckwerth for guiding me in expanding my research scope and their career path advice. I would also like to thank Patrick Kennedy for the coffee meetings we had throughout my Ph.D. and for his easy way of explaining fundamental concepts. Having a basic understanding of what one is studying is the basis to build up solid science. Thanks, Pat.

Pursuing graduate studies far from home is not easy and it takes international students extra energy and effort to pursue a degree in a different country and language. I would like to thank

my friends, lab mates, and the Latin community in Colorado who became my local family during my time away from home. For the great support they gave me when I was sick, or down, or just needed to hang out with friends. I would also like to thank the staff in the LSC and the dining hall that sent me home with an extra portion of food. Gracias!

I would also like to give thanks to my family, my mother Sofia, my father Carlos, and my brother Carlitos for all their love that they gave me during my Ph.D. through video calls, sometimes every day, and for coming all the way from Colombia to Colorado every time I needed them for visiting, for medical procedures, and for my mental health. I also would like to thank Casey for all the love she gave me during the hardest part of my Ph.D. For reminding me to make time to have fun, and for always being there whenever I needed it, especially in the final part of my Ph.D while preparing for my defense, for being a great emotional support when things didn't go well or after a long day in the lab. Los quiero mucho!

Finally, I would like to thank the Fulbright program for opening to me the opportunity to pursue a graduate program in the U.S. and to the NSF that supported my research.

DEDICATION

I would like to dedicate this dissertation to my family and Casey.

TABLE OF CONTENTS

ABSTRACT ii
ACKNOWLEDGEMENTS iv
DEDICATION vi
LIST OF TABLES x
LIST OF FIGURES xi

Chapter 1 Introduction 1
1.1 Motivation 1
1.2 Statement of the Problem 3
1.3 Research Question 4
1.3.1 Main objective 5
1.3.2 Secondary Objective 5
1.4 Overview 5

Chapter 2 Background 6
2.1 Fundamentals of Radars 6
2.2 Precipitation Measurement 7
2.3 Attenuation Correction 9
2.4 Dual Doppler Analysis 11
2.5 Spectral decomposition 13
2.6 Large drops and C-band 14

Chapter 3 The RELAMPAGO experiment radar dataset 16
3.1 RELAMPAGO Overview 16
3.2 Radar calibration 19
3.2.1 Pointing angle calibration 19
3.2.2 Z_{dr} Bias correction 22
3.3 Radar Statistics 24

Chapter 4 Cross validation of the network of ground-based radar with space-borne radar during the RELAMPAGO field campaign 27
4.1 Introduction 28
4.2 The RELAMPAGO radar observation 29
4.2.1 The network of C-band radar 29
4.2.2 Attenuation correction for the ground radars 32
4.2.3 Overview of the GPM overpasses 33
4.3 Inter-comparison of the RELAMPAGO network of ground-based radars with GPM 37
4.3.1 Cross-comparison with GPM 37
4.3.2 Inter-comparison of ground radars 41

4.4 Results of the inter-comparison of the RELAMPAGO network of radars with GPM . . . 44
4.4.1 Cross-comparison of the ground-based radar with GPM . . . 44
4.4.2 Inter-comparison of the ground radars . . . 46
4.4.3 Bias consistency, analysis, and estimation . . . 48
4.5 Discussion . . . 53
4.6 Summary . . . 55

Chapter 5 Attenuation in melting ice, implications for C-band radars . . . 56
5.1 Introduction . . . 56
5.2 Methods . . . 59
5.2.1 Attenuation correction in the C-band . . . 60
5.2.2 Networked-based attenuation correction . . . 61
5.2.3 Doppler winds . . . 63
5.3 Data . . . 63
5.3.1 The RELAMPAGO C-band radars . . . 63
5.3.2 The December 14, 2018, study case . . . 66
5.4 Results . . . 69
5.4.1 Identifying Melting Ice . . . 69
5.4.2 Estimating the Attenuation in Melting Ice Regions . . . 73
5.4.3 Network-based Attenuation Correction Coefficients . . . 81
5.5 Discussion . . . 86
5.5.1 Identification of melting ice from simultaneous dual-radar and dual-polarimetric radar observations . . . 86
5.5.2 Conceptual model of melting ice from radar observations . . . 88
5.5.3 Estimating the attenuation of melting ice using a network-based approach 90
5.5.4 Polarimetric signatures of melting ice . . . 91
5.5.5 Variability of the melting ice attenuation correction coefficients . . . 92
5.5.6 Network-based attenuation coefficients in melting ice compared to previous studies . . . 94
5.5.7 Validation of the network-based attenuation coefficients using disdrometers . . . 96
5.6 Summary . . . 97

Chapter 6 Dual polarization spectral analysis in updraft environments . . . 100
6.1 Introduction . . . 100
6.2 Methods . . . 102
6.2.1 Estimation of the spectrum, FFT and autocorrelation . . . 102
6.2.2 Power spectrum (sZ) . . . 103
6.2.3 Differential spectrum (sZ_{dr}) . . . 103
6.2.4 Coherence spectrum ($s\rho_{hv}$) . . . 104
6.2.5 Autocorrelation method . . . 104
6.2.6 An alternative way to compute the spectrum, the direct Fourier method . 106
6.3 Data . . . 106
6.3.1 I&Q time series from the RELAMPAGO campaign . . . 107

6.3.2 Updraft and mix phase identification . . . 108
6.3.3 Advantage of RHI samples . . . 110
6.4 Results . . . 111
6.4.1 Power spectrum (sZ) estimation, insights from the autocorrelation and the Fourier transform . . . 111
6.4.2 Coherence spectrum, challenges and practical considerations . . . 117
6.4.3 Spectral average, practical considerations . . . 121
6.4.4 Spectral decomposition of melting ice in an updraft environment . . . 127
6.5 Discussion . . . 129
6.5.1 Lessons learned by computing the spectrum via the autocorrelation and the Fourier transform . . . 131
6.5.2 Microphysical analysis . . . 134
6.6 Summary . . . 135
6.6.1 Summary . . . 135
6.6.2 Future work . . . 136

Chapter 7 Insights from comparing multiple radar observations with convective-permitting high-resolution simulations . . . 138
7.1 Introduction . . . 138
7.2 Data and Methods . . . 139
7.2.1 Radar observations and retrieval . . . 139
7.2.2 Numerical Weather Simulations of the Dec. 13-14, 2018 case . . . 139
7.3 Results . . . 141
7.3.1 Radar observations of the Dec. 14, 2018 case . . . 141
7.3.2 WRF Simulations of the Dec. 14, 2018, case . . . 144
7.3.3 Comparison of model simulations and radar observations for the Dec. 14, 2018, case . . . 149
7.4 Summary . . . 151

Chapter 8 Dissertation Summary . . . 155
8.1 Summary . . . 155
8.2 Future work . . . 156

Bibliography . . . 157

LIST OF TABLES

3.1 Z_{dr} Bias via Z vs Z_{dr} dispersion 23
3.2 Z_{dr} Bias using vertical pointing scans 24

4.1 List of GPM DPR overpasses during RELAMPAGO with significant weather. The Radar column means the GRs that capture the overpass with a good alignment in time and space with GPM DPR. 34
4.2 Resolution of spaceborne and ground-based radar used in this study. 40
4.3 Summary of the cross-comparison with KuPR of the ground-based radars during RELAMPAGO. The time is for the overpass. The bias, correlation coefficient, and RMSE are computed as defined in the set of Eq. (4.6) where Rd_X is KuPR and Rd_Y is the GR. The Samples column refers to the number of points used in the comparison. 46
4.4 Summary of the inter-comparison between the ground-based radar on November 30th, 2018 case. The bias, correlation coefficient and, RMSE are computed as defined in the set of Eq. (4.6) where the order of radars is given by Rd_X vs. Rd_Y in the Radars column. The Samples column refers to the number of points used in the comparison. . 47
4.5 Residual bias (δB) for the faces of the graph in Fig. 4.11, and residual recalculated bias ($\delta\tilde{B}$) of the graph in Fig. 4.12. 50
4.6 From CHIVO to CSAPR, biases using different paths. Bias is computed as shown in Eq. (4.9) where Rd_X is CHIVO, Rd_Y is CSAPR. 52

5.1 Location of the RELAMPAGO C-band radars used in this study. The elevation is above mean sea level (MSL) 64
5.2 Melting ice attenuation correction coefficients where $\alpha = a_h/K_{dp}$, and $\beta = a_{hv}/K_{dp}$. a_h and a_{hv} are the horizontal and differential attenuation respectively 82

7.1 WRF configuration for the different simulations 140

LIST OF FIGURES

1.1 Radar Network in Colombia, credits A. Ladino 2
1.2 Radar Network in Argentina, credits SMN Argentina 3

3.1 CSU-CHIVO south of Cordoba Argentina 16
3.2 Map with location of radars. CSU logo means CHIVO, ARM is the location for CSAPR, RELAMPAGO means Obs. Center in Villa Carlos Paz and radar in Cordoba City is the RMA site Radar Meteorologico Argentino 17
3.3 CSAPR (big radome) at Yacanto site 18
3.4 Interference from sun can be use as a reference for pointing angle calibration 19
3.5 Radio Frequency Interference received from North and South West 20
3.6 Statistical analysis of the azimuth Correction 21
3.7 Histogram of Z_{dr} for a vertical pointing scan 22
3.8 Z vs Z_{dr} dispersion for a light rain case, Z_{dr} bias is 0.71 23
3.9 Echo top Statistic. Blue x is the average echo top and red star is the highest echo top observed during the day 24
3.10 Max. Reflectivity Statistic. Blue x is the average max. reflectivity and the red star is the highest reflectivity observed during the day 25

4.1 CSU-CHIVO deployed south of Cordoba City, Argentina, during RELAMPAGO. . . . 30
4.2 ARM mobile facility deployed during CACTI-RELAMPAGO. Sensors left to right: Sonic Detection and Ranging wind profiler (SODAR), C-band Scan Precipitation Radar 2 (CSAPR-2), X and Ka band Scan ARM Cloud Radars (XSACR and KaSACR), and Ka-band Zenith Radar (KAZR). 30
4.3 Map with the locations of the network of C-band radars during the RELAMPAGO campaign (CSU-CHIVO, CSAPR-2, and RMA-1). 31
4.4 KuPR reflectivity at 2 km altitude on (a) December 6th, 2018 at 05:22 UTC, (b) January 13th, 2019 at 4:01 UTC, and (c) January 31st, 2019 at 22:35 UTC. The solid line in (a), and (b) indicates CHIVO RHI along 315°, and 192° azimuth respectively. The dashed line in (a), (b), and (c) denotes KuPR angle bins 39, 13, and 37 respectively. The doted lines represent the edges of the KuPR swath. The rings in (a), and (b) are centered at CHIVO, whereas for (c) are centered at CSAPR. 35
4.5 December 6th, 2018 reflectivity from: (a) CHIVO RHI along 315° azimuth at 05:18 UTC, and (b) KuPR along angle bin 39 at 05:22 UTC. The CHIVO RHI and DPR angle bin are marked by the solid and the dashed line in Fig. 4.4a. 36
4.6 January 13th, 2019. (a): DPR along angle bin 13 at 4:01 UTC, Ku-band reflectivity (i), and Dual Frequency Ratio (DFR) (ii). (b): CHIVO RHI along 192° azimuth at 4:06 UTC, reflectivity (i), differential reflectivity (ii), specific differential phase (iii), and hydrometeor classification (iv). 38
4.7 KuPR reflectivity on January 31st, 2019 at 22:35 UTC, 3D depiction. 39
4.8 CHIVO reflectivity on November 30th, 2018. (a) PPI scan at 3:30 UTC, and (b) RHI scan at 3:37 UTC. 43

4.9 CSU-CHIVO and KuPR reflectivity comparison for January 13, 2019 case at 4:02 UTC. CHIVO reflectivity is corrected for attenuation using (a) global average coefficient, and (b) coefficient computed from the disdrometer in the field. The dots represent the mean and the bars depict one standard deviation. 45
4.10 CSAPR-2 and CSU-CHIVO reflectivity comparison for November 30th, 2018 case at 3:30 UTC. CSAPR and CHIVO reflectivities are corrected for attenuation using coefficient computed from the disdrometer in the field. 47
4.11 Bias (parenthesis, dB) and correlation coefficient (square brackets) from the cross and inter comparison. The arrows indicate the direction in which the bias is computed, being X the beginning and Y the end of the arrow. 49
4.12 Recalculated bias using the information from the other path as in Eq. (4.12), the arrows are defined as in Fig. 4.11. 53

5.1 Map with the location of the C-band radars used in this study. 64
5.2 Picture of the C-band radars used in this study deployed in Argentina. (a) is CSU-CHIVO radar deployed South Cordoba City, (b) is CSAPR-2 deployed near the Sierras de Cordoba. 65
5.3 Hailstone reported by the community on December 14, 2018, near Cordoba city [1]. . 66
5.4 Differential reflectivity from CSU-CHIVO (a) and CSAPR-2 (b). CSAPR's plot is centered at CHIVO coordinates. The black square shows the region with a spike in Z_{dr}. The dotted line in the CHIVO and CSAPR plots refers to the azimuth 242° and 26°, respectively. 67
5.5 Reflectivity, differential reflectivity, and copolar correction along azimuth 242° shown in Fig. 5.4 in dashed line. 68
5.6 Vertical reflectivity (a), differential reflectivity (b), specific differential phase (c), and copolar correction (d) form an RHI that intersects the melting ice region. 70
5.7 Hydrometeor classification inferred from the dual polarimetric measurement presented in Fig.5.6. 71
5.8 Dual Doppler analysis from CSU-CHIVO and CSAPR-2 at 2:00 UTC, December 14, 2018. (a) shows the maximum composite reflectivity over the column and updraft contours starting at 20 m/s. (b) shows a Constant Altitude PPI (CAPPI) over the region marked by a square in (a). The contours this time are updrafts starting at 10 m/s. (c) shows a vertical cross-section marked by the dashed line in (b). 72
5.9 CHIVO Network-based (Z_n), corrected (Z_c), and measured (Z_m) reflectivity along the 242° azimuth. 74
5.10 Difference in the reflectivities shown in Fig. 5.9. In blue, it is shown the difference between Z_n and Z_m. In red is shown the difference between Zn and Z_c, and in orange is shown the difference between Z_c and Z_m. 76
5.11 Differential reflectivity (black), copolar correlation (blue), and the difference between the network-based reflectivity and the corrected reflectivity from CHIVO radar (red). . 77
5.12 Network-based (Z_n), enhanced coefficients (Z_e), and corrected reflectivity (Z_c). 78
5.13 Reflectivity (blue) and differential reflectivity (black) from CSAPR radar. The CSAPR Z_{dr} is near 2 dB before entering the melting ice region. 79

5.14 CHIVO reflectivity (blue), differential reflectivity using enhanced coefficients (solid black), and the corrected differential reflectivity using nonenhanced attenuation correction coefficient (doted black). 80
5.15 CHIVO reflectivity along the 201°azimuth. In blue is shown the network-based reflectivity, in red the corrected reflectivity using a single radar, and in magenta the measured reflectivity. 83
5.16 Attenuation correction coefficient for rain in the C-band. (a) shows the horizontal attenuation correction coefficient where $\alpha = a_h/K_{dp}$, and a_h is the horizontal attenuation. (b) shows the differential attenuation correction coefficient where $\beta = a_{hv}/K_{dp}$, and a_{hv} is the differential attenuation. To the left of (a) and (b), it is shown a boxplot of the network-based attenuation coefficient under rain conditions. The bars in the middle of (a) and (b) show a 95% confidence interval for the mean of the network-based coefficients. The right bars in (a) and (b) show a 95% confidence interval of the coefficient retrieved from local disdrometer measurement 84
5.17 Conceptualization of melting ice based on radar observations. In (a) is shown the reflectivity in solid and contours of differential reflectivity starting at 4 dB. The arrows in (a) and (b) indicate the vertical motivation drawn subjectivity following the Doppler winds direction. The square in (b) marks the region where a mix of phases was inferred by hydrometeor classification. (b) shows the interactions of particles in the area marked by the square in (a) 88
5.18 Networked attenuation coefficients for melting ice compared with previous studies. (a) shows the horizontal attenuation correction coefficient where $\alpha = a_h/K_{dp}$, and a_h is the horizontal attenuation. (b) shows the differential attenuation correction coefficient where $\beta = a_{hv}/K_{dp}$, and a_{hv} is the differential attenuation. To the left of (a) and (b), it is shown a boxplot for the melting ice coefficients that were found using the network-based approach. The bars in the middle of (a) and (b) represent the variability obtained from the scattering simulation by [2]. The right square in (a) and (b) represents the coefficients found by [3] using direct comparison with S-band observations. 95

6.1 Reflectivity (a), differential reflectivity (b), specific differential phase (c), and copolar correlation (d) of the RHI in CSU-CHIVO radar where updraft was identified 108
6.2 Reflectivity (solid), differential reflectivity (contours), and Doppler winds for the RHI of CHIVO radar in Fig. 6.1 109
6.3 Hydrometeor classification inferred from the polarimetric measurements in Fig. 6.1 . . 109
6.4 Power spectrum estimates using the autocorrelation method. The autocorrelation is multiplied with a Blackman window 113
6.5 Power Spectrum estimate using the direct Fourier transform method and a rectangular window 114
6.6 Power Spectrum estimate using the direct Fourier transform method and a rectangular window 115
6.7 Power spectrum estimate using the autocorrelation method and multiplying the samples with a Blackman window 116
6.8 Coherence spectrum computed using a Blackman window to multiply the autocorrelation and the cross-correlation 117

6.9 Coherence spectrum computed using Blackman window to multiply the autocorrelation and the samples . . . 120
6.10 Power spectrum estimation after averaging spectrum over time using 64 samples . . . 122
6.11 Power spectrum with time average of 64 samples and filtered with a Gaussian window of length five along the velocity and the range axis . . . 123
6.12 Differential reflectivity spectrum, using the same method as Fig. 6.11sρ_{hv} . . . 124
6.13 Coherence spectrum, windowing the autocorrelation and the samples, and doing spectrum averaging over 64 samples. . . . 126
6.14 Coherence spectrum computed as Fig. 6.13, this time using a Blackman window for the coherence spectrum and a Hann window for the horizontal and the vertical spectra . 127
6.15 Coherence spectrum Filtered using a Gaussian filter. The coherence spectrum is computed as in Fig. 6.14 . . . 128
6.16 Spectral decomposition from CHIVO dual polarimetric measurements along the 2.5° elevation. Power spectrum (a), differential spectrum (b), and coherence spectrum (c). . 129
6.17 Spectral decomposition of the dual polarimetric measurements from CSU-CHIVO radar at 40.5 km in range, 2.5° in elevation, and azimuth 242°. Power spectrum (sZ) is shown in red; the differential spectrum (sZ_{dr}) is shown in black, and the coherence spectrum (ρ_{hv}) in dotted blue. . . . 130

7.1 Domain of the WRF simulations . . . 140
7.2 Max. reflectivity from CSU-CHIVO radar from 1:00 UTC to 1:30 UTC before the convection initiation (CI) starts in the East slope of the SdC. . . . 141
7.3 Max. reflectivity from CHIVO radar from 1:40 to 2:30 UTC after the boundary pass and the convective initiation starts in the terrain. . . . 142
7.4 Max. reflectivity from CHIVO radar from 2:50 to 6:00 UTC. These different times illustrate how the back-building pattern occurs during this case. . . . 143
7.5 Max. reflectivity from WRF simulations from 23:00 UTC to 01:00 UTC. . . . 145
7.6 Max. reflectivity from WRF simulations from 01:30 UTC to 03:00 UTC . . . 146
7.7 Max. reflectivity from WRF simulations from 03:10 UTC to 03:40 UTC . . . 147
7.8 Max. reflectivity from WRF simulations from 04:00 UTC to 05:30 UTC . . . 148
7.9 Total rain accumulation for the Dec. 14, 2018 case. The four panels to the left are rain accumulation from models, and the panel to the right corresponds to the radar's estimates. . . . 150
7.10 Rain rate evolution from Simulations and radar estimation. The vertical intense rain rate shown in the bottom-left panel suggests the initiation of new cells on the eastern slope of the SdC. . . . 151
7.11 Rain accumulation from models (a), (b), and (c). And accumulation from radar rain estimate (d) . . . 152
7.12 Hovmoller diagram showing the rain rate evolution from Simulations and radar estimation. . . . 152

Chapter 1

Introduction

1.1 Motivation

Dual-pol radar has become a useful tool for weather agencies along with the world. In the US, for example, the Next-Generation Radar (NEXRAD) is a network of S-band weather radar operated by the National Weather Service. NEXRAD is one of the most important information resources for many decisions and nowcasting [4]. In general, weather radar has helped to predict hazard weather, save properties, and live not only in the US but in many other countries.

The S-band frequency has an important advantage in terms of the attenuation and the electromagnetic regime. The signal in S-band radar is not significantly attenuated by heavy rain as other bands such as C-band or X-band. Besides, the range of particle sizes that are not affected by resonance effects, also known as Mie Scattering, is wider. It means S-band radars can measure bigger particles properly in the Raleigh regime [5].

C-band radars have an enormous potential to improve forecasting skill in countries of emerging economy (CEE) located in tropical environments. Most of these countries do not have enough observational infrastructure, technology, and skill to predict severe weather as demanded in the new global warming scenario. There has been a proliferation of C-band radar in CEE [6], allowing precipitation observations to be obtained for the first time in these countries. However, convective precipitation, which is more prevalent in CEE in tropical/subtropical regions, makes the attenuation correction for C-band radars more challenging.

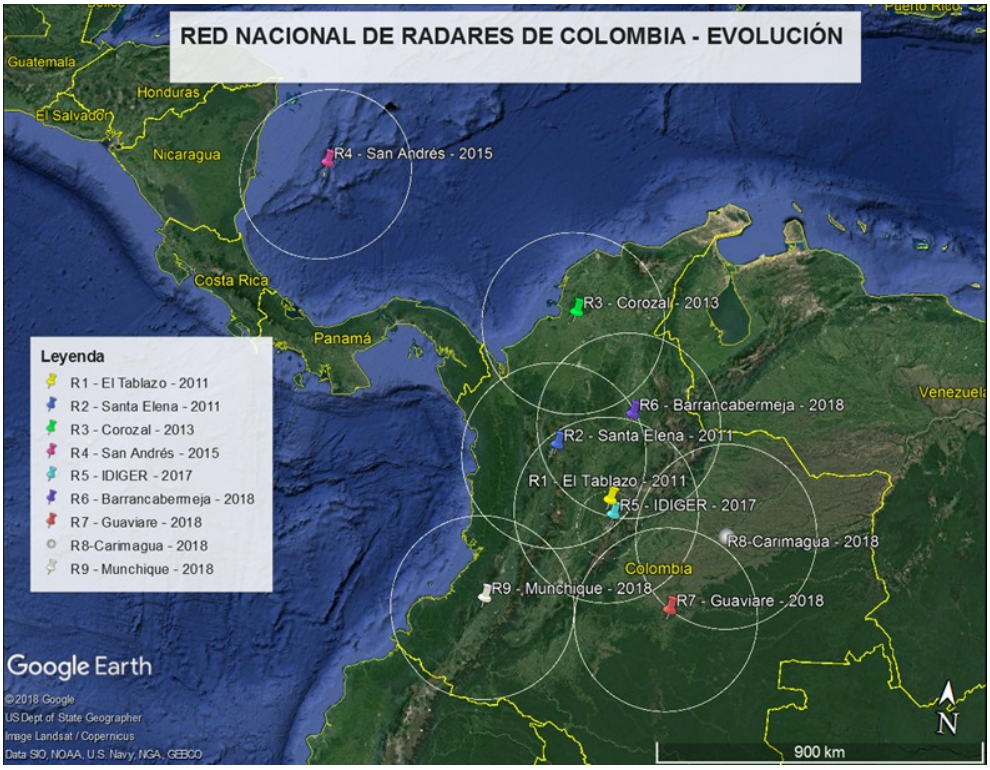

Figure 1.1: Radar Network in Colombia, credits A. Ladino

Most of the radars that have been installed recently in South America are C-band radar [7]. The reasons are that they are smaller than S-band and less costly. One of the important considerations of C-band with respect to S-band radar is the attenuation of the signal by heavy rain. However, attenuation correction algorithms have shown good performance in regions like Europe and the US. Fig. 1.1 shows the dual-polarized radars that have been installed in Colombia, while Fig. 1.2 shows the distribution of radar in Argentina, Paraguay, and South Brazil.

The C-band is the most prevalent frequency for radars in South America; however, the C-band poses additional challenges for attenuation correction in tropical/subtropical climatologies due to frequently occurring convective storms. The C-band provides advantages in terms of cost, power consumption, and sensitivity compared to the S-band [8]. In South America, Argentina alone has 11 C-band radars and plans to install 10 more. Similarly, Colombia has 10 C-band radars and plans to install 3 more. However, C-band radars need attenuation correction because a significant part

of the signal gets absorbed by the rain and melting ice particles, especially in areas with heavy precipitation [9].

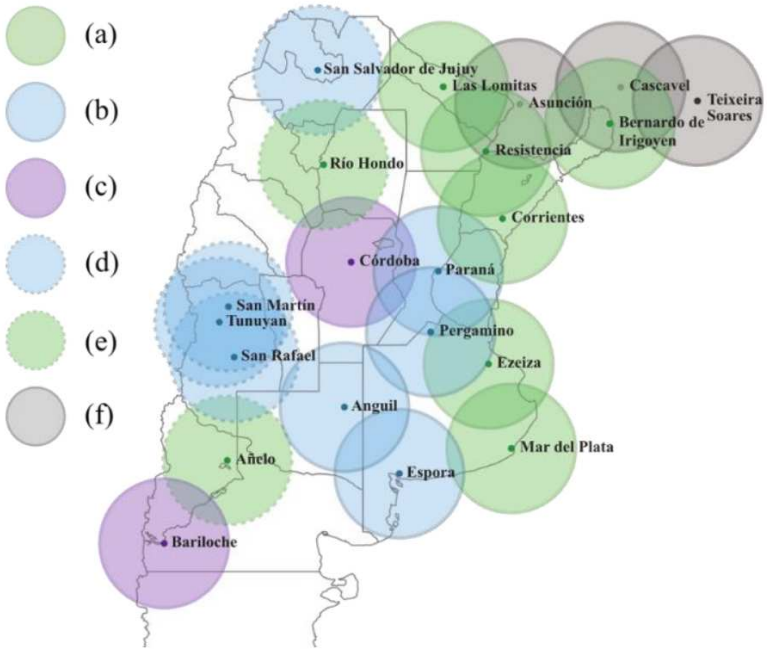

Figure 1.2: Radar Network in Argentina, credits SMN Argentina

1.2 Statement of the Problem

Weather radars have an enormous potential to improve our understanding of severe weather in tropical and subtropical climatologies. In recent years, there has been a proliferation of C-band radars in countries located in tropical and subtropical regions in the Southern hemisphere, allowing weather radar observations to be obtained for the first time in these countries. However, convective precipitation, which is more prevalent in tropical/subtropical regions, makes C-band radar observations and rainfall retrievals more challenging in these regions.

In tropical and subtropical regions, with an increase in mixed-phase and large drops due to more convection, radar correction algorithms become more important to accurately represent these storms, especially in C-band radars [10]. Radar attenuation correction algorithms work under the

assumption of pure rain and Rayleigh regime scattering [11, 12]. However, large drops and mixed-phase precipitation cause resonance and anomalous scattering that significantly affect shorter wavelength measurements, such as the C-band radar measurements [9, 13]. In addition, C-band radars are the most common radars in tropical and subtropical countries [6].

Evaluation of C-band correction algorithms has shown a good performance in regions like Europe and Australia [9, 14]. Nevertheless, studies have shown that big drops, more common in tropical regions, can cause a significant bias in dual-pol measurement in the 5cm wavelength [10, 13]. With the constant growth of C-band radar in South America, the question that arises is how C-band performs in a region that has mostly a tropical and sub-tropical climatology.

[15] presents the Americas lightning map using the GML sensor onboard GOES R. This study shows that South America has a significant number of hot-spots of lightning. Using lightning as a proxy of severe weather and thunderstorm, it is possible to say that convective storms are significantly frequent in South America climatology. From TRMM perspective, [16] shows from a 3-year climatology that convection is more prevalent than stratiform precipitation in South America.

In 2018, CSU sent CHIVO to Argentina, a C-band radar with dual polarimetric capability. The radar was sent for the RELAMPAGO field campaign. At the same time and close by, DOE deployed CSAPR, another C-band radar with similar characteristics as CHIVO. Both radars were collecting simultaneous observations for more than three months. This unique set-up of radars during RELAMPAGO is a big opportunity to evaluate the performance of C-band under different precipitation regimes, especially over intense storms.

1.3 Research Question

How to employ multiple radar observations in a network to understand microphysical processes in deep convection. To answer that question, data collected during the RELAMPAGO campaign in Argentina is used to take advantage of simultaneous observation of the C-band network deployed during the campaign.

1.3.1 Main objective

To retrieve microphysical variables to study convective processes occurring in severe weather and to investigate practical considerations unveiled by simultaneous radar observations in a network.

1.3.2 Secondary Objective

Some of the key questions that will be addressed in this dissertation are:

1. How to use simultaneous radar measurements to self-calibrate the instruments in a network.
2. How to quantify and parameterize the attenuation of melting ice using a network-based approach.
3. How to compute dual-polarization spectra to study particle compositions in updraft and mix-phase environments.
4. How numerical prediction models (NWP) resolve microphysical processes observed by radar in La Plata Basin.

1.4 Overview

This document is organized as follows: Chapter 2 shows the theoretical framework. Chapter 3 shows the data used for this study and the evaluation and calibration of the data set. Chapter 4 presents a cross-validation of the network of the C-band used in this study with GPM. Chapter 5 presents a study of radar signal attenuation in melting ice. Chapter 6 shows a guide on how to compute the dual-polarization spectral decomposition in updraft and hail environments. Chapter 7 compares radar observations with high-resolution numerical models for a representative case. Finally, the conclusion is presented in Chapter 8.

Chapter 2

Background

Radar systems started as military application but with the advanced of the technology they became in a useful tool for atmospheric sciences. Most of their advantage come from their active capability, i.e. the capacity to emit their own signal. This technology has achieved a good level of development for ground base observation. For example, dual polarization radars have been extensively used to acquire information about precipitations and clouds worldwide. Nowadays, this technology has been extended not only for ground but also for space observation that permits to take information in a global scale.

2.1 Fundamentals of Radars

Radar systems started as military application but with the advanced of the technology they became in a useful tool for atmospheric sciences. Most of their advantage come from their active capability, i.e. the capacity to emit their own signal. This technology has achieved a good level of development for ground base observation. For example, dual polarization radars have been extensively used to acquire information about precipitations and clouds worldwide. Nowadays, this technology has been extended not only for ground but also for space observation that permits to take information in a global scale. $Radar$ stands for radio detection and ranging. The following equation shows how the range is calculated from the radar signal:

$$R = \frac{cT_R}{2} \tag{2.1}$$

And the following is an expression of the radar equation [17]:

$$P_r = \frac{P_t G}{4\pi R^2} . \frac{\sigma}{4\pi R^2} A_e \tag{2.2}$$

where P_r is the received power and P_t is the transmitted power, G is the gain of the antenna and A_e is the effective area of the antenna.

The max. range (R_{max}) is the distance after a target cannot be detected. The max. range is given as follows:

$$R_{max} = \left[\frac{P_t G A_e \sigma}{(4\pi)^2 S_{min}} \right] \tag{2.3}$$

2.2 Precipitation Measurement

Radar is an active instrument that emits its source of radiation and measures the backscatter from targets. It gives the advantage to choose Radio Frequency (RF) parameters such as the wavelength, power, or polarization to sense a specific kind of particles properly. For example, if the target of interest is precipitation, then one can choose a frequency that allows working the radar in the Rayleigh regime, where the backscatter is proportional to the size of the particles. However, if one needs more portability, one can choose a radar with a shorter wavelength.

A radar transmits an energy pulse of a short duration and then measures the backscatter power from particles along the trajectory of the beam. Indeed, a radar measures the backscatter radiant flux. For a volume target such as clouds, the backscatter power P_r that the radar received is given by the following relation [18]:

$$P_r \propto \frac{\eta}{r^2} \tag{2.4}$$

Where r, the range, is the distance between the antenna and the target, and η is the backscatter cross section per unit of volume or, in other words, the sum of the backscatter cross section (σ_b) of all the particles in the sampled volume:

$$\eta = \frac{1}{V} \sum_i \sigma_b(i) \tag{2.5}$$

note that the backscatter is the portion of energy that scatters exactly backward toward the radar antenna. In mathematical from, it means:

$$\sigma_b = \sigma_s.p(\pi) \tag{2.6}$$

where σ_s is the volume scattering coefficient or also known as scattering cross section. For Rayleigh regime, scattering cross section is given by:

$$\sigma_s = \frac{2\pi^5}{3}\frac{|K|^2 D^6}{\lambda^4} \tag{2.7}$$

$$p(\Psi_s) = \frac{3}{4}(1 + cos^2\Psi_s) \tag{2.8}$$

where $K = (m^2 - 1)/(m^2 + 2)$, m is the complex index of refraction and absorption and D is the diameter of the particles. Replacing Eq: (2.7) and Eq: (2.8) in Eq: (2.6) and taking $\Psi_s = \pi$ in Eq: (2.8), it yields:

$$\sigma_b = \frac{\pi^5}{\lambda^4}|K|^2 D^6 \tag{2.9}$$

now, assuming particles are spread according to a drop size distribution $N(D)$, then it is possible to express η in the following integral form:

$$\eta = \int_0^\infty \sigma_b(D).N(D)\, dD = \frac{\pi^5}{\lambda^4}|K|^2 \int_0^\infty D^6.N(D)\, dD \tag{2.10}$$

the last integral on the left of Eq: (2.10) is the radar reflectivity Z, defined as:

$$Z := \int_0^\infty D^6.N(D)\, dD \tag{2.11}$$

note that the reflectivity is the sixth moment of the DSP. That's why Z is sensitive to small changes is D, because D is elevated to the sixth in the integral.

Z is considered the primary radar measurement, and it is used in many applications such as rain rate estimation, liquid water content calculation, hydrometeor classification, etc. The units of Z are

in $[mm^6/m^3]$, and it is normally expressed in logarithmic scale (dBZ), i.e. $Z[dBZ] = 10.log(Z)$ because of the wide range of values it can take. Given the last derivation, then the received power is proportional to:

$$P_r \propto \frac{|K|^2 Z}{r^2} \tag{2.12}$$

in fact, when one considers the radar equation, Eq: (2.12) becomes

$$P_r(r) = \frac{c\tau}{2} \frac{P_t G_0^2}{(4\pi)^3} \frac{\pi\theta_1\phi_1}{8ln2} \frac{\pi|K|^2}{\lambda^2} \frac{Z(r)}{r^2} \tag{2.13}$$

the first part on the left of Eq: (2.13) before the reflectivity Z is also known as the radar constant as is an important parameter for radar calibration [19].

2.3 Attenuation Correction

The measured reflectivity Z_m differs from the intrinsic reflectivity Z due to the attenuation along the path. The attenuation is basically the fraction of the energy that is lost through the medium, very similar to the optical depth from radiation theory. In previous section, it was proved that $Z \propto P_r$. Using Beer's law, the following expression is obtained Z_m and Z:

$$Z_m(r) = Z(r) \left[exp\left(- \int_0^r \sigma_e \, dS \right) \right]^2 \tag{2.14}$$

where σ_e is the volume extinction coefficient, which is the volume absorption plus the volume scattering coefficient. The square power in the expression represents the attenuation in both trajectories, from the radar to the cloud and backward. The exponential function in the brackets is the transmittance along the path, which is the ratio of transmitted radiant power to incident radiant power [18]. Eq: (2.14) shows the relation between Z_m and Z in terms of the optical properties and energy transfer of the medium.

Define the attenuation as the slant of the transmittance along one portion of the path. In other words, let's call attenuation the cumulative extinction from range r_{i-1} to r_i:

$$A(r_i) := 2. \int_{r_{i-1}}^{r_i} \sigma_e \, dS \tag{2.15}$$

not that the attenuation is very similar to the definition of optical depth from radiation theory. Now, when one replaces Eq: (2.15) in Eq: (2.14), and doing some transformation explained in [11]:

$$Z_m(r) = Z(r).exp\left(-0.46 \int_0^r A(S) \, dS\right) \tag{2.16}$$

normally, reflectivity and attenuation are expressed in logarithmic scale, as the following form [11]:

$$Z_m[dB] = Z[dB] - 2A.r \tag{2.17}$$

for an inhomogeneous path (i.e A_h varies along the path) Eq: (2.17) may be modified as,

$$Z_m[dB] = Z[dB] - 2 \int_0^r A(S) dS \tag{2.18}$$

$$Z_m[dB] = Z[dB] - 2\alpha \int_0^r K_{dp}(S) dS \tag{2.19}$$

$$Z_m[dB] = Z[dB] - 2\alpha[\Phi_{dp}(r) - \Phi_{dp}(0)] \tag{2.20}$$

where the liear relation $A = \alpha K_{dp}$ has been used along the propagation path. Thus, the corrected Z at a range r is obtained as,

$$Z[dB] = Z_m[dB] + \alpha[\Phi_{dp}(r) - \Phi_{dp}(0)] \tag{2.21}$$

and the procedure is not dependent on the functional form of $K_dp(r)$ at each point along the path. A range of α-values have been reported in the literature especially at C-band [10]. The cumulative

effect of differential attenuation A_{dp} on Z_{dr} is specially evident at C-band. The correction for Z_{dr} for a homogeneous propagation path is given by:

$$Z'_{dr}(r)[dB] = Z_{dr}(r)[dB] - 2A_{dp}r \tag{2.22}$$

which can be generalized for an inhomogeneous path as,

$$Z'_{dr}(r)[dB] = Z_{dr}(r)[dB] - 2\int_0^0 A_{dp}(S)dS \tag{2.23}$$

and assuming the relationship of $A_{dp} = \beta K_{dp}^b$, the corrected $Z_d r$ at range r is obtained as,

$$Z_{dr}(r)[dB] = Z'_{dr}(r)[dB] + \beta[\Phi_{dp}(r) - \Phi_{dp}(0)] \tag{2.24}$$

2.4 Dual Doppler Analysis

Weather radar can measure radial velocity using the Doppler effect. When particles are moving around the radar domain, they generates a shift in the received signal. That shift ω_d modulates the base-band signal. This is the physical reason why radar are able to remotely measure the radial velocity.

Mathematically, the radial Doppler velocity can be expressed as [20]:

$$\phi = 2\pi \times \frac{2R}{\lambda} = 4\pi R/\lambda \tag{2.25}$$

Differentiating Eq. (2.25) with respect to time gives the rate of change of phase:

$$\omega_d = \frac{d\phi}{dt} = \frac{4\pi}{\lambda}\frac{dR}{dt} = \frac{4\pi v_r}{\lambda} = 2\pi f_d \tag{2.26}$$

where $v_r = dR/dt$ is the radial velocity (m/s). This equation can be also expressed as:

$$f_d = \frac{2v_r}{\lambda} = \frac{2f_c v_r}{c} \tag{2.27}$$

where f_c is the carry frequency of the radar.

The radial velocity observed by the radar is not the the velocity of the storms. Instead, radial velocity is the projection of the wind field over the radar pointing vector.

The wind vector has three components that are traditionally referred as u, v and w components (eastward,northward, and vertical, respectively). As described by [21], Doppler velocity v_r in the radar coordinate system is the projection of (u, v, w) onto the line of sight, i.e.,

$$v_r = usin\phi cos\theta + vcos\phi cos\theta + (w + w_t)sin\theta \tag{2.28}$$

where ϕ and θ are the azimuth and elevation angles of the radar beam, and w_t is the precipitation final velocity. In case of overlapped coverage by multiple radars, the projections at different beam angle for the same target form a system of independent linear equations, in a matrix form as:

$$V_r = H[u, v, w + w_t]^T \tag{2.29}$$

where, assuming n radars

$$V_r = [v_r^1 ... v_r^n]^T \tag{2.30}$$

$$H = \begin{pmatrix} sin\phi_1 cos\theta_1 & cos\phi_1 cos\theta_1 & sin\theta_1 \\ \vdots & \vdots & \vdots \\ sin\phi_n cos\theta_n & cos\phi_n cos\theta_n & sin\theta_n \end{pmatrix} \tag{2.31}$$

Then the 3-D wind field can be solved from the linear system. Using generalized least square technique, wind velocity can be solved as,

$$[u, v, w + w_t]^T = (H^T H)^{-1} H^T V_r \tag{2.32}$$

The horizontal wind components u and v can be retrieved if more two radars are available. The angle between the two radar needs to be big enough to provide sufficient independence for both radar velocity. Otherwise, each would be a linear combination of one another.

The vertical component can be resolved using mass conservation principle and variational analysis described by [22]. The following equations modeled mass conservation and the horizontal motion, which mainly governed compressible atmosphere under an anelastic approximation.

$$\frac{\partial(\rho_s u)}{\partial x} + \frac{\partial(\rho_s v)}{\partial y} + \frac{\partial(\rho_s w)}{\partial z} = 0 \tag{2.33}$$

$$\frac{\partial u}{\partial t} + u\frac{\partial u}{\partial x} + v\frac{\partial u}{\partial y} + w\frac{\partial u}{\partial z} = -\frac{\partial \pi}{\partial x} \tag{2.34}$$

$$\frac{\partial v}{\partial t} + u\frac{\partial v}{\partial x} + v\frac{\partial v}{\partial y} + w\frac{\partial v}{\partial z} = -\frac{\partial \pi}{\partial y} \tag{2.35}$$

where ρ_s is a height-dependent base-state density, and π is the perturbation pressure divided by ρ_s.

Subtracting the y derivative of Eq. (2.34) from the x derivative of Eq. (2.35) yields the vorticity equation:

$$\frac{\partial \zeta}{\partial t} + u\frac{\partial \zeta}{\partial x} + v\frac{\partial \zeta}{\partial y} + w\frac{\partial \zeta}{\partial z} + \left(\frac{\partial v}{\partial z}\frac{\partial w}{\partial x} - \frac{\partial u}{\partial z}\frac{\partial w}{\partial y}\right) + \zeta\left(\frac{\partial u}{\partial x} + \frac{\partial v}{\partial y}\right) = 0 \tag{2.36}$$

where $\zeta := \left(\frac{\partial u}{\partial x} - \frac{\partial v}{\partial y}\right)$ is the vertical vorticity. Eq. (2.36). A boundary condition to solve last equation is given by the constraints of no downward flow in the ground level and also a zero updraft in the upper layer.

2.5 Spectral decomposition

Spectral decomposition is call to the representation of dual-pol measurement in the Fourier domain. [23] shows how spectral from time series can be extended to differential reflectivity and co-polar correlation.

The co-polar coherency spectrum is defined as:

$$\rho_{hv} = \frac{C_{hv}(v)}{\sqrt{P_{hh}(v)P_{vv}(v)}} \tag{2.37}$$

where $C_{hv}(v)$ is the co-polar cross spectrum and $P_{hv}(v)$, $P_v v(v)$ are hh and vv power spectra respectively. The co-polar coherency physical meaning is similar to the co-polar correlation coefficient and can be defined as a spectral decomposition of the co-polar correlation coefficient.

The spectral decomposition of differential reflectivity is defined as the ratio of hh and vv power spectra, $P_{hh}(v)/P_{vv}(v)$. Similar to the differential phase, the precipitation signal is characterized by the constant spectral differential reflectivity over all Doppler frequencies. The clutter spectral differential reflectivity, however, varies with Doppler frequency and range.

The slope of the spectral differential reflectivity exhibits interesting variations across the hail core, which suggests the presence of size sorting of hydrometeors caused by vertical shear in a turbulent environment [24].

During RELAMPAGO, CHIVO collected time series with severe weather going on. The spectral decomposition is used to understand better the microphysical process involved.

2.6 Large drops and C-band

Large drops can affect significantly polarimetric C-band measurement due to propagation effects. In [13], it is shown the sensitivity of C-band radars to large drops, particularly in the attenuation correction algorithms. In that study it is mentioned that attenuation for horizontal polarization and differential attenuation is significantly affected by the occurrence of large raindrops of sufficient concentration and the assumed raindrop axial ratio. The relations between A_H or A_{HV} and K_{DP} are not biased significantly by occurrence of large drops because of their low concentration within typical raindrop size spectra. However, the presence of large drops can cause, through resonant scattering effects, considerable enhancement of the maximum possible attenuation and lead to significant local increases of attenuation over very short paths. Examination of the attenuation as a function of the median volume diameter shows this clearly. Unlike the increase in variability associated with large raindrop occurrence, variations in the raindrop axial ratio can bias $A_H(K_{DP})$ and $A_{HV}(K_{DP})$.

In [10], the authors show how large drops bias the mean coefficients upward and increase the standard error associated with the mean empirical coefficients down range of convective cores that contain large drops. To reduce this error, the authors implemented a large drop correction that utilizes enhanced attenuation correction coefficient in large drop cores.

[10] proposed a method to identify areas with big drops. On those areas, the authors use enhanced attenuation correction coefficients. To validate their results, cumulative rain gauge amounts were compared with cumulative radar rainfall estimates using $R(Z_h)$ and $R(K_{dp}, Z_{dr})$ before and after correction.The correction procedure significantly reduced both the bias and standard error of both cumulative radar rainfall estimates to within expected ranges given typical measurement errors other than propagation.

As a conclusion, C-band is sensitive to large drops ($D_0 > 2.5mm$). Those type of drops size are common in tropical regions. As a result, they can affect significantly the performance of C-band products on those regions. Some studies have proposed procedures to correct the effect of large drops in dual-pol measurement; however, the validation of those studies have been done through simulation and point-wise insitu sensor. There is not still a final conclusion to correct those effects.

Given the RELAMPAGO data with significant severe weather, including large drops, and a network of C-band radar, this is a big opportunity to evaluate the performance of large drops correction in C-band radars.

Chapter 3

The RELAMPAGO experiment radar dataset

3.1 RELAMPAGO Overview

CHIVO (C-band Hydrometeorological Instrument for Volumetric Observation) is CSU C-band weather radar which has dual polarization capability that produces products such as reflectivity (Z), differential reflectivity (Z_{dr}), differential phase (ϕ_{dp}), and specific differential phase (K_{dp}). During the RELAMPAGO field campaign, CHIVO was deployed for about 3 months of continuous operation with good performance. CHIVO started operation in Argentina on November 10 and was continuously working until December 22. As per the agreement between the PIs, CHIVO was off during Christmas break (Dec22-Dec 26) and restarted operations on December 27 until January 31. Fig. 4.1 shows a picture of CHIVO in Lozada site.

Figure 3.1: CSU-CHIVO south of Cordoba Argentina

CHIVO site was located south of Cordoba city and it was about 30 minutes driving from Alta Gracia and 45 minutes drive from Villa Carlos Paz where the Observation Center was located. Fig. 4.3 shows the location of the radars deployed in RELAMPAGO.

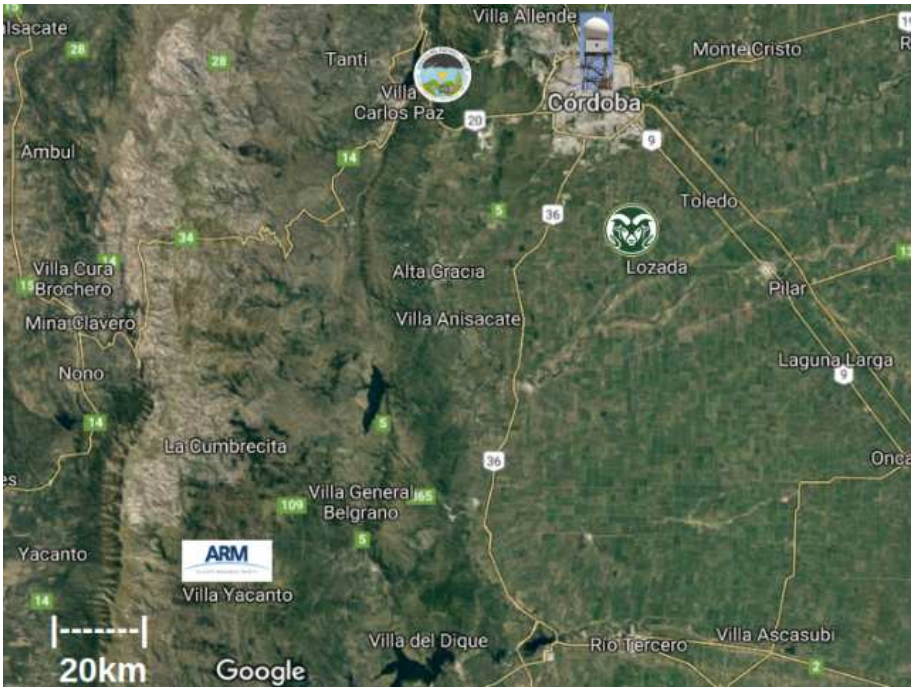

Figure 3.2: Map with location of radars. CSU logo means CHIVO, ARM is the location for CSAPR, RELAMPAGO means Obs. Center in Villa Carlos Paz and radar in Cordoba City is the RMA site Radar Meteorologico Argentino

During the campaign, the built in functions for attenuation correction and ground filters were disabled in the data and signal processor of CHIVO in order to archive the most unprocessed data as possible. This is important because we want to be able to capture signals that might be filtered out by this functionality in the Sigmet processor.

On the other hand, the C-Band Scanning ARM Precipitation Radar (CSAPR) is a dual-polarization Doppler weather radar that operates in a simultaneous transmit and receive (STAR) mode, splitting the transmit signal so that power is transmitted on both horizontal and vertical polarizations at the same time. The C-SAPR can also transmit on a single polarization (horizontal or vertical) and measure linear depolarization ratio (LDR).

In addition to the first three Doppler moments (reflectivity, radial velocity, and spectra width), the C-SAPR also provides differential reflectivity, correlation coefficient, and specific differential phase. The dual-polarization variables enable the provision of rainfall rate estimates and identification of precipitation types [25].

Figure 3.3: CSAPR (big radome) at Yacanto site

Fig. 4.2 shows CSAPR radar, big radome over the container, at Yacanto site. ARM site also contains other atmospheric sensor as can been seen in the figure. The site was closer to the foothill than CHIVO site. CSAPR was scanning in a 30min based strategy. It collected horizontal RHI, volume PPI and vertical pointing scans.

3.2 Radar calibration

3.2.1 Pointing angle calibration

During preliminary analysis it was found that the azimuth reference was shifting due to some loose positioning devices. This was further confirmed by several simple tests such as monitoring the Sun. Therefore it was decided to check and calibrate the azimuth for each experimental day. Subsequently three independent procedures were developed to perform pointing angle calibration, namely a) the Sun, b) position of persistent radio interference targets and c) position of ground targets.

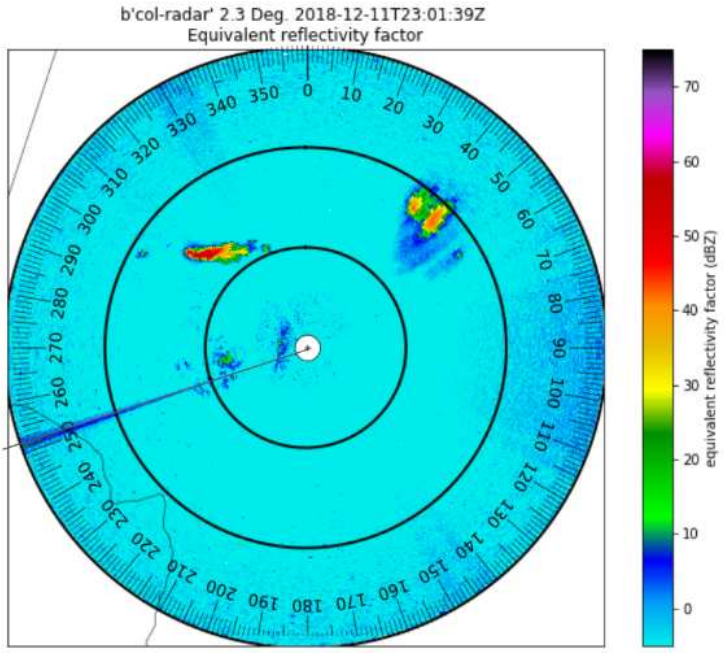

Figure 3.4: Interference from sun can be use as a reference for pointing angle calibration

Sometimes, the sun is captured by the radar when the elevation and azimuth coincide with the position of the sun while the radar is scanning as it is possible to see in fig. 3.4. For those cases, the observed position of the sun was then compared with the expected solar position using the solar position computations. While the azimuth was corrected the elevation was found to match the solar position and did not need any correction.

Radio Frequency Interference is not always bad. For this study, we use it to keep track of the true azimuth taking into account that interference sources don't change the location. Fig. 3.5 shows the RFIs used for this purpose, one in the north and the other in the southwest. These RFIs were selected among the other observed interference because they are isolated and they showed up in almost every low elevation sweep.

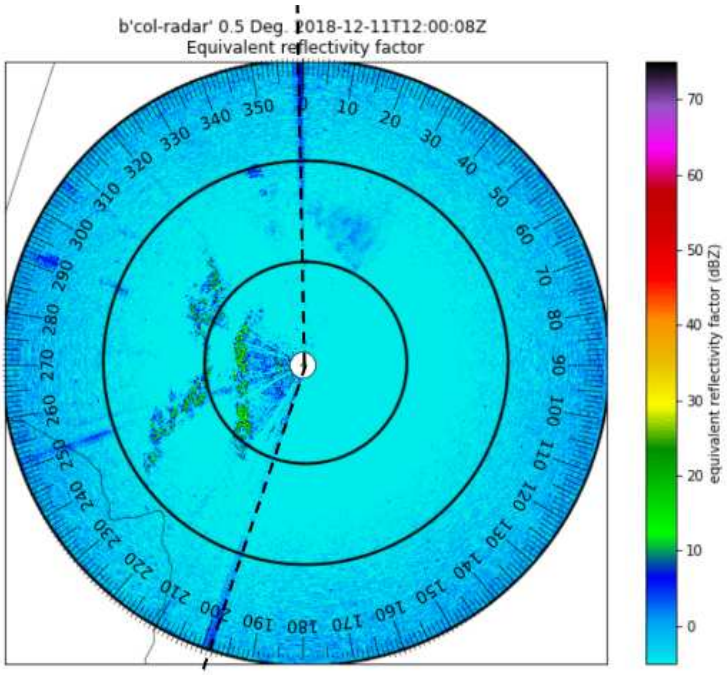

Figure 3.5: Radio Frequency Interference received from North and South West

The true location of the RFIs was determined using data on Nov 13, 2018, on which sun calibration was performed on CHIVO. The azimuth difference was obtained subtracting the true location of the azimuth to the angle where they show up in low elevation scans.

Additionally of radio frequency references, fixed targets were used to add more information and reduce the uncertainty of the azimuth evolution. To select good targets, fixed targets that meet the following condition for each low elevation sweep were chosen:

- Reflectivity over 45 dBZ
- ρ_{hv} below 0.85

- No other fixed target in a neighborhood around, i.e. isolated targets

The azimuth locations of the targets were monitored and tracked. Previous azimuth information from the sun and RFIs is used to start looking for the fixed targets in a neighborhood around their location plus the expected rotation. The difference in azimuth of each individual target is averaged and then a final difference is computed per each low elevation sweep. Since we are averaging many fixed targets, this leads to a more smooth retrieval.

Since there are three methods to evaluate azimuth calibration, each day all the methods were used and a mean curve was produced with a resolution of 6 hours. In addition a standard deviation in the mean bar was also calculated and plotted on the top of the mean. Based on the standard deviation of the mean, the accuracy of the azimuth calibration estimates are about 0.1 degree.

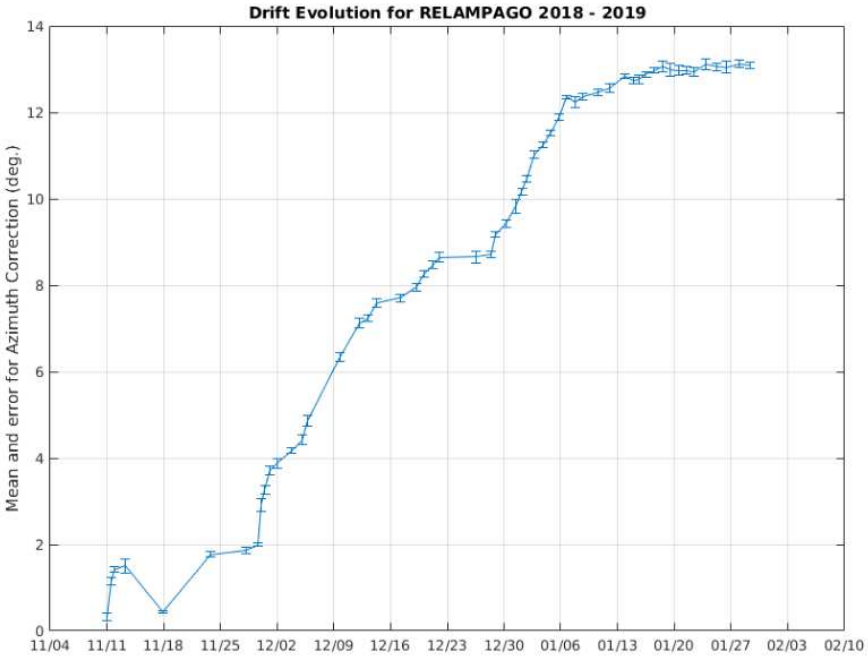

Figure 3.6: Statistical analysis of the azimuth Correction

Fig. 3.6 shows the mean and the standard deviation of the mean for the azimuth correction. Note that the error is a fraction of a degree and stays stable during the campaign. Azimuth cor-

rection was done using three independent methods for consistency of the retrieval and to reduce uncertainties. The correction uncertainty is of the order of tenths of a deg.

3.2.2 Z_{dr} Bias correction

Z_{dr} bias was computed using two independent methods: a) vertical pointing analysis and b) reflectivity versus differential reflectivity dispersion [19]. Birdbath scans were used for vertical pointing analysis while low elevation sweeps were used for differential reflectivity dispersion. To perform a birdbath scan, the radar is positioned at approximately 90 deg elevation and rotated to perform a 360 deg azimuth sweep. The melting layer, also known as the 0 deg level, is found using radiosonde information. The data collected below the melting layer is used to find the bias from vertical pointing analysis. Ideally, when a water drop is seen vertically, the Z_{dr} is expected to be zero. Thus, a finite deviation in the value of Z_{dr} in these cases is considered biased in Z_{dr}. Any azimuth variation due to external factors are averaged out using a full 360 degree scan. The following pictures shows an example for both methods respectively.

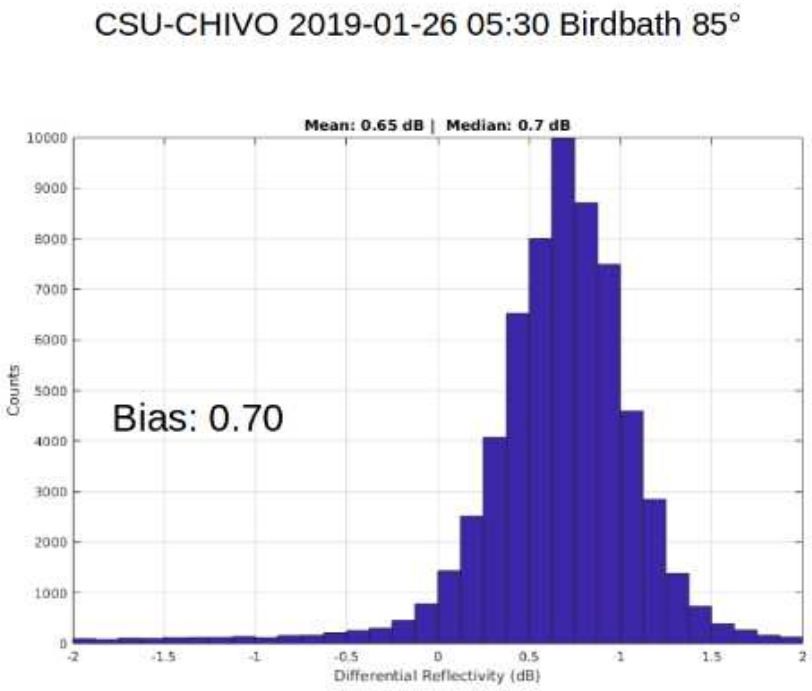

Figure 3.7: Histogram of Z_{dr} for a vertical pointing scan

Table 3.1: Z_{dr} Bias via Z vs Z_{dr} dispersion

Case	Z vs $Z_{dr} Bias(dB)$
2018/11/22 15-18 UTC	0.89
2018/11/26 09-12 UTC	0.71
2018/11/26 21-24 UTC	0.80
2018/12/01 09-12 UTC	0.87
Average	0.81

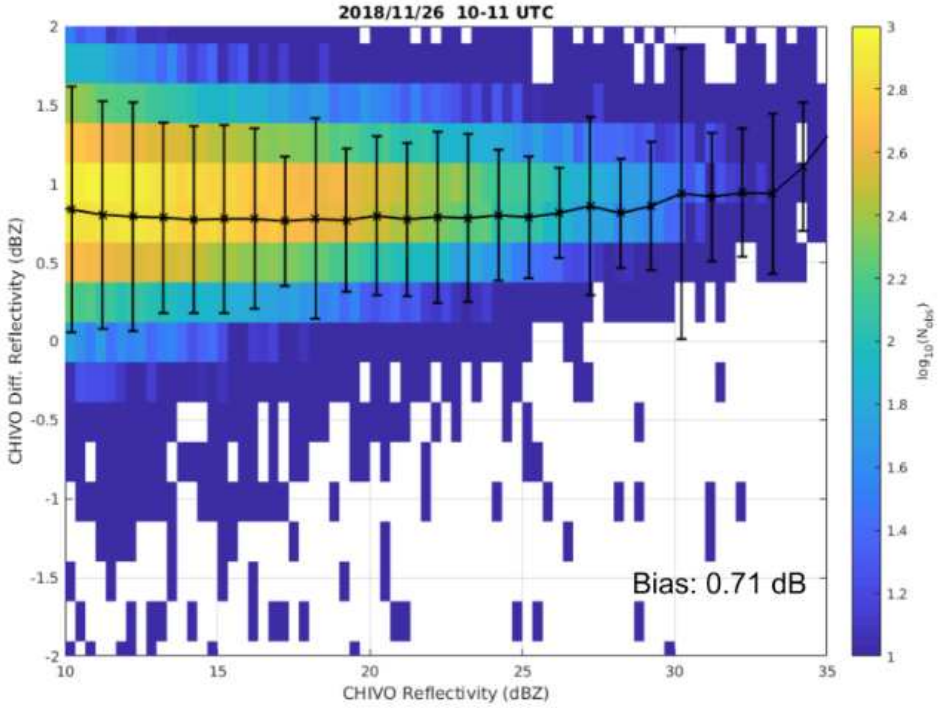

Figure 3.8: Z vs Z_{dr} dispersion for a light rain case, Z_{dr} bias is 0.71

Tables in Fig. 3.2 shows a summary of the Z_{dr} bias during the campaign for CHIVO. Note that the Z_{dr} bias remains stable during the field campaign and also it is possible to see that it is consistent for both methods of calculation. Based on these results, the suggested Z_{dr} bias is 0.75 +- 0.05 dB.

Z_{dr} and azimuth biases were found for CHIVO data during RELAMPAGO campaign and corrected for level 1a data. Z_{dr} shows a bias of 0.75 dB with an uncertainty of 0.05 dB. Also Z_{dr}

Table 3.2: Z_{dr} Bias using vertical pointing scans

Bias from birdbath (dB)	
2018/11/26	0.68
2019/01/26	0.70

bias shows a stable behavior during both the IOP and the extended period. Azimuth correction was done using three independent methods for consistency of the retrieval and to reduce uncertainties.

3.3 Radar Statistics

RELAMPAGO domain is known for having one of the highest storms in the world. Those storms can produce significant severe weather. During the three months CHIVO was in Argentina; it captured many interesting cases. In this section, I summarized the main cases during RELAMPAGO using radar parameters as a proxy of how severe a storm is. Those parameters are echo top and maximum reflectivity. The echo top refers to the height of the storms, storms whose echo top reaches more than the prevalent tropopause are considered tall storms. In the same way, storms that reach a maximum reflectivity higher than 65dBZ are considered important storms since 65dBZ is the NWS threshold for hail.

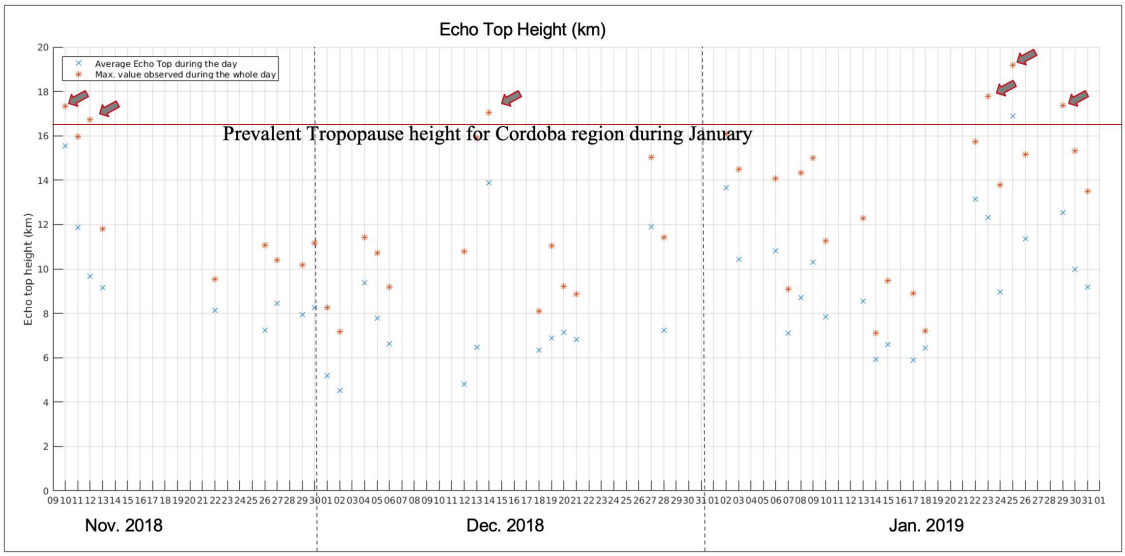

Figure 3.9: Echo top Statistic. Blue x is the average echo top and red star is the highest echo top observed during the day

Fig. 3.9 shows the echo top per day along the time CHIVO was collecting data in Argentina. Fig. 3.10 shows the maximum reflectivity. The arrows in fig. 3.9 correspond to those storms that reach an echo top higher than the prevalent tropopause for the RELAMPAGO domain during the summer.

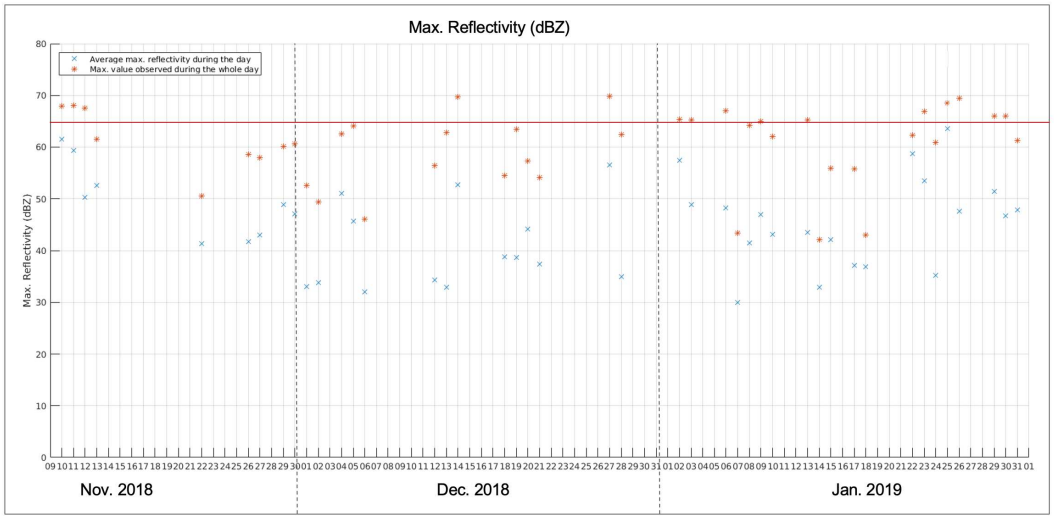

Figure 3.10: Max. Reflectivity Statistic. Blue x is the average max. reflectivity and the red star is the highest reflectivity observed during the day

Some of the highlights for the statistics are:

- During the IOPs, CHIVO observed reflectivity higher than 65 dBZ for five days. For the extended period, 9 days reached more than 65 dBZ. This is a clear indication of hail.
- From echo top, storms reached very high for three days during IOP and three days during the extended period.
- Storms that reached more than 65 dBZ and 16.5 km echo top are on 11/10, 11/12, 12/14, 1/22, 1/25 and 1/29.

- The maximum reflectivity and echo top were observed on Jan 25; On the same storm, CSAPR also observed very high reflectivity.

Chapter 4

Cross validation of the network of ground-based radar with space-borne radar during the RELAMPAGO field campaign

The cross-validation of radars in a network is important in making consistent retrievals across the domain and assuring the product quality. During the RELAMPAGO field campaign, two C-band radars, namely the Colorado State University C-band Hydrological Instrument for Volumetric Observations (CSU-CHIVO) and the C-band Scanning ARM Precipitation Radar (CSAPR-2), were deployed near the Sierras de Cordoba in Argentina, a region known for having some of the most intense severe weather in the world. In addition to these two radars, the operational radar of the Cordoba City, the Radar Meteorologico Argentino 1 (RMA-1), adds another instrument to the RELAMPAGO network. This study presents an intercomparison between the RELAMPAGO C-band radars using the GPM spaceborne radar as a common reference. A method to bring ground-based radars into better agreement is also proposed. Moreover, the attenuation correction for the C-band radar is studied in the context of intercomparing two radars. The attenuation coefficients are computed for the RELAMPAGO domain using the local disdrometers deployed during the campaign. After the attenuation correction, CSU-CHIVO, CSAPR-2, and RMA-1 compare well with GPM-DPR with a high correlation and bias less than 1 dB. [1]

[1]The content of this chapter was adapted from: Arias, I., & Chandrasekar, V. (2021). Cross validation of the network of ground-based radar with GPM during the Remote sensing of Electrification, Lightning, And Mesoscale/microscale Processes with Adaptive Ground Observations (RELAMPAGO) field campaign. Journal of the Meteorological Society of Japan. Ser. II, 99(6), 1423-1438.

4.1 Introduction

The RELAMPAGO field campaign took place near the Sierras de Cordoba (SdC) in Argentina. The Tropical Rainfall Measuring Mission (TRMM) observations indicate that the SdC have some of the most intense severe weather on the planet (Zipser et al. [26]). Details about TRMM can be found in [27]. RELAMPAGO brought to Argentina a dense network of ground-based sensors to investigate deep convection. The word "Relampago" stands for lightning in Spanish, the primary language spoken in South America.

The SdC has raised the interest of scientists motivated by the strength and characteristics of its storms. Since the study presented by [26], satellite observations have been used to study the weather near the SdC. For instance, [28] used TRMM and GOES-12 to characterize the convention type in this region. They also studied the vertical structure of wide convective cores using the precipitation radar on board TRMM. Details about the precipitation radar on board TRMM can be found in [29]. [30] also used satellite observations to hypothesize the key ingredients for convection initiation near the SdC.

Satellite observations have helped elucidate the storm characteristics that lead to such severe weather near the SdC. Nevertheless, ground observations are still needed to complete the picture. The RELAMPAGO field campaign was motivated by the fact that the SdC can be used as a natural laboratory to further our understanding of deep convection.

RELAMPAGO brought an interdisciplinary group of scientists and many sensors to Argentina. Two C-band radars were deployed near the SdC to investigate the terrain influence on deep convection. The operational radar of Cordoba City adds another instrument to the network of fixed radars that were collecting dual-polarization observation during RELAMPAGO.

RELAMPAGO occurred during the austral warm season of 2018 and had an intense observation period (IOP) from November to December of 2018. The campaign had an extended period (EOP) in January of 2019. During both observation periods, the Global Precipitation Mission (GPM) core observatory made several overpasses over the SdC. With the dense network of ground-based

sensors deployed during the campaign, RELAMPAGO provides a valuable opportunity for ground validation. Details about the GPM mission can be found in [31]; [32].

In this study, we provide a comprehensive analysis evaluating the ground-based radar (GR) during RELAMPAGO using the Dual-frequency Precipitation Radar (DPR) on board the GPM core observatory. Moreover, DPR is used as a common platform between the GRs to see if it can be used to bring them into a better agreement. The comparison of the GRs with DPR is used as an evaluation of the attenuation correction procedure used for the C-band radars. Details about DPR can be found in [33]; [34]; [35]; [36]).

The remainder of this chapter is organized as follows: Section 4.2 describes the network of GRs deployed during RELAMPAGO, presents an overview of the GPM DPR overpasses during the campaign, and discusses important aspects of the data analysis; Section 4.3 explains the procedures for comparing the GRs between themselves and with DPR, and also presents some considerations regarding the procedure limitations; Section 4.4 shows the comparison results of the different platforms, and presents a procedure for computing a more consistent bias in the radar networks; Section 4.5 offers a discussion of the results; and Section 4.6 our conclusions.

4.2 The RELAMPAGO radar observation

This section describes the radars used in our study, and the GPM DPR overpasses during the RELAMPAGO campaign. The attenuation correction procedure to compensate the C-band reflectivity is also explained.

4.2.1 The network of C-band radar

Three C-band radars in the RELAMPAGO domain were used in this study. These radars collected data during the IOP and the EOP. CSU-CHIVO and CSAPR-2 were brought to Argentina, and deployed near the SdC. The RMA-1 is the operational radar of Cordoba City. All three are C-band radars with dual-polarization capabilities.

Figure 4.1: CSU-CHIVO deployed south of Cordoba City, Argentina, during RELAMPAGO.

CSU-CHIVO is a research radar from Colorado State University (CSU). Figure 4.1 shows a picture of CSU-CHIVO deployed south of Cordoba City. CSU-CHIVO started operating on November 10th, 2018 and it was scanning until January 31st, 2019.

Figure 4.2: ARM mobile facility deployed during CACTI-RELAMPAGO. Sensors left to right: Sonic Detection and Ranging wind profiler (SODAR), C-band Scan Precipitation Radar 2 (CSAPR-2), X and Ka band Scan ARM Cloud Radars (XSACR and KaSACR), and Ka-band Zenith Radar (KAZR).

CSAPR-2 was deployed as part of the Clouds, Aerosols, and Complex Terrain Interactions (CACTI) project. CACTI is RELAMPAGO's sister project funded by the US Department of En-

ergy (DOE). CACTI brought many sensors to Argentina to study orographic clouds and their representation in multi-scale models. RELAMPAGO and CACTI overlapped in time, and both deployed sensors near the SdC. Figure 4.2 shows CSAPR-2 radar located by the radome on top of the containers. As shown in Fig. 4.2, the CSAPR-2 site also contains other atmospheric sensors, such as a wind profiler, and a cloud radar.

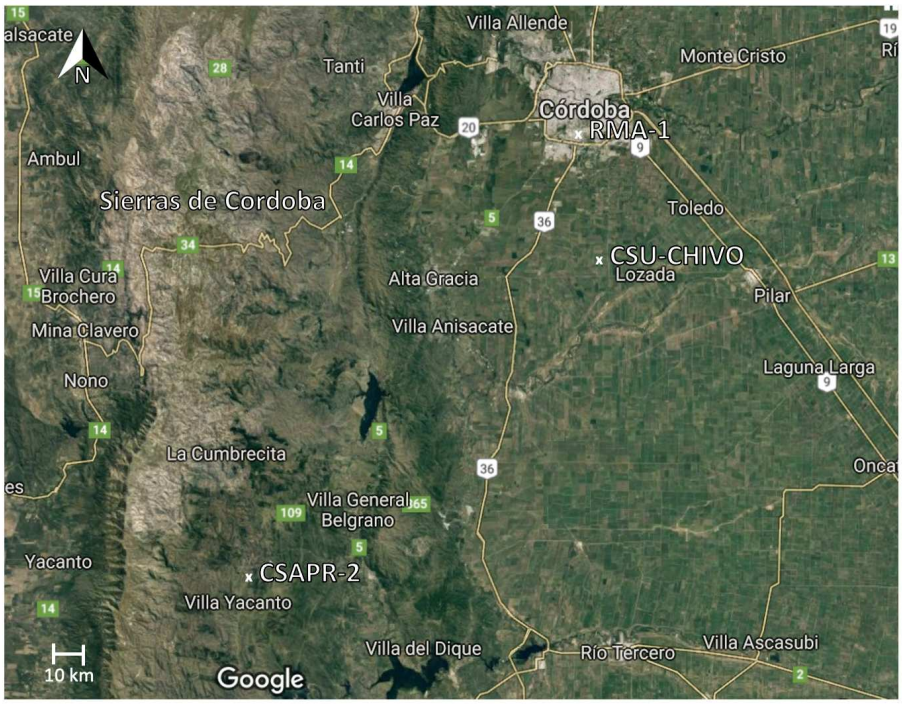

Figure 4.3: Map with the locations of the network of C-band radars during the RELAMPAGO campaign (CSU-CHIVO, CSAPR-2, and RMA-1).

Figure 4.3 depicts the location of the GRs used in this study. CSU-CHIVO is located at 31.63° S latitude, 64.17° W longitude, and 421 m altitude above mean sea level (AMSL); CSAPR-2 coordinates are 32.13° S latitude, 64.73° W longitude, and 1141 m altitude AMSL. RMA-1 is at 31.44° S latitude, 64.19° W longitude, and 484 m altitude AMSL.

In this study, we will denote CSU-CHIVO by CHIVO, CSAPR-2 by CSAPR, and RMA-1 by RMA for simplicity of notation.

CHIVO and CSAPR are approximately 80 km apart, while CHIVO and RMA are approximately 25 km away from each other. The distance between RMA and CSAPR is approximately 120 km.

4.2.2 Attenuation correction for the ground radars

The C-band reflectivity needs to be corrected for attenuation before being used quantitatively [11]. Therefore, the measured reflectivity (Z_m) can be lower than the intrinsic reflectivity (Z), especially in precipitation.

In dual-polarization radars, the specific differential phase (K_{dp}) can be used to account for attenuation. K_{dp} is related to the volume's liquid water content. The following equation shows an estimation of the attenuation using K_{dp} [11]:

$$A_H = \alpha K_{dp}^b \,, \tag{4.1}$$

where A_H is the attenuation in the horizontal channel, and α, b are the reflectivity attenuation coefficients.

Considering the attenuation, the measured and intrinsic reflectivity at a range r can be expressed in dB as follows:

$$Z_m(r) = Z(r) - 2\int_0^r A(S)dS \,, \tag{4.2}$$

where the factor two in the integral means that the attenuation is accounted twice since the signal is attenuated in both directions, from the radar to the target and vice versa. Replacing Eq. (4.1) in (4.2) and assuming $b = 1$, it yields that:

$$Z_m(r) = Z(r) - 2\alpha\int_0^r K_{dp}(S)dS. \tag{4.3}$$

Since K_{dp} is the derivative of the differential phase Φ_{dp} along with the range, Eq. (4.3) can be expressed as:

$$Z_m(r) = Z(r) - 2\alpha[\Phi_{dp}(r) - \Phi_{dp}(0)]. \tag{4.4}$$

Thus, the intrinsic reflectivity can be estimated as:

$$Z(r) = Z_m(r) + 2\alpha[\Phi_{dp}(r) - \Phi_{dp}(0)]. \tag{4.5}$$

The coefficient α can be computed using scattering simulations. Given a drop size distribution (DSD), one can simulate K_{dp} and A_H, with K_{dp} in deg/km and A_H in dB/km. The slope from a linear regression with intercept in the origin would be the α-value. The DSD can be simulated with a Gamma distribution or it can be measured by disdrometer.

In [11], the value of α for C-band is reported as 0.073. This value was computed by averaging scattering simulation of a wide variety of Gamma DSD. They also varied the simulation temperature from 0 to 30 C and took the average to compute the α-value.

We derived the α-value from measured DSD using data from the DOE 2-dimensional video-disdrometer deployed near CSAPR during the campaign [37]. The scattering simulations from DSD collected during November and December of 2018 were computed. The simulations were performed using the T-matrix procedure and a temperature of 10 C. An α-value of 0.15 was found for the C-band scattering simulation of the measured DSD.

In the remainder of the chapter, we will refer to the RELAMPAGO coefficients as those computed using the local disdrometer deployed during RELAMPAGO. The global average coefficients are referred to as those reported by [11].

4.2.3 Overview of the GPM overpasses

TRMM provided the observation to point out the SdC as a natural laboratory to further our understanding of deep convection. However, the TRMM mission ended by the time of the campaign. Nevertheless, its successor, GPM was capturing many interesting cases in different precipitation regimes with a dual-wavelength capability.

Table 4.1: List of GPM DPR overpasses during RELAMPAGO with significant weather. The Radar column means the GRs that capture the overpass with a good alignment in time and space with GPM DPR.

Date	Time (UTC)	Radar
2018/12/06	05:22	CHIVO/RMA
2019/01/13	04:01	CHIVO
2019/01/31	22:35	CSAPR

Table 4.1 lists the GPM DPR overpasses during RELAMPAGO with significant weather. The December 6th and January 13th overpasses covered the CHIVO domain, while the January 31st overpass covered the CSAPR domain. The December 6th overpass also covered the RMA domain.

A Range Height Indicator (RHI) taken during an overpass provides a valuable opportunity for vertical analysis. An RHI observes a vertical cross-section of the storm seen by a radar. During RELAMPAGO, CHIVO and CSAPR scan strategy included RHI.

On December 6th, 2018, the CHIVO RHI along the 315° azimuth overlapped significantly well with DPR Ku-band (KuPR) along angle bin 39. Figure 4.4a shows the location of this RHI in a solid line and KuPR angle bin 39 in dashed line. Figure 4.5 illustrates the vertical section from both platforms. Note that the vertical structure of the storms shows similar patterns, adjusting for their respective resolutions. For instance, the bright band is located at approximately 2.5 km elevation.

GPM DPR captured a group of convective cells over the CHIVO domain on January 13th, 2019. The CHIVO RHI in azimuth 192° overlapped significantly well with KuPR angle bin 13. Figure 4.6 shows a vertical cross-section of the storm from DPR (Fig. 4.6a) and CHIVO (Fig. 4.6b). The solid and dashed lines in Fig. 4.4b represent the locations of the RHI and the KuPR angle bin, respectively, for this case. Figure 4.6a.i shows the KuPR reflectivity whereas Fig. 4.6a.ii depicts the Dual Frequency Ratio (DFR). The DFR is computed from the DPR Ku and Ka equivalent reflectivity (Z_e).

Figure 4.6b shows the CHIVO observations for the January 13th, 2019 case. Note that the core of the cell, located at 65 km from CHIVO and at latitude -32.2 for DPR, exhibits interesting features. Reflectivity is significantly high below 8 km for both platforms, and the column has

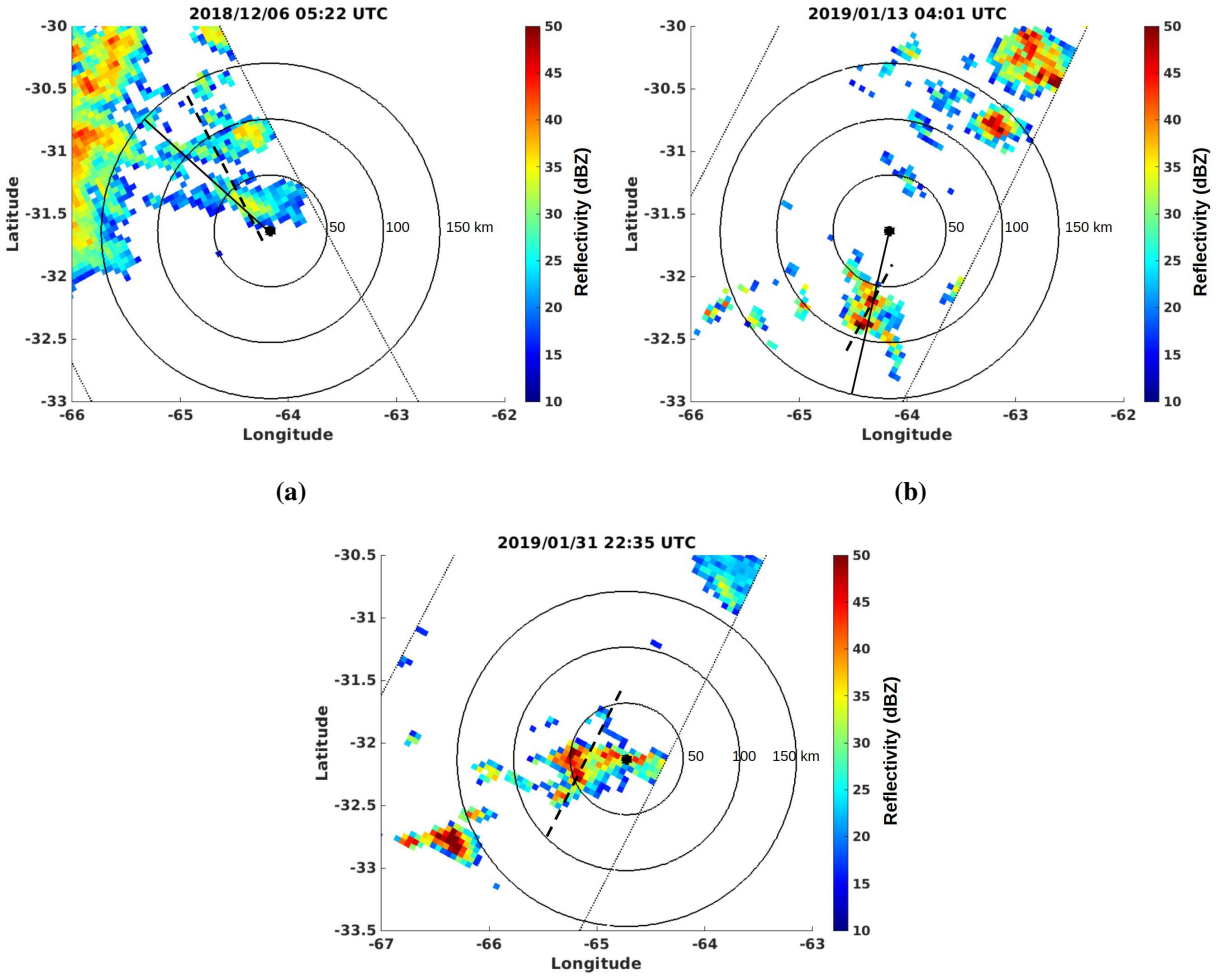

Figure 4.4: KuPR reflectivity at 2 km altitude on (a) December 6th, 2018 at 05:22 UTC, (b) January 13th, 2019 at 4:01 UTC, and (c) January 31st, 2019 at 22:35 UTC. The solid line in (a), and (b) indicates CHIVO RHI along 315°, and 192° azimuth respectively. The dashed line in (a), (b), and (c) denotes KuPR angle bins 39, 13, and 37 respectively. The doted lines represent the edges of the KuPR swath. The rings in (a), and (b) are centered at CHIVO, whereas for (c) are centered at CSAPR.

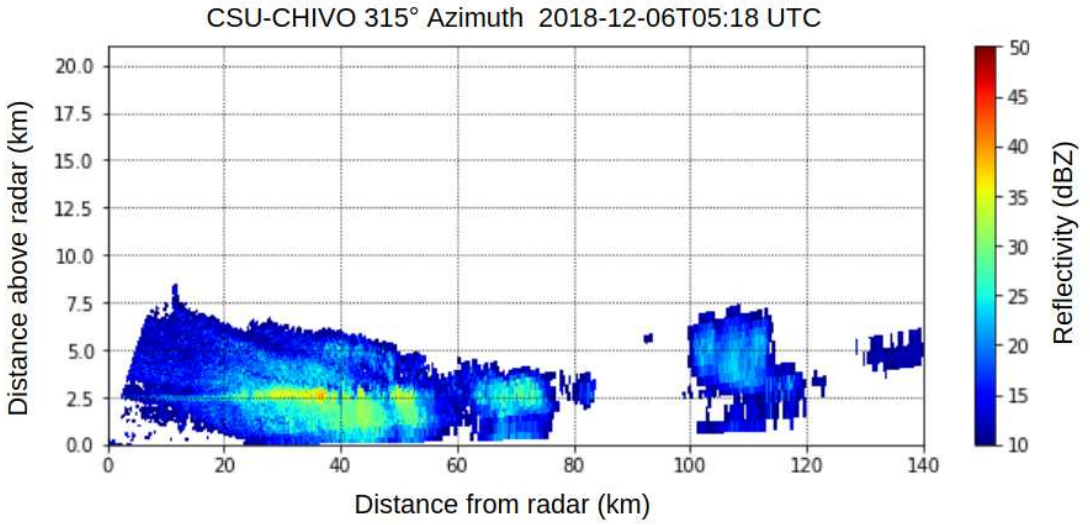

(a)

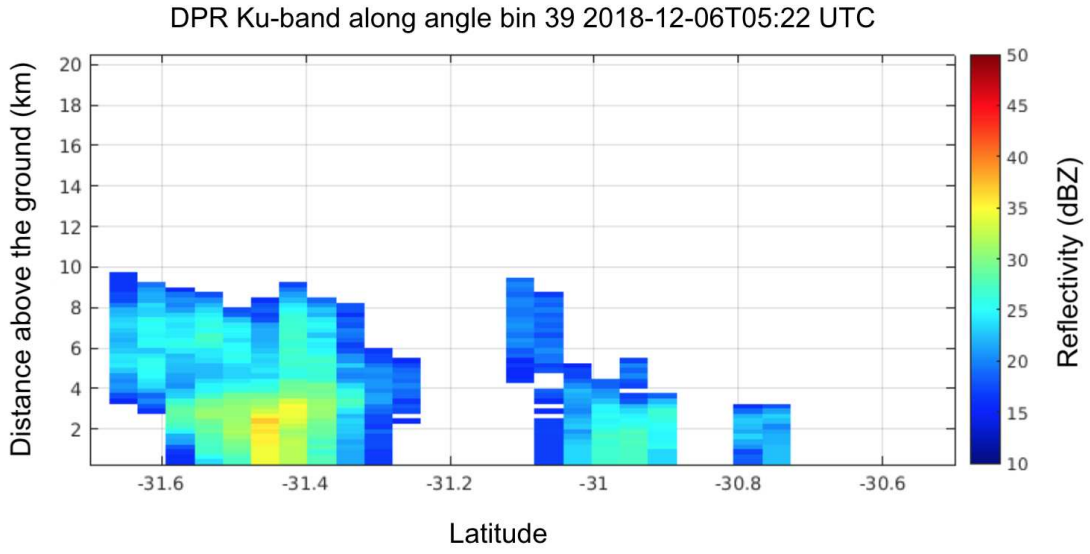

(b)

Figure 4.5: December 6th, 2018 reflectivity from: (a) CHIVO RHI along 315° azimuth at 05:18 UTC, and (b) KuPR along angle bin 39 at 05:22 UTC. The CHIVO RHI and DPR angle bin are marked by the solid and the dashed line in Fig. 4.4a.

a remarkable high DFR that coincides with high K_{dp} and differential reflectivity. Hydrometeor classification from CHIVO shows heavy rain below 5 km for this column.

GPM DPR did not have overpasses in the CSAPR domain during the IOP. However on January 31st, 2019, it recorded an overpass with CSAPR while deep convective cells were in the radar domain. Figure 4.7 shows a 3D depiction of the KuPR reflectivity collected over CSAPR domain. The dashed line in Fig. 4.4c and Fig. 4.7 correspond to KuPR angle bin 37. Note from Fig. 4.7 that the storm was very deep and localized.

4.3 Inter-comparison of the RELAMPAGO network of ground-based radars with GPM

This section describes the methods of comparing the radars in the RELAMPAGO network with each other and with DPR. The cross-comparison is done using the KuPR radar. The term "precipitation radar" (PR) in this chapter refers to a radar on board a space aircraft to measure precipitation. The methodology for cross-comparing a PR with a GR is first explained. Some considerations are then analyzed in terms of the resolution and how it can affect the results. Finally, a simple method of inter-comparing ground-based radars is proposed.

4.3.1 Cross-comparison with GPM

Quantitative comparison between DPR on board the GPM core observatory and GRs is challenging. Many aspects must be considered, such as time and space alignment.

In terms of the time alignment, when the GPM core observatory passes over the GR domain, their time difference must match well to obtain valid results. The GPM core observatory orbits the Earth at a speed of 7 km/s (Skofronick-Jackson et al. [31]). At this pace, the GPM core observatory covers the GR domain in approximately 30 s. Meanwhile, it takes a few minutes for a GR to fully scan its domain. Therefore, an overpass close to the middle of the start and end times of a GR scan is desired.

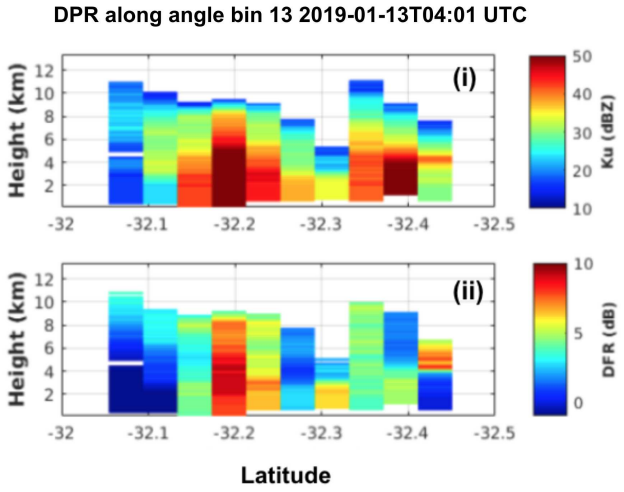

(a)

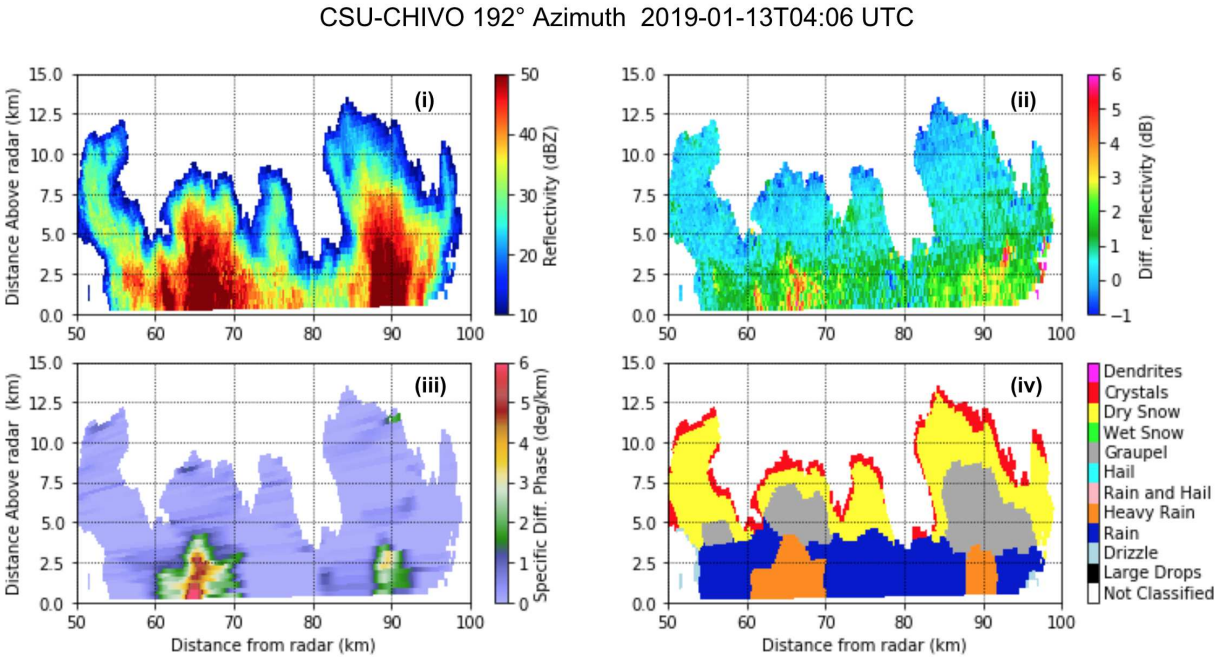

(b)

Figure 4.6: January 13th, 2019. (a): DPR along angle bin 13 at 4:01 UTC, Ku-band reflectivity (i), and Dual Frequency Ratio (DFR) (ii). (b): CHIVO RHI along 192° azimuth at 4:06 UTC, reflectivity (i), differential reflectivity (ii), specific differential phase (iii), and hydrometeor classification (iv).

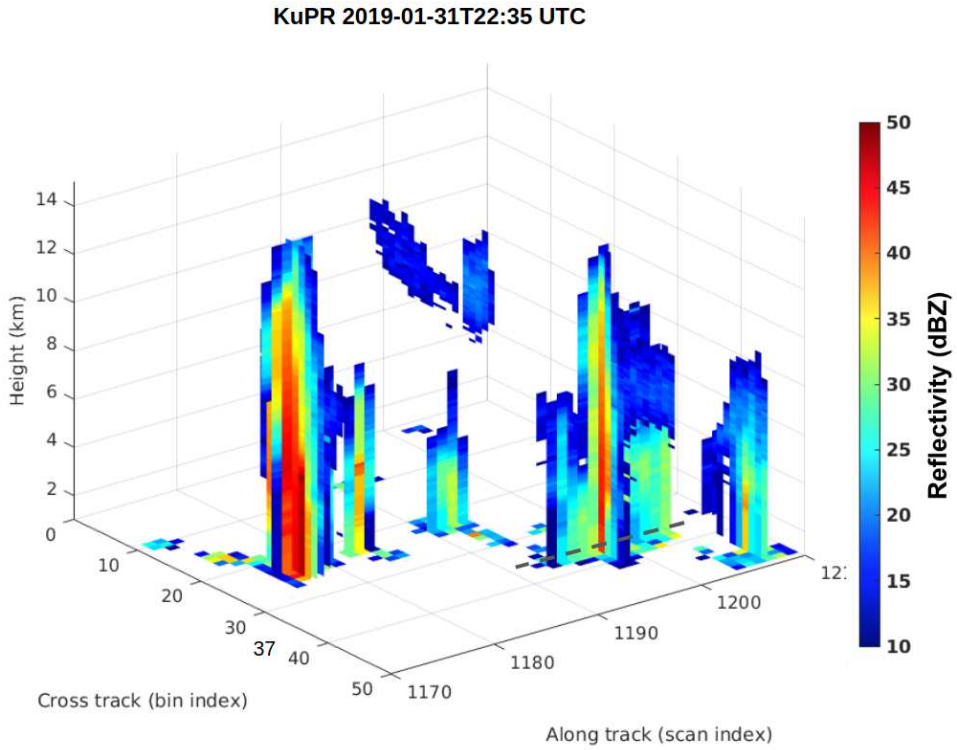

Figure 4.7: KuPR reflectivity on January 31st, 2019 at 22:35 UTC, 3D depiction.

Table 4.2: Resolution of spaceborne and ground-based radar used in this study.

Radar	Beam-width (deg.)	Pulse duration (μs)	Range resolution (m)	Footprint
KuPR	0.72	1.6/3.2	250/500	5 km at 400km
CSU-CHIVO	0.95	1.0	150	994 m at 60 km
CSAPR-2	0.90	0.7	100	942 m at 60 km
RMA-1	0.87	3.0	450	911 m at 60 km

The considered GRs have a beam width of approximately 1 degree. At a 60 km range, the vertical resolution of a GR with this characteristic would be approximately 1 km. In the case of DPR, [38] showed with real data that the beam width of KuPR is approximately 0.72 degrees. With this beam width and measuring precipitation at approximately 400 km, KuPR has a footprint of approximately 5 km.

The pulse duration is related to the range resolution of a radar. The range resolution determines what is the vertical and horizontal resolutions for a PR and a GR respectively. A PR scans from space; thus the range resolution indicates the vertical resolution in the data. Differently, for a GR, the range resolution designates the horizontal resolution.

Table 4.2 summarizes the PR and GR resolution used in this study. The PR and the GRs have a better range resolution than a footprint. Since both platforms observe the weather from different perspectives, these variables represent different quantities in their data.

Due to the difference in their geometries, a volume matching is needed to cross-compare DPR and a GR. Moreover, since the spaceborne radar is moving, it can have issues related to its orbits such as roll, pitch, and yaw. Most of these issues have been addressed for TRMM by [39]. In addition, [40] and [41] have analyzed extensively the techniques for comparing ground and spaceborne radar. As a legacy from TRMM, these methods can be used for DPR.

The tools developed by [39] and implemented by [42] are used for volume matching. This algorithm matches both platform data per GR sweep, and takes the PR beam projection in the GR sweep. It then averages the gates along the PR beam that intersect with the GR sweep in the vertical. For the GR, it averages all the gates in azimuth and range that intersect with the PR beam.

This procedure is done for each GR sweep and then for each PR beam. In this way, the algorithm computes the average reflectivity for the matched volumes.

While very practical, the procedure used by [42] has some limitations in terms of the spatial distribution of the storm and the resolution of each platform. The volume matching is done using the coarsest resolution for each platform, i.e., the PR horizontal resolution (5 km) and the GR vertical resolution (1 km). This has many implications when comparing both platforms. For example, in the edges of the storm, non-uniform beam filling can affect the PR approximation with respect to the GR. On the other hand, rapid changes in the vertical structure of the storm, such as in the melting layer or in convection, can affect the GR approximation with respect to the PR. Nevertheless, good results have been obtained using the procedure of [42].

Previous studies have compared GRs with space-borne radars individually. For instance, [43] compared the reflectivity from DPR with GRs in different precipitation regimes. The GRs used by [43] are part of the USA's NEXRAD network, and they are located in different cities. Similarly, other studies, such as that presented by [44], used spaceborne radars as a reference to calibrate GRs situated in different Australian cities. In addition, [45] used a comparison with DPR to derive absolute calibration for GR reflectivity.

The evaluation of GRs measurement with other ground measurements is important when comparing GRs with spaceborne radars because one can understand the error structure better. It also provides more insight into whether biases are from the cross-comparison with the space-borne radar or inherent to the GRs measurement. A good solution is to compare a GR with another GR. However, GRs need to be located nearby.

4.3.2 Inter-comparison of ground radars

The network of GRs deployed during the RELAMPAGO campaign is very valuable for GPM ground validation. A dense radar network was placed in a relatively small domain. Therefore, these radars can be compared with each other. In this study, we inter-compare each of the C-band radars deployed during RELAMPAGO.

The inter-comparison of the radars is performed by creating a common Cartesian grid. The grid origin is selected to be in the middle of the GRs to be compared, such that it equally compensates for the variation in the volume for each radar. A widespread stratiform case is used since it provides more stable conditions in terms of the storm variability.

The grid size is chosen to be 16 km square. The vertical extent of the grid is 1.2 km. The horizontal resolution is selected to be the CHIVO range resolution, i.e., 150 m. While the vertical resolution is chosen to be 600 m.

Only data below the melting layer is used because the melting layer introduces variabilities to the comparison due to strong spatial gradients. The melting layer is found using RHIs scan from CHIVO. In addition, only data above 1.2 km AMSL is used to avoid ground clutter. Since the grid vertical extent is 1.2 km, precipitation from 1.2 to 2.4 km AMSL is used to compared two GRs.

A widespread stratiform covers the GRs domain at around 3:30 UTC of November 30th, 2018. Data acquired around this time is used to perform the inter-comparison. Figure 4.8 shows CHIVO reflectivity for this case. Note from the RHI in Fig. 4.8b that the melting layer is located around 2.5 km above the ground level (AGL).

The metrics used to compare the reflectivity of a pair of radars are the bias, Pearson correlation coefficient (CORR), and the root mean square error (RMSE), which are defined as follows:

$$\text{BIAS} = E[Rd_X - Rd_Y]\,, \tag{4.6a}$$

$$\text{CORR} = \frac{Cov(Rd_X, Rd_Y)}{\sigma_{Rd_X}.\sigma_{Rd_Y}}\,, \tag{4.6b}$$

$$\text{RMSE} = E[(Rd_X - Rd_Y)^2]^{1/2}\,, \tag{4.6c}$$

where $E[.]$ is the expected value, Rd_X is the radar X and Rd_Y the radar Y. $Cov(.)$ is the co-variance, and σ_R is the standard deviation.

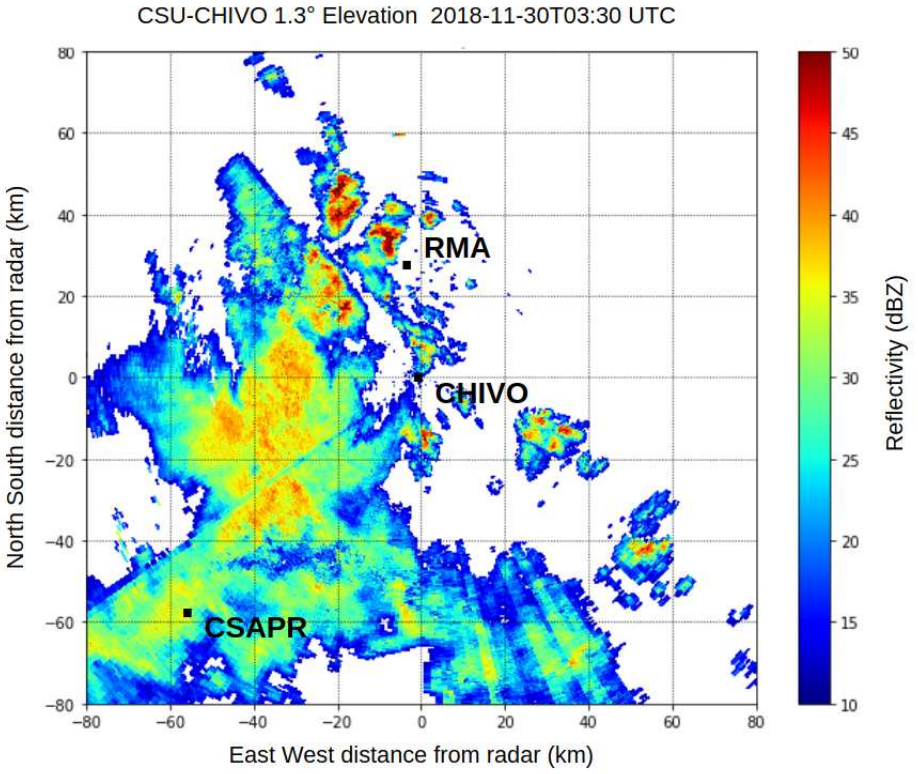

(a)

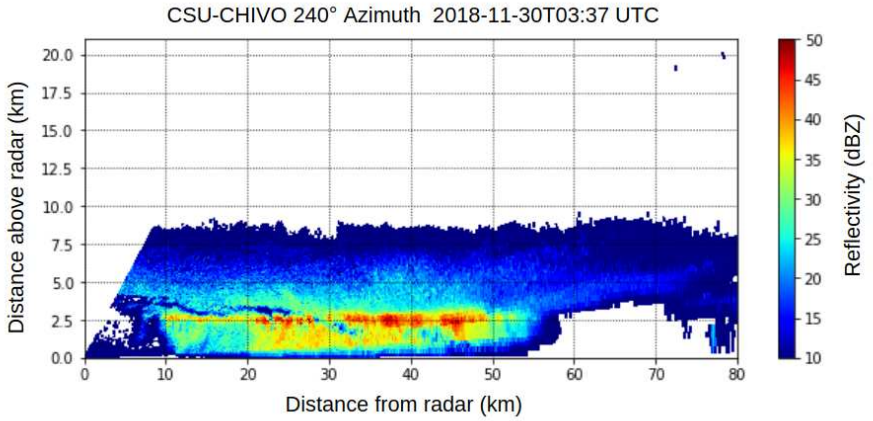

(b)

Figure 4.8: CHIVO reflectivity on November 30th, 2018. (a) PPI scan at 3:30 UTC, and (b) RHI scan at 3:37 UTC.

4.4 Results of the inter-comparison of the RELAMPAGO network of radars with GPM

Comparisons between the radars in a network is important in making consistent retrievals across the study domain. This verification assures the quality of the results and provides a more solid background for quantitative observation. In this section, we inter-compare the GRs deployed during RELAMPAGO. We use DPR as a common platform across the radars in the network. Error and bias are also computed based on DPR comparison.

4.4.1 Cross-comparison of the ground-based radar with GPM

To compare the RELAMPAGO GRs with GPM DPR, we initially perform attenuation correction to the reflectivity of each GR. The attenuation is estimated using the K_{dp} relationship presented in Eq. (4.1). The global average value of the coefficient α in this equation is reported by [11] as 0.073. However, we obtained a higher value of α (0.15) using local disdrometers deployed during the campaign.

The difference in the RELAMPAGO and the global average coefficient leads into the question of which value shall be used to correct the RELAMPAGO GR reflectivity. To answer this question, we perform attenuation correction to the CHIVO reflectivity using each coefficient separately. Then, the corrected reflectivity is compared with the KuPR reflectivity. It is worth noting that we use the KuPR corrected reflectivity available in the level 2A data set as the PR reflectivity. Figure 4.9 shows the cross-comparison of CHIVO with DPR for the overpass on January 13, 2019.

Figure 4.9a shows the comparison using the global mean coefficient reported in the literature. In this figure, it is possible to see that the CHIVO reflectivity deviates from the KuPR as the reflectivity yields higher values. The bias between KuPR reflectivity and CHIVO is 0.71 dB, the correlation coefficient is 0.94 and the RMSE is 2.4 dB in this case.

On the other hand, Fig. 4.9b shows the comparison using the local RELAMPAGO domain coefficient. In this figure, it can be seen that the CHIVO reflectivity matches well with KuPR reflectivity even for high values. The bias between KuPR reflectivity and CHIVO is 0.1 dB, the

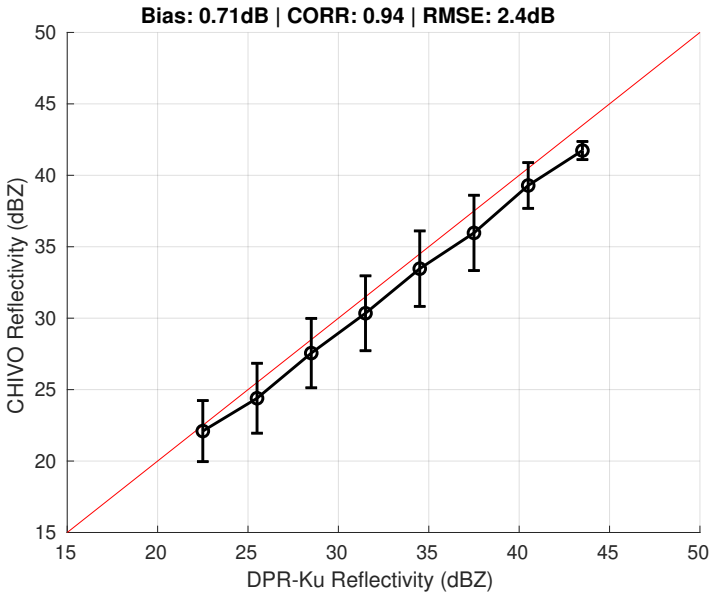

(a)

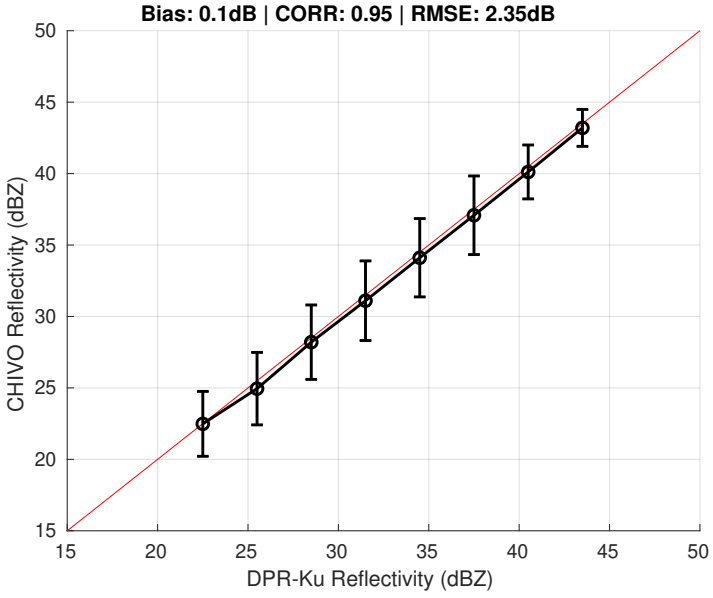

(b)

Figure 4.9: CSU-CHIVO and KuPR reflectivity comparison for January 13, 2019 case at 4:02 UTC. CHIVO reflectivity is corrected for attenuation using (a) global average coefficient, and (b) coefficient computed from the disdrometer in the field. The dots represent the mean and the bars depict one standard deviation.

Table 4.3: Summary of the cross-comparison with KuPR of the ground-based radars during RELAMPAGO. The time is for the overpass. The bias, correlation coefficient, and RMSE are computed as defined in the set of Eq. (4.6) where Rd_X is KuPR and Rd_Y is the GR. The Samples column refers to the number of points used in the comparison.

Date	Time (UTC)	Radar	Bias (dB)	Corr.	RMSE (dB)	Samples
2018/12/06	05:22	CHIVO	0.17	0.89	1.94	776
		RMA	-1.16	0.82	3.01	1104
2019/01/13	04:01	CHIVO	0.10	0.95	2.35	458
2019/01/31	22:35	CSAPR	0.93	0.87	3.04	946

correlation coefficient is 0.95 and the RMSE is 2.35 dB in this case. A higher correlation and a lower RMSE is observed when using the RELAMPAGO coefficient compared to the results obtained using the global coefficient. Similar results were also obtained with a different overpass on December 6th, 2018 for CHIVO.

Table 4.3 summarizes the cross-comparison of the RELAMPAGO GRs with KuPR using the RELAMPAGO coefficient. In the table, CHIVO shows almost no bias with respect to KuPR for both of its overpasses. CSAPR shows a positive bias, indicating that its reflectivity is slightly smaller than that of DPR. On the contrary, RMA shows a negative bias, which might indicate an overestimation of its reflectivity. It is worth mentioning that different GRs capture different overpasses. This difference might have an effect in the consistency of the comparison.

4.4.2 Inter-comparison of the ground radars

This section presents the results of the inter-comparison of the GRs used in our study. Similar to DPR cross-comparison, a better agreement between the radars was obtained using the RELAMPAGO coefficient. The inter-comparison is done for each pair of GRs, i.e., CHIVO vs CSAPR, CHIVO vs RMA, and RMA vs CSARP.

Figure 4.10 shows the scattergram of CHIVO and CSAPR reflectivity. Note that in the scattergram, the CHIVO reflectivity seems to be slightly higher than CSAPR. Nevertheless, they compare well with a high correlation and low RMSE.

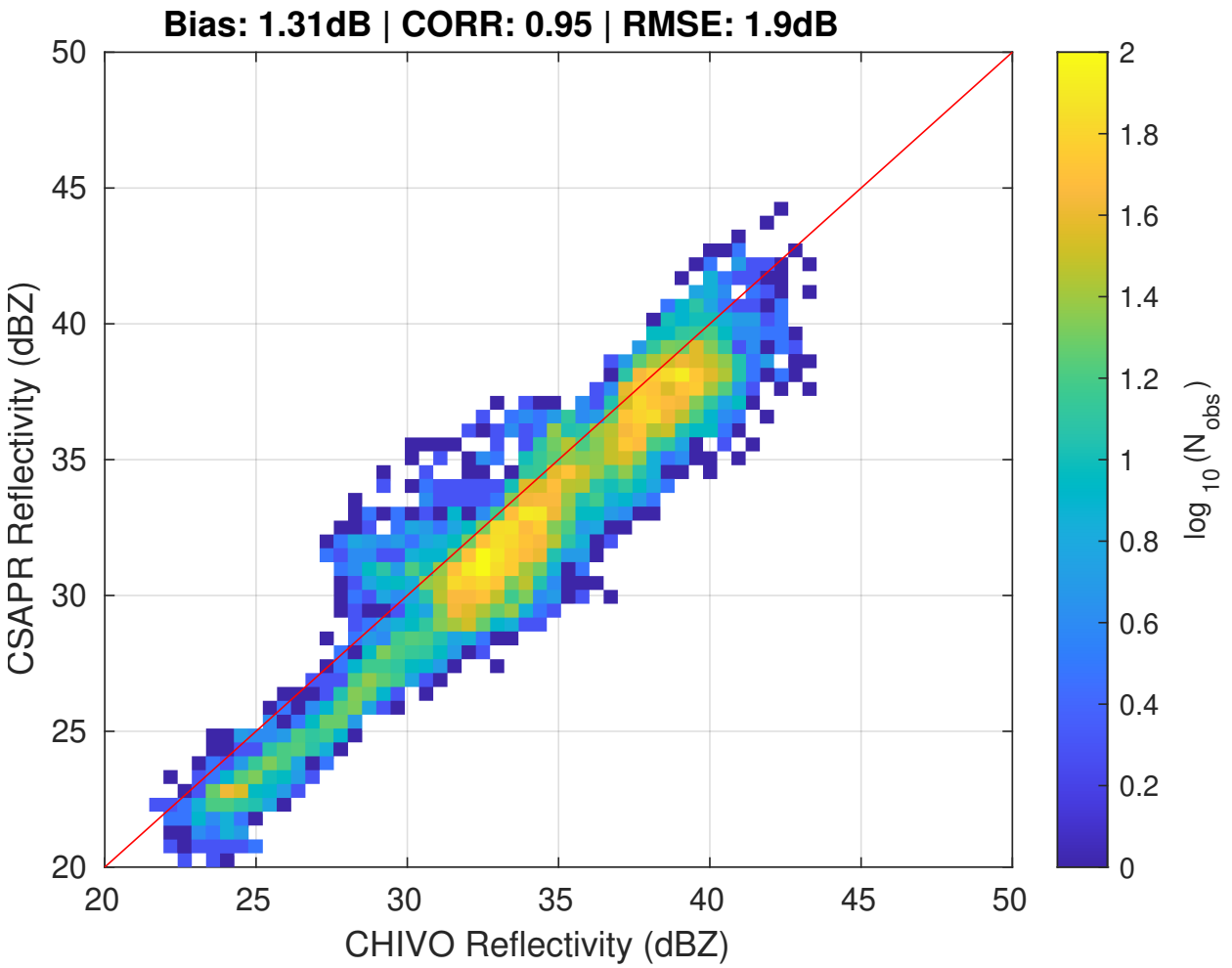

Figure 4.10: CSAPR-2 and CSU-CHIVO reflectivity comparison for November 30th, 2018 case at 3:30 UTC. CSAPR and CHIVO reflectivities are corrected for attenuation using coefficient computed from the disdrometer in the field.

Table 4.4: Summary of the inter-comparison between the ground-based radar on November 30th, 2018 case. The bias, correlation coefficient and, RMSE are computed as defined in the set of Eq. (4.6) where the order of radars is given by Rd_X vs. Rd_Y in the Radars column. The Samples column refers to the number of points used in the comparison.

Time (UTC)	Radars	Bias (dB)	Corr.	RMSE (dB)	Samples
3:30	CHIVO vs. CSAPR	1.31	0.95	1.90	7772
4:00	CHIVO vs. RMA	-0.95	0.85	2.57	7791
3:15	RMA vs. CSAPR	1.91	0.72	3.95	7539

Table 4.4 shows the results for the rest of radars. The inter-comparison between CHIVO and RMA exhibits a negative bias, which can be interpreted as a lower value in CHIVO reflectivity with respect to RMA. In the case of RMA vs CSAPR, the bias is now positive, indicating that RMA reflectivity is higher than that of CSAPR.

With the inter-comparison results, the question that arises is whether or not the GRs biases are consistent with the bias found with KuPR. The following section addresses this issue.

4.4.3 Bias consistency, analysis, and estimation

In the last subsections, each radar is compared with one another. A total of four radars are compared, including the KuPR. Tables 4.3 and 4.4 show the bias and the correlation coefficient for the cross and inter comparison respectively. Nevertheless, we would like to know if the results are consistent between different instruments. Therefore, we construct a visual representation in Fig. 4.11.

Figure 4.11 shows the results of the comparison in a directed graph. The vertices are the radars, while the edges are the comparison metrics. The edges show the bias in parenthesis and the correlation coefficient in square brackets. The direction of the arrows represents how the bias is computed, where the X radar is the beginning and the Y radar the end of the arrow. X and Y are specified as in Eq. (4.6a). Since CHIVO had multiple overpasses, we average their biases and correlations to construct the KuPR-CHIVO edge.

The graph is arranged in the form of a triangular based pyramid. KuPR is placed in the apex of the pyramid because it is a common platform across the network of radars. In other words, KuPR is used as a reference in the space to bring the other corners of the pyramid together. The GRs are placed in the pyramid's base to represent that they are ground-based sensors.

To have an insight into the bias consistency, one can take a walk around one of the pyramid faces and add the biases. Let us call the result of this summation the residual bias (δB) from a face. For example, take the phase formed by CHIVO-RMA-CSAPR. In this case, the residual bias is:

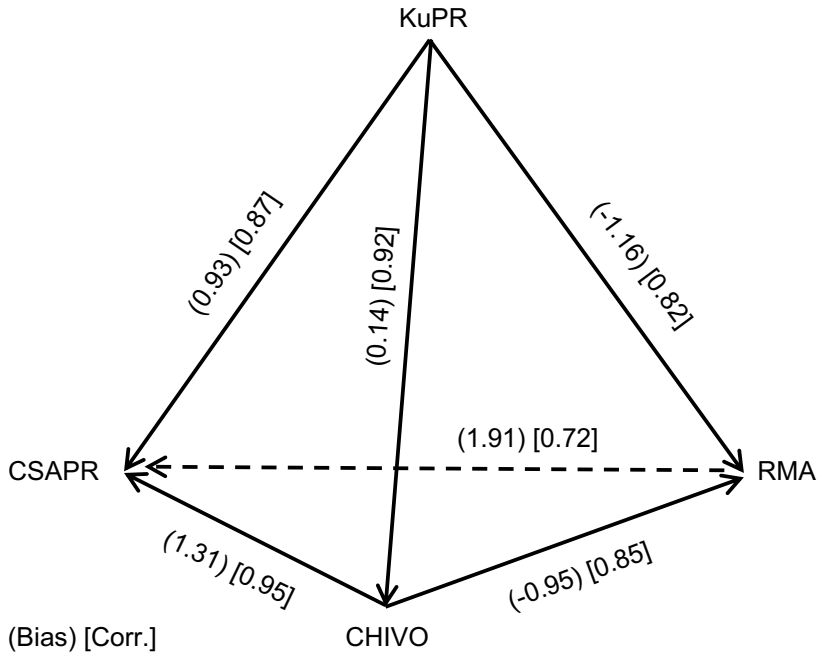

Figure 4.11: Bias (parenthesis, dB) and correlation coefficient (square brackets) from the cross and inter comparison. The arrows indicate the direction in which the bias is computed, being X the beginning and Y the end of the arrow.

Table 4.5: Residual bias (δB) for the faces of the graph in Fig. 4.11, and residual recalculated bias ($\delta\tilde{B}$) of the graph in Fig. 4.12.

Face	$\delta B(dB)$	$\delta\tilde{B}(dB)$
CHIVO-RMA-CSAPR	-0.35	0.09
CHIVO-RMA-KuPR	0.35	-0.11
CHIVO-KuPR-CSAPR	-0.52	0.17
KuPR-CSAPR-RMA	0.18	-0.03

$$\begin{aligned}\delta B &= B(CHIVO, RMA) + B(RMA, CSAPR) + B(CSAPR, CHIVO) \\ &= B(CHIVO, RMA) + B(RMA, CSAPR) - B(CHIVO, CSAPR) \\ &= (-0.95) + (1.91) - (1.31) = -0.35\,,\end{aligned} \tag{4.7}$$

where $B(Rd_X, Rd_Y)$ is the bias between the radars X and Y. Note that:

$$B(Rd_X, Rd_Y) = -B(Rd_Y, Rd_X) \tag{4.8}$$

because the way the bias is defined. This is the reason why B(CSAPR, CHIVO) is replaced by -B(CHIVO, CSAPR) in the second line of Eq. (4.7).

Intuitively, the residual bias of a face should be equal to zero because a radar's bias with itself is zero, or mathematically, $B(Rd_X, Rd_X) = 0$. Since one returns to the same radar after finishing a walk through the face, it is natural to expect that the biases will compensate along the vertices, and the residual bias would be zero. For example, in the walk through the CHIVO-RMA-CSAPR face, one starts with the bias from CHIVO to RMA and concludes with the bias from CSAPR to CHIVO (first line of Eq. (4.7)).

In this respect, computing the residual bias for each face can provide a sense of how consistent the comparison between the radars is. Table 4.5 shows the δB for each face of the graph in Fig. 4.11. The meaning of $\delta\tilde{B}$ in Table 4.5 will be explained later in this section. The residual biases are computed counter-clockwise in the direction specified by the order of the radar in the table. Note

that a switch in the clockwise direction only changes the residual bias sign; but the magnitude remains constant.

Table 4.5 shows the absolute maximum residual bias (max. $|\delta B|$) is 0.52 dB. This max. $|\delta B|$ can be interpreted as the comparison of each sensor to one another is consistent within half of a dB. More about this interpretation will be presented in the Discussion section.

Moreover, this confirms that we can use KuPR to bring the network of GRs into better agreement. A new bias between each pair of radars is recomputed. The new bias is found by averaging the sum of the biases from the paths connecting two radars in the graph. The averaging is weighted using the correlation coefficient. When a path has more than one edge, the correlation coefficient is found by multiplying the individual correlations.

For instance, to go from CHIVO to CSAPR, one can go directly, through KuPR, or through RMA. We did not include paths with more than one radar in between e.g., CHIVO-RMA-KuPR-CSAPR because they can induce more uncertainty in the estimation. Hence, the path's biases for the CHIVO and CSAPR example are given as:

$$\begin{aligned} B(CHIVO, KuPR, CSAPR) &= B(CHIVO, KuPR) + B(KuPR, CSAPR), \\ B(CHIVO, RMA, CSAPR) &= B(CHIVO, RMA) + B(RMA, CSAPR), \end{aligned} \tag{4.9}$$

where $B(Rd_X, Rd_Y, Rd_Z)$ is the sum of biases in the path that connect the radar X and Z passing through the radar Y.

Similarly, the correlation of the path connecting the radar X with Z passing through radar Y can be defined as:

$$Corr(Rd_X, Rd_Y, Rd_Z) = Corr(Rd_X, Rd_Y) \times Corr(Rd_Y, Rd_Z). \tag{4.10}$$

In this way, the correlation of the paths that go from CHIVO to CSAPR is given by:

Table 4.6: From CHIVO to CSAPR, biases using different paths. Bias is computed as shown in Eq. (4.9) where Rd_X is CHIVO, Rd_Y is CSAPR.

Path	Bias (dB)	Corr.
CHIVO-CSAPR	1.31	0.95
CHIVO-KuPR-CSAPR	0.79	0.80
CHIVO-RMA-CSAPR	0.96	0.61

$$
\begin{aligned}
&Corr(CHIVO, KuPR, CSAPR) = Corr(CHIVO, KuPR) \times Corr(KuPR, CSAPR),\\
&Corr(CHIVO, RMA, CSAPR) = Corr(CHIVO, RMA) \times Corr(RMA, CSAPR).
\end{aligned}
\tag{4.11}
$$

Table 4.6 shows the numeric values of the paths' bias and correlation connecting CHIVO and CSAPR. As expected, the direct path that connects CHIVO and CSAPR has the highest correlation because it doesn't go through any other radars. In contrast, the smaller biases going through KuPR and RMA suggest that the bias between CHIVO and CSAPR should be lower than the bias computed directly. Therefore, it makes sense to compute a new bias combining the biases from different paths. The correlation can then be used to weight the bias.

In the case of CHIVO and CSAPR, the bias can be recalculated as follows:

$$
\begin{aligned}
&\tilde{B}(CHIVO, CSAPR) =\\
&[B(CHIVO, CSAPR) \times Corr(CHIVO, CSAPR)+\\
&B(CHIVO, KuPR, CSAPR) \times Corr(CHIVO, KuPR, CSAPR)+\\
&B(CHIVO, RMA, CSAPR) \times Corr(CHIVO, RMA, CSAPR)]/\\
&[Corr(CHIVO, CSAPR) + Corr(CHIVO, KuPR, CSAPR)+\\
&Corr(CHIVO, RMA, CSAPR)],
\end{aligned}
\tag{4.12}
$$

where $\tilde{B}(Rd_X, Rd_Y)$ is the estimation of the new bias between the radar X and Y.

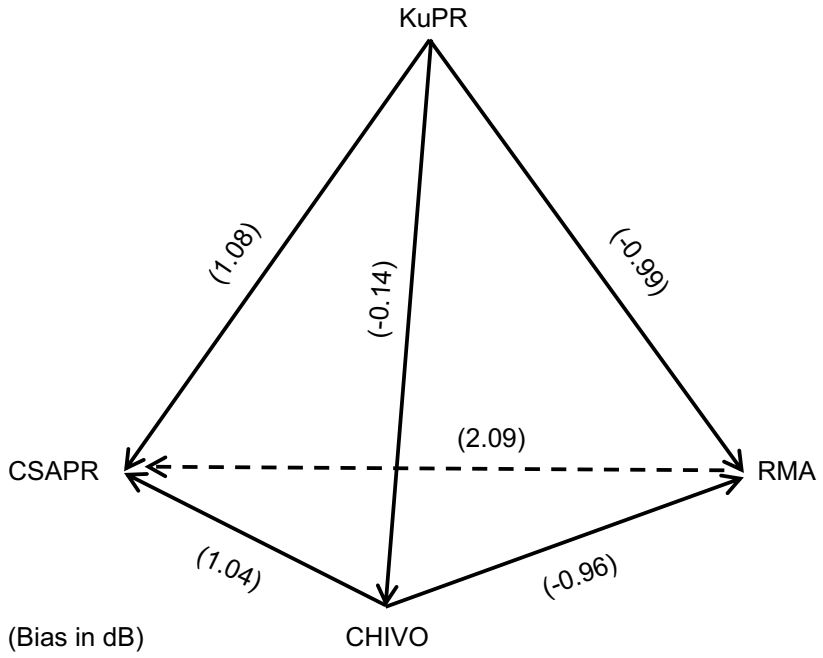

Figure 4.12: Recalculated bias using the information from the other path as in Eq. (4.12), the arrows are defined as in Fig. 4.11.

In a similar manner, the new biases are computed for the other edges of the graph and they are shown in Fig. 4.12. Table 4.5 lists the new residual bias ($\delta\tilde{B}$) for the faces of the graph in Fig. 4.12. Note that the the absolute maximum residual bias (max. $|\delta\tilde{B}|$) is 0.17 dB for Fig. 4.12 graph. This reduction in the max. $|\delta\tilde{B}|$ compared to the max. $|\delta B|$ from Fig. 4.11 can be interpreted as the new estimated biases are in a better agreement within the network.

4.5 Discussion

A discussion of the main results in this study is presented. First, the increase in the α-value in the RELAMPAGO domain is examined. Second, the residual bias as a measurement of the consistency of the bias in a radar network is explained. Finally, a procedure to find a more consistent bias in the network of radars is discussed.

We found a change in the α-value derived from the local disdrometer in the RELAMPAGO domain compared to the α-value reported by [11], which was derived from a global set of DSDs.

A comparison with KuPR suggests a better agreement using the RELAMPAGO α-value for the GR's attenuation correction. Almost a one-to-one agreement was observed for CHIVO using the RELAMPAGO coefficient. The results shown in Fig. 4.9 suggest that the higher the reflectivity, the lower the agreement for the global average coefficient.

The change in the RELAMPAGO α-value is due to the narrower domain of DSD for the local region. The RELAMPAGO domain is known for having some of the most intense convection on Earth. Disdrometer analysis shown by [46] reveals an increase in the normalized droplet concentration in the RELAMPAGO domain. This variation in the DSD in the RELAMPAGO domain makes more relevant the computation of the attenuation coefficients for this region.

The graphical representation shown in Fig. 4.11 helps us to have a better interpretation of the results. For example, CHIVO shows a good agreement with KuPR with a high correlation within 0.9 and almost unbiased reflectivity. CSAPR and RMA also compare well with KuPR with a correlation within 0.8 and approximately 1 dB bias. CHIVO also compares well with CSAPR and RMA with a high correlation within 0.85. The slightly low correlation between RMA and CSAPR was expected because the distance between these two radars is the longest.

The graph in Fig. 4.11 also suggests the residual bias's computation as shown in Eq. (4.7) for CHIVO-RMA-CSAPR face. The residual bias along the faces of the graph provides a sense of the consistency of the comparison. Ideally, the residual bias should be zero. An intuitive explanation is because in a close path one returns back to the starting point. As a result, δB can be seen as the "boundary condition", as instrument's bias with itself, i.e., zero.

As shown in Table 4.5, the maximum absolute residual bias in Fig. 4.11 is approximately half of a dB. The max. $|\delta B|$ can be seen as a measurement of the bias consistency between different instruments because each δB represents how consistent the bias is between three of the sensors. The results show a max. $|\delta B|$ of half of a dB, which can be interpreted as the mean uncertainty of the radars' comparison.

A method to find a more consistent bias in the graph is proposed. The bias between two radars is combined with the bias going through the other two radars in the graph. An example to compute

a new bias between CHIVO and CSAPR using the information from KuPR and RMA is presented in Eq. (4.12). The same procedure is applied to the other radars in the network, including KuPR.

The values of the new biases are presented in Fig. 4.12. The residual bias is found for the faces of the new graph, and it is shown in Table 4.5 in the $\delta\tilde{B}$ column. Note that there is a reduction in the residual bias for the recalculated graph. The lower $\delta\tilde{B}$ can be interpreted as the biases in the graph are more consistent between the different nodes.

4.6 Summary

We present an intercomparison of three radars with KuPR in this study. The intercomparison is done using the network of C-band radars deployed during the RELAMPAGO field campaign in Argentina. We also compare the GRs between each other. Each instrument is compared pairwise with one another, including KuPR. Evaluating the network consistency in itself is the unique aspect of this study, in addition to the comparison with KuPR.

The attenuation correction coefficients were computed from DSD measured by disdrometer deployed in the GRs domain during the field campaign to improve the accuracy of attenuation corrected reflectivity. The derived coefficients were slightly higher than the global average values reported in the literature. The bias between KuPR and the GRs reduces when the RELAMPAGO coefficients are used to correct attenuation.

We propose a method to evaluate the consistency of the bias in the network of GRs and KuPR. Previous studies compare each GR with KuPR individually. The GRs used in this study were located such that there was sufficient overlapping coverage regions that allowed a comparison between them. Therefore, we were able to compute the bias between each pair of instruments. The residual bias between three of the radars is used to have a sense of the biases' consistency. We also propose a method to compute a more consistent bias between two radars employing the other instruments' information.

Chapter 5

Attenuation in melting ice, implications for C-band radars

The melting ice attenuation in C-band radars is studied. Dual C-band radar observations from the RELAMPAGO campaign are used. Melting ice regions in the radar data are identified using spectral decomposition, Doppler winds, and hydrometeor classification. The attenuation in regions that display polarimetric signatures of melting is computed using a network-based approach. The network-based approach to computing the attenuation correction coefficients is validated by comparing with disdrometer data over rain. The attenuation correction coefficients over melting ice that were found compare well with the coefficients found in previous studies by simulations and direct comparison of C and S-band radar measurements. [2]

5.1 Introduction

The C-band is one of the most prevalent frequencies for radars in the tropics [6]; however, the C-band poses additional challenges for attenuation correction in tropical/subtropical climatologies due to frequently occurring convective storms. The C-band needs attenuation correction to obtain quantitative estimates from the radar measurements such as rainfall, especially in convection [9]. Melting ice formation is associated with the recirculation of ice particles in deep convection [47]. In addition, the melting ice produces an enhanced scattering that the attenuation correction algorithms cannot compensate for satisfactorily [3]. As a result, it has become more critical to study the effect of the melting ice in the attenuation to obtain quantitative estimates, especially in the tropics.

[2]The content of this chapter was adapted from: Arias, I., & Chandrasekar, V. (2023). Attenuation of Melting Ice at C-band Frequencies, Observed Using Dual Radar Measurements During the RELAMPAGO Campaign. IEEE Journal of Selected Topics in Applied Earth Observations and Remote Sensing (Accepted, in press). All rights reserved.

In addition to studying the melting ice because of its attenuation, the study of the melting ice itself is important to understand the microphysical processes occurring in convective storms that produce severe weather on the ground. The melting ice sheds large drops that can grow very fast in an updraft environment generating heavy precipitation. Furthermore, the melting ice advected into the updraft can provide the embryos to produce large hail with the potential of impacting the ground.

Previous studies by [48] have determined how ice melts in a controlled environment. This study used a wind tunnel setup to emulate the updraft. In this study, the suspended ice was let to melt, and its different stages while melting were recorded. It was found that when the ice starts melting, it develops a torus of water. Later, the melting ice sheds large drops when this torus becomes bigger. Subsequently, the melting ice stabilizes and becomes a very oblate large drop sustained by the core of ice inside. The ideal condition in [48] made the ice melt without interacting with other particles. This early study provides an excellent insight into how ice melts in an updraft condition.

Studies from dual polarimetric radar observations have documented very high values of Z_{dr} extended in the vertical in deep convection [47, 49]. [49] has attributed these high values of Z_{dr} to melting ice transported into new updrafts from mature convective towers. More recently, [47] characterized these high values of the differential reflectivity as a Z_{dr} column and explained how these high values are associated with strong updrafts that advect melting ice particles. The Z_{dr} column seems to be the product of large drops from a source other than regular warm rain formation. The high Z_{dr} return observed near the updraft is associated with the drops that the melting ice sheds. These large drops grow rapidly in the updraft rich in liquid water. These large drops are more oblate and produce the high return observed in the Z_{dr} column.

Enhanced scattering and attenuation have been reported in C-band radars, especially in convective conditions [10]. This study also proposed treating the attenuation correction differently in regions with enhanced attenuation. A piecewise correction is proposed in this study. The attenuation correction was increased in the regions with enhanced scattering. Another name for this piecewise correction is a hot spot [50]. This anomalous scattering could be caused by melting

ice particles and the large drops that they shed, which generate resonance in the C-band. This enhanced attenuation could also be due to enhanced absorption in the C-band of the melting ice particles.

The melting ice attenuation has been studied by comparing S and C-band measurements [3]. In this study, the S-band measurements are assumed to be unaffected by attenuation. The C-band measurements are then compared directly with the S-band measurements, and the attenuation is computed. However, scattering simulations from [51] and [52] shows that even when the S-band measurements are less affected by melting ice, these measurements still can attenuate. Nevertheless, this study provides a good insight into the attenuation of melting ice in the C-band.

A comprehensive scattering simulation in the C-band of melting ice has been carried out by [2, 53]. In these studies, a wide range of hail with different sizes was ingested into simulated updrafts. The melting ice microphysics was represented by the stages in [48], and the updraft environment was simulated using the spectral microphysical scheme developed by the Hebrew University. The scattering responses to the C-band of these melting ice particles were also analyzed in these studies. It was found in these studies an enhanced attenuation in the melting ice. This attenuation also displayed a wide variability in the simulations.

The previous work on melting ice mentioned so far has provided a good understanding of the melting ice processes and how they interact with the C-band signal. However, there are still significant unknowns of the factors that make the melting ice produce such a big and wide attenuation and the microphysical processes involved in the melting ice evolution in the updraft. The direct comparison of S and C band radar presented by [3] provides a great starting point to study the attenuation in the C-band caused by melting ice. Nevertheless, the melting ice also affects the signal in the S-band. On the other hand, the simulations conducted by [2, 53] represent in a very comprehensive way the updraft environments and the melting ice microphysics. Nevertheless, observations of the melting ice evolution are needed to validate the findings in these simulations.

In this article, the attenuation of melting ice is studied using the simultaneous observations of the network of C-band radars deployed during the RELAMPAGO campaign. A network-based

approach to compute the melting ice attenuation is also presented. Furthermore, this observation allowed the analysis of the microphysical processes involved in the melting ice evolution in an updraft environment and its interaction with the updraft. This network-based approach in the same band is suitable for studying attenuation because the radar's signals in the network interact similarly with the melting ice. As a result, a better estimation of the attenuation can be obtained. This network-based approach is also one of the new aspects of this study. The validation of this approach to computing the attenuation in the C-band is also presented.

This chapter is organized as follows. Section 5.2 presents the methods used to compute the attenuation and the radar analysis tools used to identify the melting ice. Section 5.3 presents the study case used to compute the melting ice attenuation. Section 5.4 presents how the melting ice is identified and how the attenuation is computed. The main findings of our study are discussed in section 5.5. This section also presents a conceptual model of the melting ice evolution in updrafts based on radar observations and how the attenuation of melting ice found in this study compares with previous works. Finally, section 5.6 shows our conclusions.

5.2 Methods

This section presents a background for the radar analyses and retrievals presented in this study. These radar analyses are performed to study the melting ice attenuation using simultaneous observations from the network of C-band radars deployed during the Remote sensing of Electrification, Lightning, And Mesoscale/microscale Processes with Adaptive Ground Observations (RELAMPAGO) field campaign. More about the RELAMPAGO campaign will be expanded in the Data section. These simultaneous observations in the C-band are used to retrieve advanced radar estimates such as the network-based attenuation and the Doppler wind. In addition, the in-phase and quadrature (IQ) data collected by one of these radars is used to perform polarimetric spectral decomposition in regions with melting ice.

5.2.1 Attenuation correction in the C-band

C-band radars need attenuation correction in order to use their measurements quantitatively [9]. The attenuation correction algorithms typically assume pure rain conditions. However, especially in convection, large drops and hail can make the C-band radar's signal resonate, producing enhanced scattering and attenuation. In this scenario, the attenuation correction can underestimate the attenuation, and quantitative retrievals can mislead their estimations. This part of the chapter explains the attenuation correction algorithm over rain and piecewise correction algorithm in regions with enhanced scattering.

Differential phase (Φ_{dp}) Method for attenuation correction

This method uses the dual polarization from radars to correct the attenuation. It assumes a linear relationship between the the specific differential phase (K_{dp}) and the attenuation [11]. The slope between K_{dp} and the attenuation can be found by scattering simulations using measured drop size distribution (DSD). This relationship can be expressed in the following way:

$$a = \alpha K_{dp} \tag{5.1}$$

Where a is the attenuation at a particular gate and α is the slope between K_{dp} and the attenuation. Thus, the cumulative attenuation can be expressed as:

$$A = 2 \int_0^r a(s) ds \tag{5.2}$$

Where A is the cumulative attenuation at a range r. The factor 2 in equation (5.2) accounts for the attenuation of the signal back and forth from the radar. Replacing (5.1) in (5.2) yields:

$$A = 2 \int_0^r \alpha K_{dp}(s) ds \tag{5.3}$$

$$A = 2\alpha \int_0^r K_{dp}(s)ds \tag{5.4}$$

Since K_{dp} is the derivative of Φ_{dp}, (5.4) become the following expression:

$$A = 2\alpha[\Phi_{dp}(r) - \Phi_{pd}(0)]. \tag{5.5}$$

Note that since K_{dp} is the derivative of Φ_{dp}, then the integration of the derivative leads into the same function, Φ_{dp}. This expression is very convenient because Φ_{dp} is a radar measurement. Φ_{dp} can experience noise, especially if there is resonance. Therefore, it is recommended to filter Φ_{dp} before applying attenuation correction so that this noise is not propagated to the correction.

Piecewise correction

A variation of the Φ_{dp} method is applied to regions with enhanced attenuation. Enhanced attenuation has been documented in the C-band, especially in tropical climatologies [10]. The piecewise correction increases the attenuation in regions where an enhanced scattering is identified. The rest of the path is treated as rain. The integral in (5.4) is divided into the part with rain and the part with enhanced scattering. An augmented coefficient is used in the part that exhibits an enhanced scattering. The equation that represents this piecewise integration can be expressed as:

$$A = 2\alpha_r \int_0^{r_0} K_{dp}(s)ds + 2\alpha_e \int_{r_0}^{r_1} K_{dp}(s)ds + 2\alpha_r \int_{r_1}^{r} K_{dp}(s)ds \tag{5.6}$$

Where the region with enhanced scattering goes from r_0 to r_1, α_r is the attenuation coefficient used for rain, and α_e is the enhanced attenuation coefficient used to correct the region with enhanced scattering.

5.2.2 Networked-based attenuation correction

The network-based reflectivity is computed using the network of C-band radars deployed during the RELAMPAGO campaign. This algorithm uses the simultaneous observation from a net-

work of radars and computes a reflectivity that matches in an optimal way all the radars. This network-based approach was developed for the network of X-band radars as part of the CASA project [54]. The network-based attenuation algorithm was adapted to the C-band for our study.

The network-based attenuation correction algorithm reconciles the reflectivity from a primary radar with the observations from the other radars in the networks. This algorithm is based on the assumption that the radars in the network should measure the same reflectivity because they are in the same band and should have similar scattering responses. The algorithm iterates over the following equations to estimate an optimal reflectivity that matches all the radars:

$$Z(r) = Z_m(r) + 2\int_{r_0}^{r} a(s)ds \tag{5.7}$$

$$a(r) = cZ^b(r) \tag{5.8}$$

Where Z and Z_m are the intrinsic and the measured reflectivities in dB, and c and b are the constants that relate the attenuation to the intrinsic reflectivity.

(5.7) relates the intrinsic reflectivity, the measured reflectivity, and the attenuation. As can be seen in this equation, the intrinsic reflectivity is the measured reflectivity plus the attenuation. At the same time, the intrinsic reflectivity and the attenuation are given in (5.8). An optimal intrinsic reflectivity is found by iterating over these two equations and the radars' measurements in the network.

The network-based algorithm matches the reflectivity over a common volume of observations from the radar network. Therefore, the algorithm needs sufficient overlapping regions between the primary radar and the other radars' measurements in the network. In addition, this algorithm is ray based. The rays of the primary radar are compared with the other radar measurements and then reconciled optimally.

Bias between the radar needs to be taken into account. [55] Computed the bias for the network of radars deployed during the RELAMPAGO campaign and cross-compared this bias with GPM.

The bias between the radars was considered at the time of running the network-based attenuation algorithm in this study.

5.2.3 Doppler winds

The python dual Doppler Analysis (PyDDA) package is used to compute the 3D Doppler winds [56]. This package uses the 3D variational method based on [22] with vorticity constraints [57]. Radial velocity data from the network of C-band radars deployed during RELAMPAGO are used to construct the Doppler winds.

The wind field has three degrees of freedom; each radar provides one radial velocity to resolve the 3D wind field. If two radars are used, there is still one free variable to resolve the 3D velocity field. The third variable is constrained using the conservation of mass as a boundary condition.

It is important to mention that the wind field cannot be retrieved when the angle between both radars is less than 30°. This is because the degree of independence between the radial velocity needs to be high to reconstruct the wind field. Otherwise, the two radial velocities would be a linear combination of each other and would not provide independent measurements to resolve the wind field.

5.3 Data

The radar observations used in this study are explained in this section. The simultaneous dual observations from the network of C-band radars deployed during the RELAMPAGO campaign are used to study the attenuation of melting ice.

5.3.1 The RELAMPAGO C-band radars

The network of C-band radar deployed during the RELAMPAGO campaign is used to study the attenuation in melting ice. The RELAMPAGO campaign took place near the Sierras de Cordoba in Argentina, a region known for having some of the tallest storms on earth [58]. The campaign's

intensive operational period went from November 1st to December 18th, 2018. RELAMPAGO also had an extended operational period until January 31st, 2018.

Table 5.1: Location of the RELAMPAGO C-band radars used in this study. The elevation is above mean sea level (MSL)

Radar	Latitude	Longitude	Elevation MSL (M)
CSU-CHIVO	31.63S	64.17W	421
CSAPR-2	32.13S	64.73W	1141

During the RELAMPAGO campaign, Colorado State University (CSU) deployed the C-band Hydrological Instrument for Volumetric Observation (CSU-CHIVO) radar. CSU-CHIVO was deployed South of Cordoba city, as shown in Fig. 5.1. CSU-CHIVO collected dual polarimetric radar data from November 10th, 2018, to January 31st, 2019. The coordinates and altitude of the CSU-CHIVO can be seen in Table 5.1. A picture of the CSU-CHIVO deployed in South Cordoba city can be seen in Fig. 5.2(a).

Figure 5.1: Map with the location of the C-band radars used in this study.

The C-band Scanning ARM Precipitation Radar 2 (CSAPR-2) was deployed in Argentina as part of the Clouds, Aerosols, and Complex Terrain Interactions (CACTI) field campaign. CACTI

took place in Argentina simultaneously with RELAMPAGO. CSAPR-2 was collecting data during the intensive and the extended RELAMPAGO observational period. CSAPR-2 was located near the foothills of the Sierras de Cordoba, as can be seen in Fig. 5.1. CSAPR-2 is a radar from the US Department of Energy (DOE) and is part of the Atmospheric Research Measurement (ARM) facility. CSAPR-2 is a C-band radar with dual-polarization capability. CSAPR-2 and the CSU-CHIVO radar are 76.1 km apart from each other. The location of CSAPR-2 and its altitude can be seen in Table 5.1. A picture of the CSAPR-2 radar deployed in the Villa Yacanto site is shown in Fig. 5.2(b).

Figure 5.2: Picture of the C-band radars used in this study deployed in Argentina. (a) is CSU-CHIVO radar deployed South Cordoba City, (b) is CSAPR-2 deployed near the Sierras de Cordoba.

The bias between the radars is considered when performing the networked attenuation correction. [55] reported the bias in the reflectivity of the C-band radars deployed during the RELAMPAGO campaign. In this study, the authors use the Ku band radar on board the GPM core observatory as a common reference for each of the RELAMPAGO radars. They also compare the bias between each of the radars to one another. They found a consistent bias between the network of radar.

The CSU-CHIVO and the CHIVO will be used interchangeably to denote the same radar in the rest of the chapter. In a similar way, the CSAPR-2 and CSAPR radar mean the same radar and will be used interchangeably for simplicity.

5.3.2 The December 14, 2018, study case

The December 14, 2018, case is used to study the attenuation of melting ice. During this case, convective systems initiate in between the location of CHIVO and CSAPR, providing enough overlapping to compute dual radar retrievals such as network-based attenuation and Doppler winds. Significant hail and severe weather were also reported on the ground in this case [1]. A picture of one of the hailstones that was reported during this day is shown in Fig. 5.3.

Figure 5.3: Hailstone reported by the community on December 14, 2018, near Cordoba city [1].

The convective cells that initiate at 2 UTC between CHIVO and CSAPR evolve very fast [59]. As a result, the simultaneous observations between CHIVO and CSAPR scans need to be closely synchronized in time to compute dual radar retrievals. CHIVO collected data in a 10 min interval

during the campaign, while CSAPR has a scan strategy interval of 15 min. As a result, CHIVO and CSAPR synchronized every 30 min. CHIVO and CSAPR synchronized at 2:00 and 2:30 UTC for this study case, providing dual radar observations to study the melting ice at this time.

Fig. 5.4 shows CHIVO and CSAPR differential reflectivity at 2 UTC for the December 14, 2018, case for a low elevation plan position indicator (PPI) scan. It can be seen in this figure that the differential reflectivity reaches values of more than 6 dB in the region marked by the black square. Downrange of this region, the Z_{dr} drops to negative values for both radars. Note the CSAPR's PPI is centered at the CHIVO origin to show the coinciding location of the spike in the Z_{dr} for each of the radars. It is worth noting that the reflectivity and differential reflectivity were corrected for attenuation according to [55].

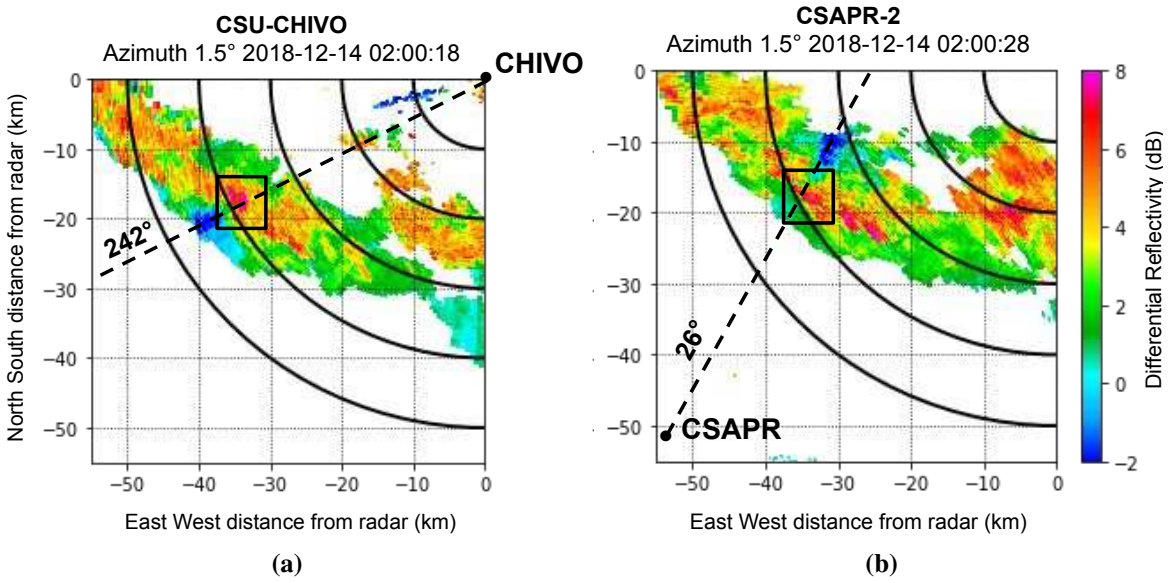

Figure 5.4: Differential reflectivity from CSU-CHIVO (a) and CSAPR-2 (b). CSAPR's plot is centered at CHIVO coordinates. The black square shows the region with a spike in Z_{dr}. The dotted line in the CHIVO and CSAPR plots refers to the azimuth 242° and 26°, respectively.

A spike in the differential reflectivity followed by negative values can indicate an enhanced attenuation [10], especially at low-elevation scans. Positive Z_{dr} is expected to be observed in the low-elevation scans instead of negative Z_{dr}. The Z_{dr} values are negative when particles are oriented vertically, such as ice crystals. Typically, these ice particles should have already melted

away at low elevations. As a result, the negative Z_{dr} observed in Fig. 5.4 indicates an enhanced attenuation that the correction algorithms do not compensate for satisfactorily due to a possible enhanced scattering produced by melting ice.

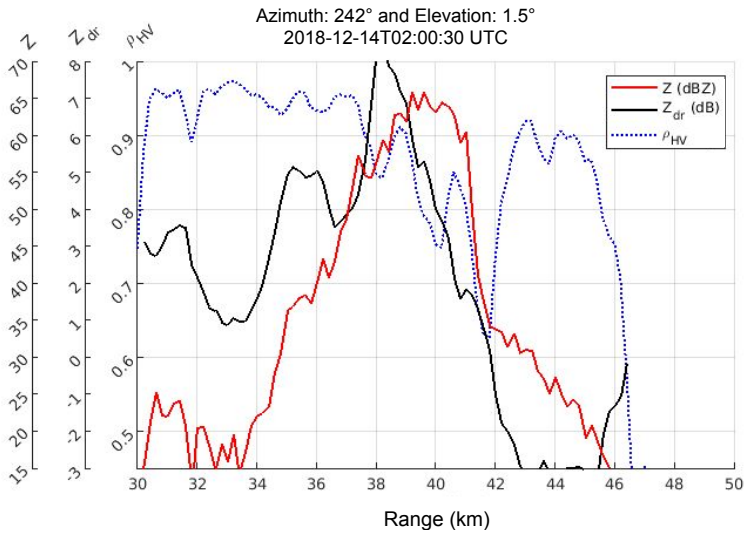

Figure 5.5: Reflectivity, differential reflectivity, and copolar correction along azimuth 242° shown in Fig. 5.4 in dashed line.

The dual polarimetric variables from CHIVO radar along the 242° azimuth are shown in Fig. 5.5. This azimuth crosses the region with the spike in Z_{dr}, and it is marked by the dashed line in Fig. 5.4. It can be seen in Fig. 5.5 that Z_{dr} reaches values higher than 8 dB near the 38 km range, and the Z_{dr} values drop to negative after the 42 km range. It can also be seen in Fig. 5.5 that the values in the copolar correlation decrease to almost 0.7 near the 38 km range, and the reflectivity displays high values greater than 60 dBZ.

The polarimetric measurements in Fig. 5.5 suggest melting ice between the 38 km and 42 km range. Simulations made by [53] show that melting ice exhibits a spike in the Z_{dr} and an enhanced attenuation, like the values observed in Figs. 5.4 and 5.5. In addition, the high values in the reflectivity could be an indication of the presence of hail in some form. Furthermore, the decrease in the copolar correlation in this region supports the presence of a mixed phase of rain and ice.

As can be seen from the analysis of Figs. 5.4 and 5.5, this case displays polarimetric signatures of melting ice. This case also provides dual radar observations from CHIVO and CSAPR. Therefore, this data is used to study the melting ice attenuation. Vertical analysis, Doppler wind, spectral decomposition, and network-based attenuation analysis are performed also to this case to understand more the microphysics involved in melting ice evolution and its attenuation.

5.4 Results

The attenuation of melting ice in the C-band is studied using the simultaneous observations from the CSU-CHIVO and the CSAPR radars collected during the RELAMPAGO campaign. The radar measurements on December 14, 2018, that display polarimetric signatures of melting ice are used. As was shown in the previous section, the correction algorithms seem not to compensate for the attenuation satisfactorily due to the melting ice in the December 14 case. A radar network-based procedure is also presented in this section. This procedure is employed to estimate the true values of the reflectivity and differential reflectivity. Subsequently, these network-based retrievals are used to study the attenuation in melting ice.

The simultaneous observations from CHIVO and CSAPR are used to identify the melting ice and estimate its attenuation. We first explore one azimuth to explain the rationale behind identifying melting ice and estimating its attenuation in A and B. This same rationale is applied to many other azimuths that display melting ice signatures in C. Also in C, the network-based attenuation is compared with the attenuation from disdrometer observations to validate the estimation method used for the melting ice.

5.4.1 Identifying Melting Ice

A series of radar polarimetric analyses were conducted to identify melting ice in the radar data collected on December 14, 2018. These analyses include 1) the vertical analysis of dual polarimetric measurements from a range position indicator (RHI) scan, 2) hydrometeor classification inferred from dual-pol observations, and 3) spectral polarimetric decomposition from IQ data. In

addition, 4) dual Doppler analysis from CHIVO and CSAPR is also obtained to understand the storm motion and how the melting ice evolves.

Vertical Structure of the Storm

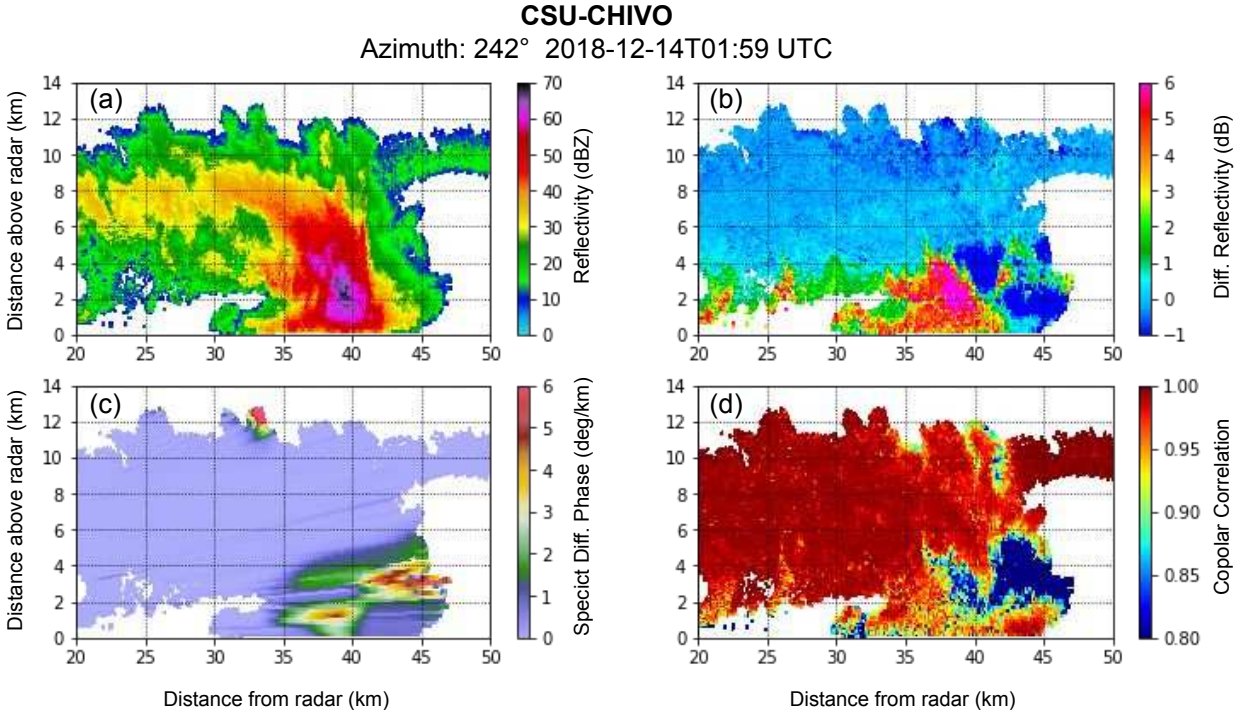

Figure 5.6: Vertical reflectivity (a), differential reflectivity (b), specific differential phase (c), and copolar correction (d) form an RHI that intersects the melting ice region.

CSU-CHIVO took an RHI in the direction where the signatures of melting ice were observed. This RHI is presented in Fig. 5.6. This RHI shows the vertical Z, Z_{dr}, K_{dp}, and ρ_{hv} along the 242°azimuth. This vertical cross-section of the storm was taken a minute before the simultaneous observation from CHIVO and CSAPR at 2:00 UTC. This RHI allows the analysis of the storm's vertical structure near the melting ice region.

The RHI in Fig. 5.6 displays complex characteristics in the vertical where the melting ice region is suspected, near 38 km. It can be seen in this figure that the storm displays enhanced values of Z_{dr} between 35 and 40 km. These enhanced values of Z_{dr} propagate in the vertical, forming a Z_{dr} column that reaches almost 5 km in height. This Z_{dr} column indicates a wide

updraft [47]. It can also be seen from the Z_{dr} plot that there seem to be two inflows going into this updraft (left part of the Z_{dr} column). One of the inflows seems to come from the low levels near the ground below 2 km in height. The other inflow appears to come from the mid-levels above the 2 km. Both inflows converge at the location of the Z_{dr} column. This region also displays high values of reflectivity, which could be an indication of hail. High values of K_{dp} are also observed in this region of convergence. The high values in K_{dp} indicate the abundance of liquid water in this region. Additionally, the copolar correlation decreases in this region. This drop in copolar correlation could be caused by a mixed phase of rain and melting ice.

Hydrometeor Classification

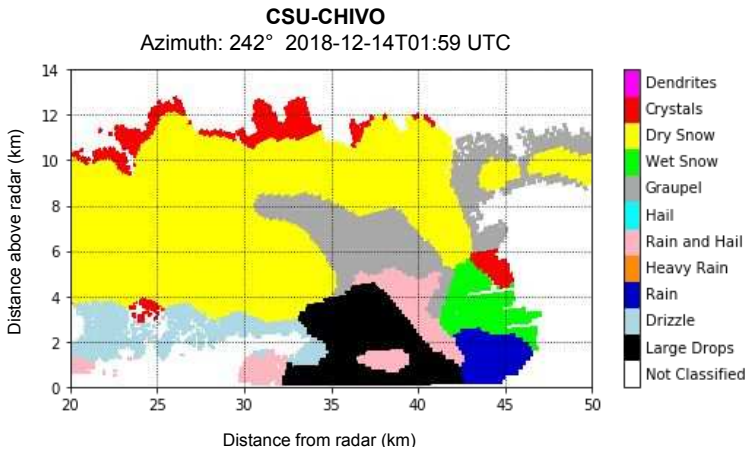

Figure 5.7: Hydrometeor classification inferred from the dual polarimetric measurement presented in Fig.5.6.

The type of precipitation particles in the RHI presented in Fig. 5.6 is inferred from its dual polarimetric measurements. The semi-supervised hydrometeor classification algorithm (Hydro-Class) [60] is used to infer the type of particles from the dual-pol measurements in the RHI of Fig 5.6. This algorithm uses fuzzy logic with region clustering. The algorithm resolved 11 classes of weather particles. These classes include hail and a mix of rain and hail. Fig. 5.7 shows the hydrometeor classification resolved from the measurements in the RHI of Fig. 5.6.

HydroClass resolves a mix of rain and hail near the region with signatures of melting ice. The mix of rain and hail is shown in magenta in Fig 5.7. This mix of phases is resolved near 38 km in the low elevations, near the melting ice signatures observed in Figs. 5.4, and 5.5. This mix of rain and hail at the low elevation suggests that in fact, ice might be melting due to the warmer temperatures near the ground.

Doppler Winds

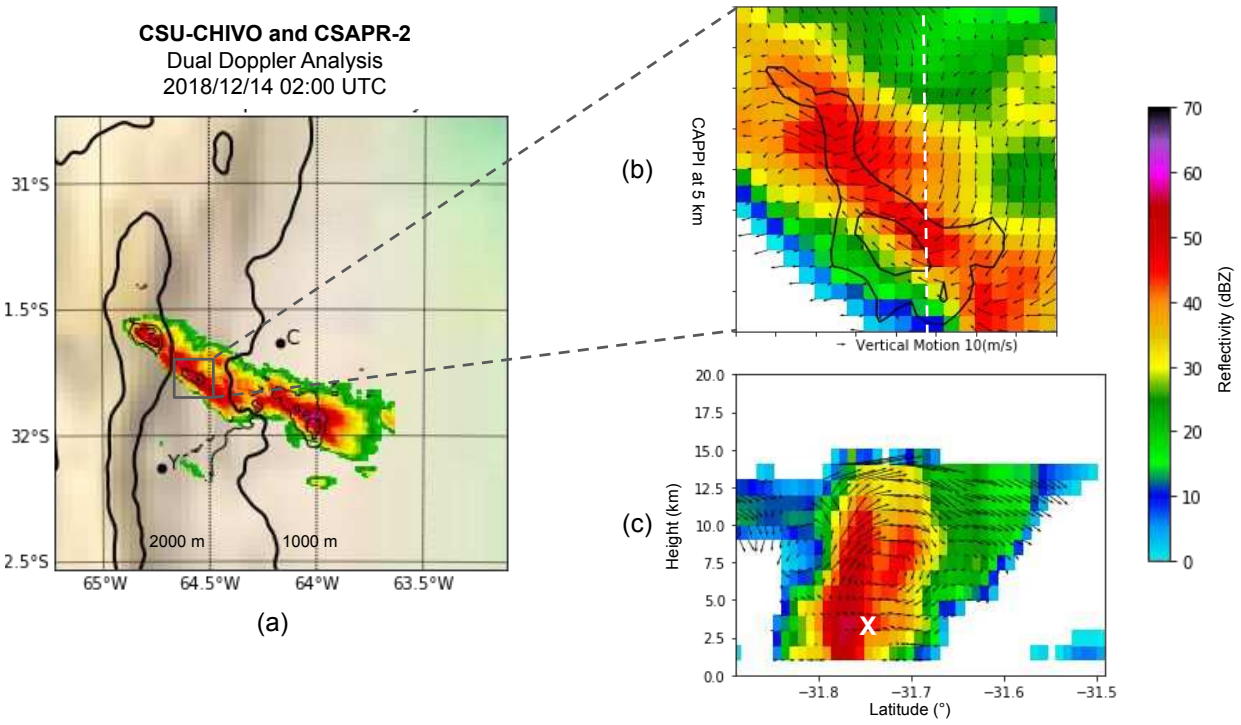

Figure 5.8: Dual Doppler analysis from CSU-CHIVO and CSAPR-2 at 2:00 UTC, December 14, 2018. (a) shows the maximum composite reflectivity over the column and updraft contours starting at 20 m/s. (b) shows a Constant Altitude PPI (CAPPI) over the region marked by a square in (a). The contours this time are updrafts starting at 10 m/s. (c) shows a vertical cross-section marked by the dashed line in (b).

The Doppler winds are computed to have an insight into the interaction between the microphysics and the kinematics of this storm. The RHI in Fig. 5.6 suggests the presence of two inflows in the storm. This RHI also displays a Z_{dr} column in the region of convergence of these two inflows. This Z_{dr} column indicates a vigorous and wide updraft in this region of convergence. It is in this region of convergence where the polarimetric signatures of melting ice are observed. The

storm motion retrieved from Doppler winds can help to elucidate the coexistence of ice and rain in the low elevation.

The 3D velocity field is retrieved from the simultaneous observation from CHIVO and CSAPR. These simultaneous observations were taken at 2 UTC on December 14, 2018. The PyDDA package [56] was used to obtain the Doppler winds. This algorithm retrieved the 3D winds using a variational method [57] to resolve the vertical vorticity equation [22]. Once the 3D velocity field is computed, the storm motion is subtracted to obtain the storm relative motion.

Fig. 5.8(a) shows the maximum reflectivity over the column in solid. The contours mean 20 m/s maximum updrafts over the column. It can be seen in this figure that the storm displays multiple updrafts. Some updrafts are wide, like the one marked in the square in Fig. 5.8(a). Fig. 5.8(b) shows a CAPPI at 5 km with the arrows signifying the direction and magnitude of the winds. This time the contours mean upward vertical velocity starting at 10 m/s. It can be seen from Fig. 5.8(b) that the storm displays a wide updraft at this part. It can also be seen in this figure that the storm displays some vorticity.

The dashed line in Fig. 5.8(b) indicates the vertical cross-section shown in Fig. 5.8(c). The arrows in Fig. 5.8(c) indicate the North South and the vertical wind components. It can be seen in Fig. 5.8(c) a recirculation pattern. The X in Fig. 5.8(c) marks the location where the mix phase was observed. It can be seen in the region marked by an X, the convergence of two streams. As the RHI in Fig 5.6 suggests, one of the inflows is coming from the upper levels, and the other inflow is coming from the low levels. These two inflows converge in the mid-levels forming a circulation pattern in the vertical.

5.4.2 Estimating the Attenuation in Melting Ice Regions

This part of the chapter explains how the simultaneous observations from CHIVO and CSAPR are used to estimate the horizontal and differential attenuation in melting ice regions. The analysis presented in the last section provides confidence in the identification of melting ice regions from radar observations. The negative Z_{dr} observed downrange of the melting ice suggests an enhanced

attenuation that a single radar correction scheme does not compensate satisfactorily for. Nevertheless, using the simultaneous observations from CHIVO and CSAPR allows us to obtain a better estimate of the reflectivity and differential reflectivity in melting ice regions.

Horizontal Attenuation

The reflectivity in the region of melting ice is estimated using the network-based scheme developed by [54]. This algorithm reconciles the reflectivity from radars that observe storms from different locations and obtains a reflectivity that matches the best the radars' reflectivity in a common observation area. In this case, when the melting ice was observed, the network-based algorithm reconciled the reflectivity from CHIVO and CSAPR, both C-band radars. Since the melting ice region marked in Fig. 5.4 is in between both radars, CHIVO and CSAPR provide observations from different ends of the storms, which makes the network-based method suitable for studying the attenuation in the melting ice region.

Network-based Reflectivity

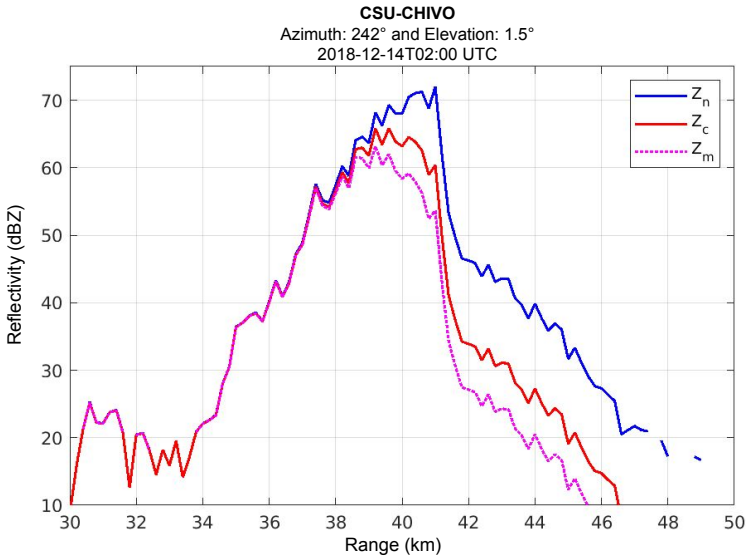

Figure 5.9: CHIVO Network-based (Z_n), corrected (Z_c), and measured (Z_m) reflectivity along the 242° azimuth.

The reflectivity using the network-based approach is obtained for the radar data that displays polarimetric signatures of melting. The azimuth marked in Fig. 5.4(a) is used as an example to explain how the network-based approach is employed. Fig. 5.9 shows in blue the network-based reflectivity (Z_n), computed using simultaneous observation from CHIVO and CSAPR. The reflectivity corrected using the dual polarization from only CHIVO radar (Z_c) is shown in red, whereas the measured reflectivity (Z_m) from CHIVO radar is shown in magenta. These reflectivity profiles are displayed along the 242° azimuth near 2 UTC. This azimuth crosses the region with melting ice, as can be seen in Fig. 5.4. Dual polarimetric measurements of this azimuth are shown in Fig. 5.5.

It can be seen in Fig. 5.9 that the reflectivity obtained using dual radar observations is higher than the reflectivity corrected using only the CHIVO measurements in the melting ice region. It can also be seen that Zn reaches a maximum of more than 70 dBZ at 41 km. On the other hand, Z_c reaches its maximum at 39 km, which is about 65 dBZ. Z_n continues increasing after 40 km in range while Z_c starts decreasing at this range.

The Z_n is considered to provide a better estimate of the reflectivity in the melting ice region. The network-based algorithm matches the CHIVO reflectivity downrange of the melting ice region with the CSAPR reflectivity. From CSAPR, the reflectivity has not been affected by the melting ice at this range. The reason is that the CSAPR signal has not yet crossed the melting ice region.

The difference between Z_n and Z_c increases when the polarimetric measurements show signatures of melting ice. In addition, this difference seems to stabilize when no more melting ice signatures are observed from the polarimetric measurements. Fig. 5.10 shows the difference between Z_n and Z_m in blue. The difference between Z_n and Z_c is shown in red, whereas the difference between Z_c and Z_m is shown in orange. As can be seen in this figure, the difference between Z_n and Z_c starts to deviate at around 37 km in range. From the dual polarimetric measurement shown in Fig. 5.5, it can be seen that the Z_{dr} slope increases significantly at this range until it reaches 8 dB at 38 km. It can also be seen that ρ_{hv} starts decreasing in this mix-phase region. The difference between Z_n and Z_c constantly increases until it stabilizes at around 42 km in range. Z_{dr} also seems

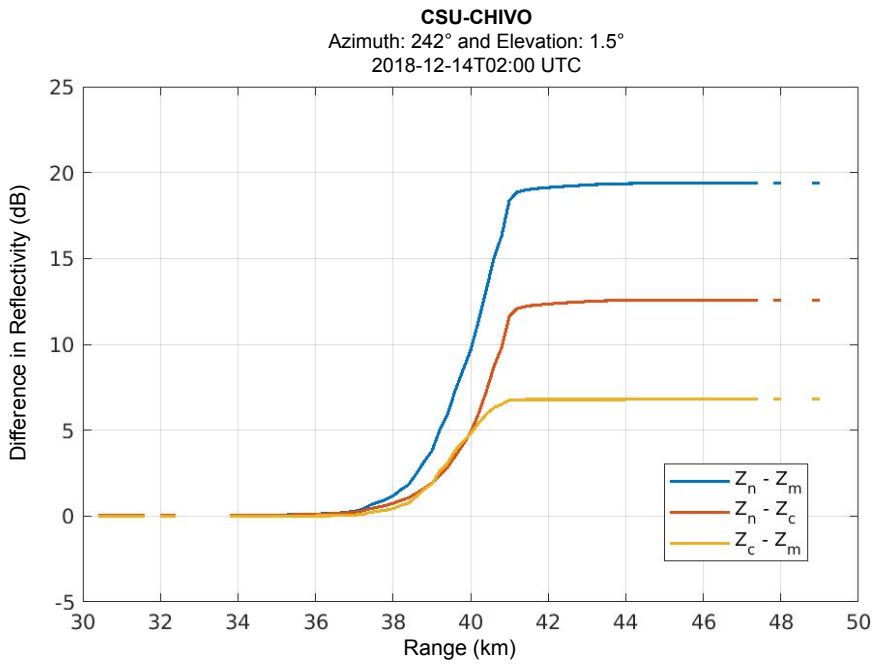

Figure 5.10: Difference in the reflectivities shown in Fig. 5.9. In blue, it is shown the difference between Z_n and Z_m. In red is shown the difference between Zn and Z_c, and in orange is shown the difference between Z_c and Z_m.

to stabilize at 42 km. There is a difference of almost 12 dB between Z_n and Z_c after crossing the region with melting ice.

Piecewise Correction

An enhancement in the attenuation correction coefficient is applied to the region that displays melting ice signatures. This coefficient is chosen such that the corrected reflectivity using the enhanced coefficient (Z_e) matches the network-based reflectivity at the end of the melting ice region. The region with melting ice is identified using Z_{dr}, ρ_{hv}, and the difference between Z_n and Z_c (ΔZ). Fig. 5.11 shows Z_{dr}, ρ_{hv}, and ΔZ along the 242° azimuth.

The starting point of the piecewise correction is selected to be the 37 km in range. It can be seen in Fig. 5.11 that the Z_{dr} slope increases significantly from 37. This increase in Z_{dr} can be an indication of the presence of melting ice. In this same range, ρ_{hv} starts decreasing significantly, which could be an indication of a diversity of hydrometeor species from 37 km in range. Note that

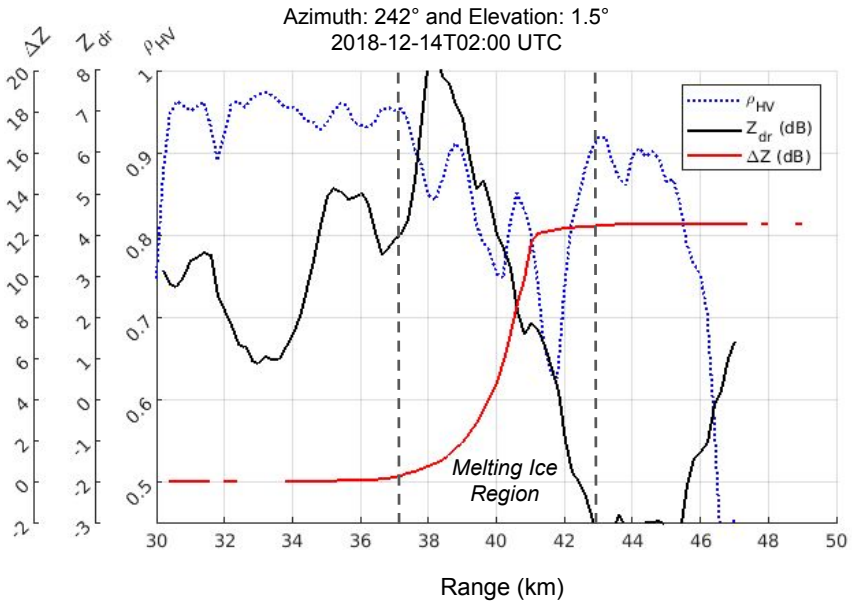

Figure 5.11: Differential reflectivity (black), copolar correlation (blue), and the difference between the network-based reflectivity and the corrected reflectivity from CHIVO radar (red).

ΔZ starts deviating significantly from this range. Therefore, this range is used as the starting point for the piecewise correction.

The endpoint in range for the piecewise correction is chosen using the same variables that were used to mark the start point, i.e., Z_{dr}, ρ_{hv}, and ΔZ. In Fig 5.11, it can be seen that Z_{dr} stabilizes near the 43 km in range. This stabilization could be attributed to the presence of only rain without melting ice affecting the differential channel. Similarly, ρ_{hv} increases at this same range, which could indicate the presence of only one kind of particle in the volume. Also note that at this point, ΔZ is also stable. As a result, the 43 km is used as a cutting point for enhanced attenuation correction.

An enhancement in the attenuation correction coefficients is applied from the start to the end point in the piecewise correction. This portion of the radar bin goes from 37 km to 42 km along the 242° azimuth, as shown in Fig. 5.11. An enhancement in the horizontal correction coefficient is applied to this region to compute the attenuation that matches the network-based reflectivity. The network-based algorithm matches the reflectivity from CHIVO and CSAPR in an optimal way. As

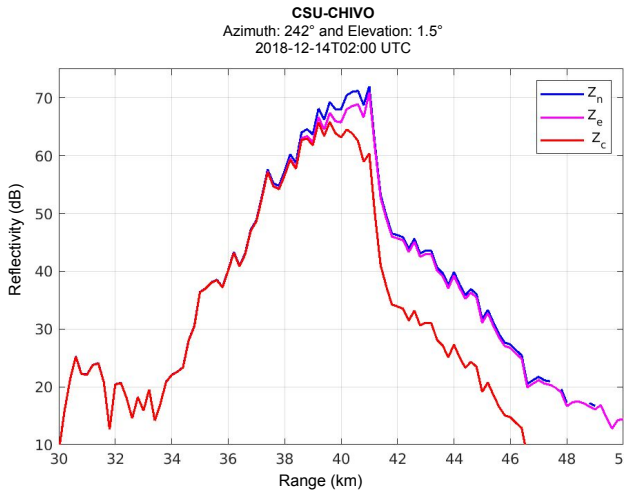

Figure 5.12: Network-based (Z_{n}), enhanced coefficients (Z_{e}), and corrected reflectivity (Z_{c}).

a result, this enhancement in the attenuation correction coefficients to match Z_n can be seen as matching CHIVO reflectivity to the CSAPR observation after crossing the region with melting ice.

The reflectivity using enhanced coefficients is computed. Fig. 5.12 shows in blue Z_n, in magenta Z_e, and in red Z_c. The enhanced attenuation correction coefficient that makes Z_e match Z_n was 0.48 for this azimuth. The coefficient that was used to correct the reflectivity with no enhancement is 0.15. This coefficient was computed from disdrometer data collected locally during the RELAMPAGO campaign in [55].

Z_e follows Z_n closely after the melting ice region, as can be seen in Fig. 5.12. There seems to be a difference between Z_n and Z_e at the beginning of the melting ice region. However, Z_e progressively catches this difference later along the range. This difference between Z_n and Z_e at the beginning of the melting ice region suggests a variation of the coefficients in the region of melting ice. This difference could be explained by changes in the melting ice concentration, size distribution, and beam filling. This enhanced coefficient is a bulk estimate that represents the average attenuation along the melting ice region. However, it could be that the coefficients vary along the melting ice region. More about this variation is discussed in section V.

Differential Attenuation

The simultaneous observations from CHIVO and CSAPR are used to estimate the differential reflectivity in the melting ice region. The location of the radars and the storm in between allow one of the radars to observe the differential reflectivity with almost no attenuation for each end of the storm. As a result, one can know the differential reflectivity after crossing the melting ice region using the measurements from the other radar.

Correction of Z_{dr} from Simultaneous Radar Observations

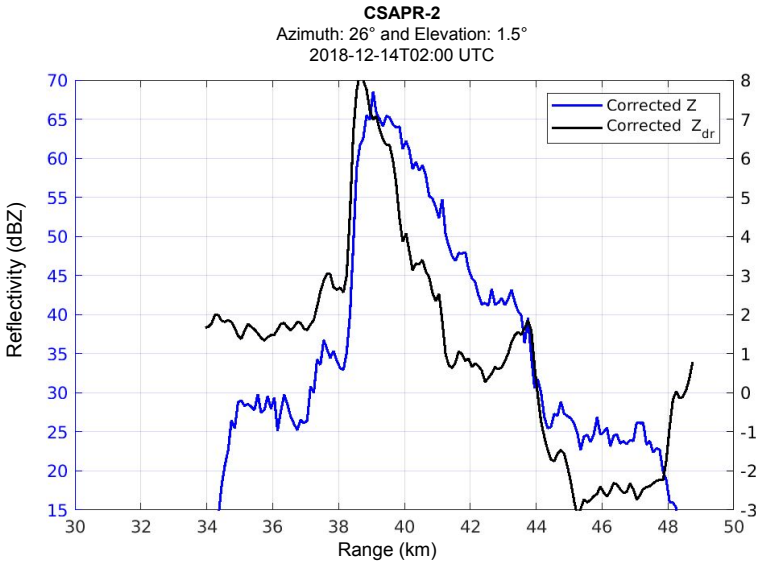

Figure 5.13: Reflectivity (blue) and differential reflectivity (black) from CSAPR radar. The CSAPR Z_{dr} is near 2 dB before entering the melting ice region.

The Z_{dr} from one of the radars after crossing the melting ice region is set to be the average of the Z_{dr} from the other radar at the other end of the storm. The attenuation coefficient for the differential channel is enhanced in the melting ice region to match the Z_{dr} from the other radar. For instance, it can be seen in Fig. 5.4 a negative Z_{dr} from the CHIVO radar after crossing the melting ice region. However, from a CSAPR perspective, this Z_{dr} is positive. Therefore, the negative Z_{dr} from CHIVO is replaced by an average of the CSAPR reflectivity in this negative Z_{dr} region observed by CHIVO. Subsequently, the Z_{dr} correction coefficient is computed to match the

positive Z_{dr} observed by CSARP. In this example, note that CSAPR Z_{dr} has not yet crossed the melting ice region. As a result, the CSAPR Z_{dr} is a better estimate than the negative Z_{dr} from the CHIVO radar.

From CSAPR, it can be seen the Z_{dr} is near 2 dB downrange of the melting ice from CHIVO. Fig. 5.13 shows the reflectivity in blue and differential reflectivity in black from a bin of CSAPR that crosses the melting ice region. This azimuth is marked by the dashed line in Fig. 5.4(b). Note that CSAPR differential reflectivity is near 2 dB before entering the melting ice region. At the same time, it can be seen from Fig. 5.11 that the differential reflectivity from CHIVO after crossing the melting ice region is near -2 dB. Thus, there is a 4 dB difference between the Z_{dr} from CHIVO and CSAPR at this part of the storm. The attenuation correction coefficient is enhanced to compensate for this 4 dB in order to bring the CHIVO Z_{dr} to the 2 dB measured by CSAPR.

Piecewise Correction of Z_{dr}

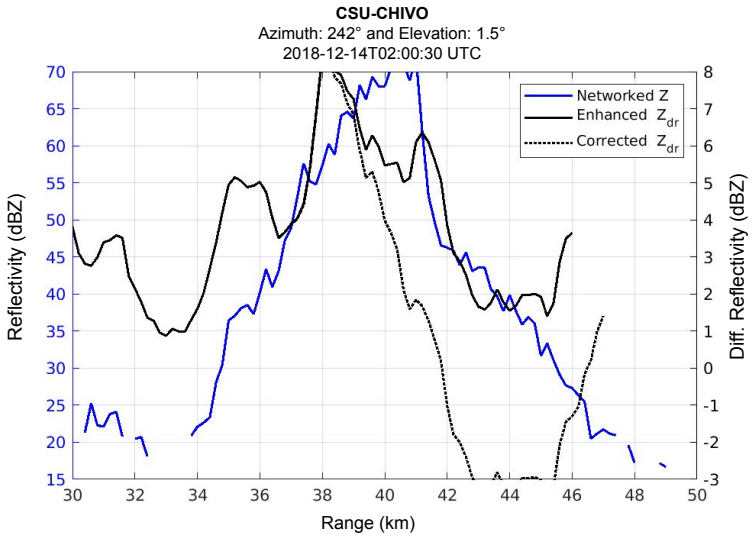

Figure 5.14: CHIVO reflectivity (blue), differential reflectivity using enhanced coefficients (solid black), and the corrected differential reflectivity using nonenhanced attenuation correction coefficient (doted black).

An Enhancement in the differential correction coefficients is applied in the region that exhibits melting ice to match the differential reflectivity from the other radar. The region where the en-

hanced differential coefficient is applied is the same as the region where the piecewise correction was chosen for the horizontal piecewise correction. For the 242° azimuth, this region goes from 37 km to 43 km in range. Fig. 5.14 shows in solid black the Z_{dr} after the enhanced coefficients are applied. This figure also shows the corrected differential reflectivity using a single radar approach in the black dashed line. For a single radar, the differential correction coefficient applied was 0.036. The enhanced coefficient that makes CHIVO Z_{dr} match CSAPR Z_{dr} after crossing the melting ice region is 0.1632. It can be seen from Fig. 5.14 that after the enhanced correction, Z_{dr} matches the 2 dB observed from CSAPR in the region of the storm downrange of the melting ice from CHIVO.

5.4.3 Network-based Attenuation Correction Coefficients

Attenuation correction coefficients for melting ice and rain were obtained empirically using the network-based approach explained in the last section. Simultaneous observations from CHIVO and CSAPR on December 14, 2018, at 2:00 and 2:30 UTC were used. The attenuation correction coefficients were computed using the network-based approach for radar bins that display polarimetric signatures of melting ice. In addition, the attenuation coefficients were also computed for regions that display polarimetric signatures of only rain. Finally, the empirical coefficients obtained for rain are compared to disdrometer measurements to validate the network-based procedure to compute the attenuation correction coefficients.

Melting Ice Attenuation Coefficients from a Network-based Scheme

Attenuation correction coefficients are computed for the radar data that displays polarimetric signatures of melting ice. Data from CHIVO and CSAPR are employed. Both radars are set as primary radars in the network-based correction, i.e., one is used to correct the reflectivity of the other radar and vice versa. The piecewise approach studied in the previous section is employed to estimate the attenuation correction coefficients. These coefficients are chosen such that the corrected measurements match the network-based measurements at the end of the storm.

Simultaneous observations from CHIVO and CSAPR at 2:00 and 2:30 UTC on December 14, 2018, are used to estimate the attenuation correction coefficients in melting ice. CHIVO and CSAPR data display polarimetric signatures of melting at these two times during the December 14 case. Simultaneous observations from both radars of high Z_{dr} followed by negative values are used to identify melting ice regions. A decrease in ρ_{hv} is also used to confirm a mix of phases between melting ice and rain.

Table 5.2: Melting ice attenuation correction coefficients where $\alpha = a_h/K_{dp}$, and $\beta = a_{hv}/K_{dp}$. a_h and a_{hv} are the horizontal and differential attenuation respectively

Time	**Radar**	**Azi.** (°)	**Ele.** (°)	α	β
2:00 UTC	CHIVO	242	1.5	0.48	0.168
2:00 UTC	CHIVO	244	1.5	0.73	0.146
2:00 UTC	CSAPR	26	1.5	0.40	0.160
2:30 UTC	CHIVO	196	1.5	0.40	0.100
2:30 UTC	CSAPR	60	1.5	0.50	0.115
2:30 UTC	CSAPR	62	1.5	0.45	0.090

Table 5.2 shows the attenuation coefficients computed at 2 UTC and 2:30 UTC from both radars. It was challenging to find data that displays polarimetric signatures of melting ice. Therefore, we use data from both radars at 2:00 and 2:30 UTC to obtain as much azimuth as possible with melting ice. We allow a degree between the azimuths to obtain independent measurements since the IQ samples might overlap between consecutive degrees.

Some of the statistics of the melting ice coefficients are computed from Table 5.2. The average of the horizontal coefficients is 0.49, and the differential coefficient average is 0.13. The standard deviation for the horizontal coefficient is 0.12, while the differential attenuation standard deviation is 0.03. Most of the horizontal coefficients are within one standard deviation, except the one at 2 UTC and azimuth 244°, which is two standard deviations from the mean. Similarly, the empirical coefficients for the differential attenuation are within a standard deviation without outliers.

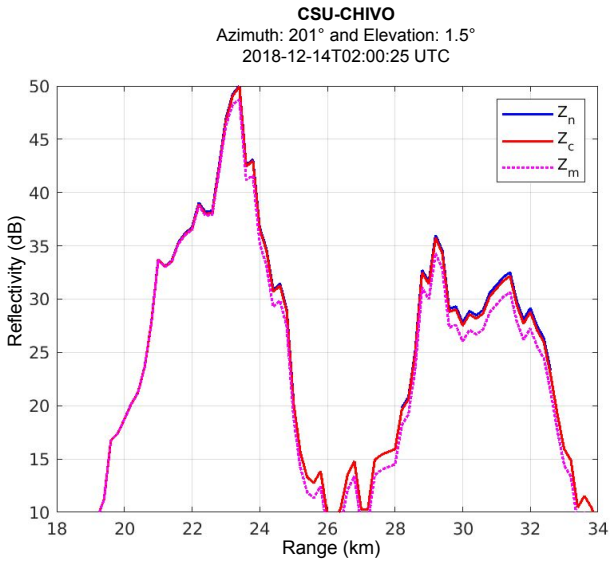

Figure 5.15: CHIVO reflectivity along the 201°azimuth. In blue is shown the network-based reflectivity, in red the corrected reflectivity using a single radar, and in magenta the measured reflectivity.

Validation of the network-based scheme to compute attenuation correction coefficients

The network-based scheme to compute the attenuation coefficient is validated by comparing these coefficients to disdrometer coefficients under rain conditions. The attenuation correction coefficients are computed using the network-based approach for radar data that display polarimetric signatures of rain. The attenuation coefficients for rain are computed exactly as they were computed for melting ice, i.e., the horizontal and differential coefficients are chosen to match the network-based estimation after attenuation correction.

The network-based reflectivity matches the corrected reflectivity well under rain conditions. One example of radar data that displays polarimetric signatures of rain is shown in Fig. 5.15. This figure shows in blue the network-based reflectivity that was constructed using the simultaneous observation from CHIVO and CSAPR. The corrected reflectivity using 0.15 as correction coefficients is shown in red. This coefficient was computed from local disdrometers deployed during the campaign [55]. The measured reflectivity is shown in magenta. There is also can be seen that the measured reflectivity is lower, which means that attenuation correction is needed to compensate for attenuation in rain conditions.

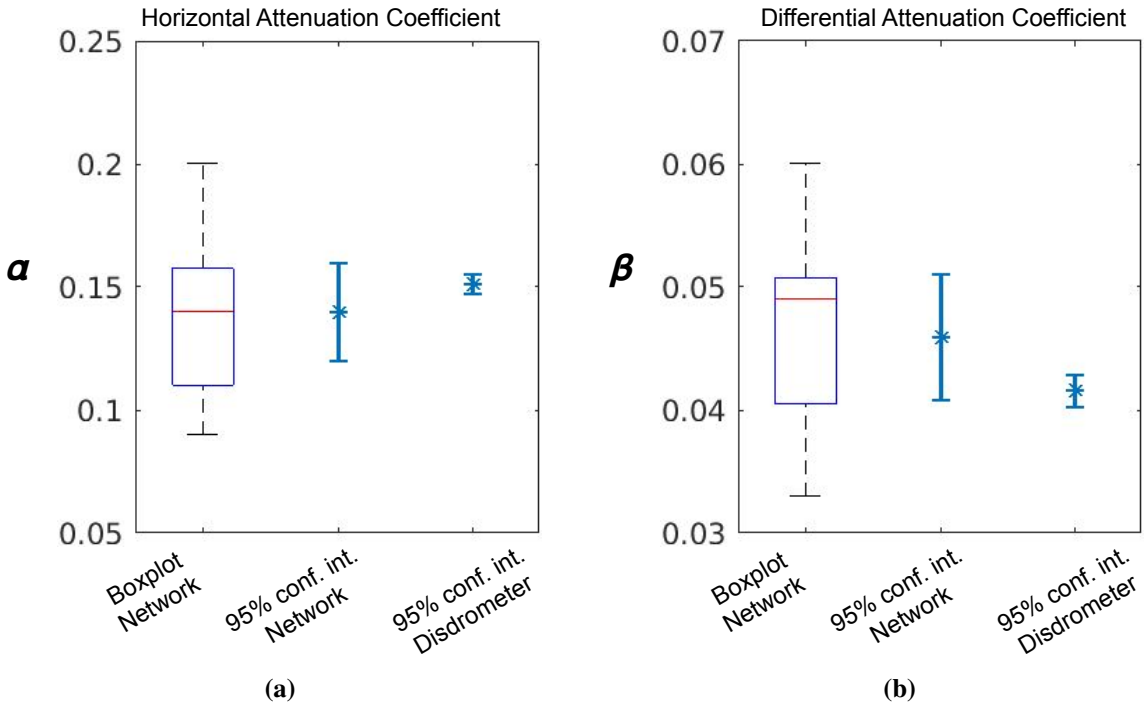

Figure 5.16: Attenuation correction coefficient for rain in the C-band. (a) shows the horizontal attenuation correction coefficient where $\alpha = a_h/K_{dp}$, and a_h is the horizontal attenuation. (b) shows the differential attenuation correction coefficient where $\beta = a_{hv}/K_{dp}$, and a_{hv} is the differential attenuation. To the left of (a) and (b), it is shown a boxplot of the network-based attenuation coefficient under rain conditions. The bars in the middle of (a) and (b) show a 95% confidence interval for the mean of the network-based coefficients. The right bars in (a) and (b) show a 95% confidence interval of the coefficient retrieved from local disdrometer measurement

The network-based attenuation coefficients were computed for 14 azimuths that display polarimetric signatures of melting ice at 2 UTC on the December 14, 2018, case. Boxplots of these coefficients are shown in Fig. 5.16. These coefficients were computed from the simultaneous observations of CHIVO and CSAPR at 2 UTC in azimuths that display polarimetric signatures of rain. These azimuths range from the 197°azimuth to the 213°. We allow a degree between the angles to avoid samples overlapping between each azimuth. We use the 1.5°elevation angle from the CHIVO radar and the volume scan from the CSAPR to compute the network-based reflectivity.

Fig. 5.16 also shows a 95% confidence interval for the mean of the horizontal and the differential network-based attenuation coefficients. The mean value of the network-based horizontal attenuation coefficient is 0.14, while the differential coefficient is 0.046. Thus, the confidence interval for the mean of the horizontal attenuation coefficients is 0.14 ± 0.02. At the same time, the confidence interval for the mean of the differential attenuation coefficients is 0.046 ± 0.051. These intervals are shown at the middle in each of the plots of Fig. 5.16.

The attenuation correction coefficients for the horizontal and the differential channels are computed from local disdrometers deployed during the RELAMPAGO campaign. Drop size measurements collected by the DOE 2-dimensional video-disdrometer [37] during the RELAMPAGO were used. This disdrometer was deployed near the location of the CSAPR radar during the campaign. Scattering simulations from the disdrometer data from November to December 2018 were conducted. The T-matrix procedure was used at 10°C temperature to conduct the scattering simulations.

A 95% confidence interval is created for the attenuation correction coefficients computed using disdrometer measurements. These intervals are shown in Fig. 5.16 to the left. The confidence intervals for the horizontal and the differential attenuation coefficients are constructed on the slope that relates K_{dp} to the attenuation based on (5.1). The interval for the horizontal attenuation coefficients based on the disdrometer measurement is 0.1515 ± 0.041. Similarly, the interval for the differential attenuation coefficient based on the disdrometer measurement is 0.04163 ± 0.00131. These intervals are shown in each of the plots of Fig. 4.17 to the right.

As can be seen in Fig. 5.16, the confidence interval of the disdrometer and the network-based attenuation coefficients overlap. Moreover, these intervals overlap for both the horizontal and the differential channels. These overlaps translate into a non-significant statistical difference between the coefficients retrieved from the disdrometer and the coefficients obtained from the network-based approach.

5.5 Discussion

This section of the chapter discusses some of the main findings from analyzing the simultaneous radar observations collected by the C-band radars during the RELAMPAGO campaign over melting ice. A comprehensive radar analysis was performed in the region with melting ice. This analysis reveals interesting features of the melting ice characteristics and its polarimetric signatures. The attenuation obtained from the network-based approach and how it is validated is also discussed

5.5.1 Identification of melting ice from simultaneous dual-radar and dual-polarimetric radar observations

The simultaneous observations from CHIVO and CSAPR were used to identify melting ice regions in the radar data. Both radars' measurements display a spike in the differential reflectivity followed by negative values at the same coordinates. The reflectivity and differential reflectivity experienced an enhanced attenuation that the correction algorithm was not able to compensate for satisfactorily due to the melting ice. A comprehensive radar analysis was performed in this region where both radars observed signatures of melting ice. This analysis provides more confidence in identifying melting ice and reveals more features of the melting ice formation.

Vertical analysis of the storm structure is conducted using one of the RHI that crosses the melting ice region. The polarimetric measurements of this vertical cross-section of the storm are shown in Fig. 5.6. As can be seen in this figure, the storm displays two inflows converging in a Z_{dr}

column. These observations could be interpreted as a strong and wide updraft advecting particles from the mid and low levels.

The 3D Doppler winds shown in Fig. 5.8 confirmed that these two inflows converged into the updraft. Furthermore, the Doppler winds displayed a recirculation pattern. One of these inflows could have brought recirculating ice into the new updraft from the previous storm tower. The updraft seems to be strong enough to anchor in the low levels, bringing warm and moist air into the convergence region, which could help the melting process of the ice. The polarimetric signatures of melting ice are also collocated in this region of convergence.

The melting ice also seems to be mixed with other hydrometeor species. Hydrometeor classifications shown in Fig. 5.7 resolved a mix of hail near the Z_{dr} column. The K_{dp} in this region is very high, indicating abundant liquid water content. One of the inflows could have brought this high concentration of liquid water from the low levels. The copolar correlation also decreases significantly, indicating diversity in hydrometeor species and confirming a mixture of phases, as the HydroClass resolved.

The mix phase region resolved by HydroClass seems to be surrounded by large drops, as can be seen in Fig. 5.7. Water-coated ice could have generated some of these large drops. While melting, the ice can shed drops of significant size. These drops can grow fast in the updraft environment by collecting small droplets. The updraft seems to be anchored near the ground and rich in liquid water. These large drops produced from melting ice are more oblate and could explain the wide and high Z_{dr} column observed in the vertical cross-section in Fig. 5.6(b).

Spectral analysis from the IQ data was performed in the region where a mix of phases was resolved by HydroClass. Moreover, one spectrum component displays rain signatures, and the other component of the spectrum displays a signature of melting ice. In addition, the rain component seems to broaden near the mix phase. This broad spectrum could be due to the different size of drops that the melting ice generates along its way in the updraft. The spectrum component that displays the signature of melting ice is significantly lower in power return than the one from rain. Nevertheless, these components dominate the polarimetric returns and the attenuation.

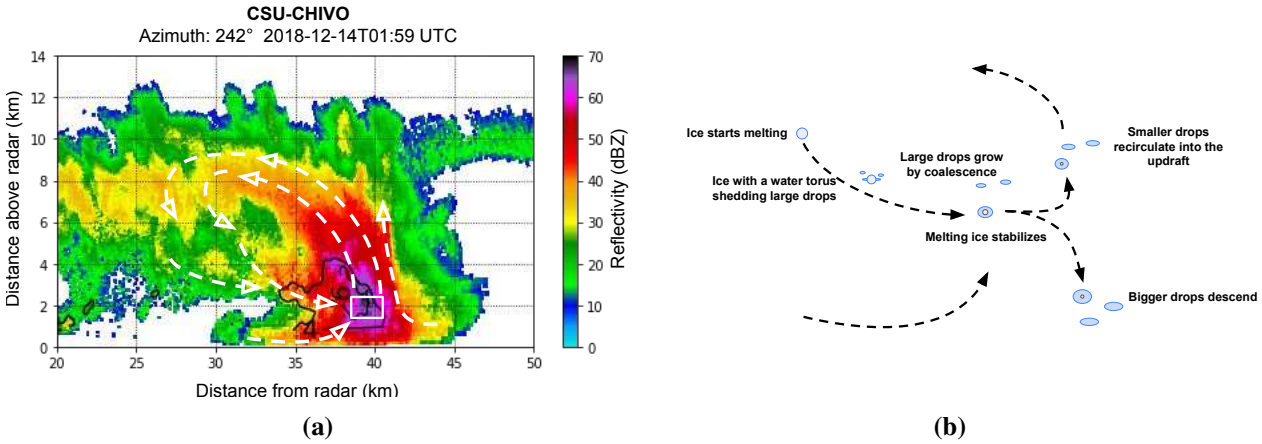

Figure 5.17: Conceptualization of melting ice based on radar observations. In (a) is shown the reflectivity in solid and contours of differential reflectivity starting at 4 dB. The arrows in (a) and (b) indicate the vertical motivation drawn subjectivity following the Doppler winds direction. The square in (b) marks the region where a mix of phases was inferred by hydrometeor classification. (b) shows the interactions of particles in the area marked by the square in (a)

These dual polarimetric and dual radar analyses suggest the presence of melting ice in the region of convergence of inflows and the updraft. This analysis was also used to construct a conceptual model of the melting ice evolution based on the radar observations.

5.5.2 Conceptual model of melting ice from radar observations

The connection between the radar retrievals presented in this study is examined for conceptualizing the processes involved the in melting ice evolution. The RHI taken in the direction of the mixed phase region provides an extraordinary insight into the storm's vertical structure. In addition, the 3D Doppler winds provide evidence of particle recirculation and documentation of the internal storm motions. Furthermore, spectral decomposition improves the identification of mixed phase regions.

Fig. 5.17(a) summarizes the radar observations for the study case that was presented in section IV. This figure shows the reflectivity from the RHI in Fig. 5.6. The solid contours in this figure represent the differential reflectivity. The vertical motion of the storm is drawn subjectively from the Doppler winds retrieval. The square marks the region that was identified as a mix of phases by

the hydrometeor classification. This region also displays a bimodality in the velocity spectrum and a convergence of inflows in the low level Doppler winds.

The mix of phases and convergence of inflows in the region marked by the square in Fig. 5.17(a) suggests that rain and ice converge in a wide updraft, forming a Z_{dr} column. Near this convergence region, the storm displays a Z_{dr} column extending significantly in the vertical. This Z_{dr} column indicates a wide and strong updraft [47]. On the other hand, the two inflows seem to converge in the same region. One of these inflows comes from the low levels and the other one from the mid-levels. In addition, the spectral decomposition shows a bimodality with signatures of melting ice and rain in the region with a mix of phases.

Fig. 5.17(b) shows our interpretation of the interaction between microphysics and the storm's kinematic to produce this unique signature in the radar measurements. This figure represents the processes occurring in the square in Fig 5.17(a). The arrows represent the two inflows and the updraft that converge in this region. It can be seen in this figure the trajectory of an ice particle descending through a region rich in liquid water. The radar observations suggest that the mid-level inflow brings the ice particles into the updraft. These observations also suggest that the low-level updraft advects moisture into the region of convergence.

The interaction of the particle coming from these two inflows in the region of convergence is also explained graphically in Fig. 5.17(b). Ice particles are brought from the mid-level inflow to the updraft, which seems to be rich in liquid water. While the ice particles are descending, the temperatures increase. As a result, the ice particles start melting and develop a torus of water, shedding large drops [48].

The relatively large drops that the melting ice particles shed can then accrete additional water mass in the updraft environment. These large drops collect small droplets in the medium, forming a bigger large drop. These large drops can explain the observed Z_{dr} column and the broaden in the Doppler spectrum. Finally, the melting ice particles sheds large drops until it stabilizes.

When the ice particle stabilizes, it can grow very large by collecting other droplets in the medium. The core of ice can sustain a very large particle size [48]. This very large drop is more

oblate, relative to ice-free raindrops, producing a higher return in the horizontal channel. This high return in the horizontal channel can explain the spike observed in the Z_{dr}.

Some of these descending, melting ice particles and the drops that they shed are advected into the updraft. The biggest particles probably descend to the lowest heights as they recirculate into the updraft, giving them an increased residence time in the updraft. Some of these advected large particles may provide embryos for the large hailstones that were observed later in this IOP.

5.5.3 Estimating the attenuation of melting ice using a network-based approach

A network-based radar approach was used to estimate the radar reflectivity and differential reflectivity in the melting ice. The use of the network-based approach to compute the attenuation in melting ice regions is one of the new aspects of this study. The network-based algorithm uses simultaneous observations from CHIVO and CSAPR, both C-band radars. The concept behind this network-based approach is to match the simultaneous observations from CHIVO and CSAPR to obtain a better estimate of the reflectivity and the differential reflectivity.

As shown previously in this chapter, melting ice exhibits a significantly higher attenuation than rain in the C-band. The C-band needs attenuation correction for quantitative uses [9]. However, melting ice generates an enhanced attenuation that correction algorithms cannot compensate for satisfactory because mainly these correction algorithms are designed for rain attenuation. Fig. 5.4 shows, for example, how the differential attenuation drops to negative values after crossing the melting ice region for both radars.

A previous study has used simultaneous observations from S and C band radars to estimate the attenuation in melting ice [3]. In this study, the S-band has been assumed to be not affected by the melting ice. However, even though the S-band is less affected, scattering simulations have shown that still the S-band can get affected by melting ice [51]. Furthermore, the difference in reflectivity between these two bands depends on the size of hail particles [52].

The network-based approach from simultaneous observation in the same band provides a suitable setup to study the attenuation in melting ice that has not been studied before. Since CHIVO and CSAPR operate in the same C-band, they both respond similarly to the melting ice. The simultaneous observations in the same band can also better characterize the polarimetric signatures of melting ice.

This study focuses on validating the network-based approach over one case to show its potential to study the melting ice attenuation. More cases will be analyzed and presented in future publications by the authors.

5.5.4 Polarimetric signatures of melting ice

The polarimetric signatures that were observed in melting ice regions are discussed. An enhanced Z_{dr} followed by negative values observed simultaneously from CHIVO and CSAPR is used to identify melting ice. The melting ice seems to have some distinct signature in the Z_{dr} and the ρ_{hv}. The physical interpretation of these measurements is discussed and how these observational signatures compare with previous studies.

The differential channel exhibits some distinct characteristics in the melting ice. As can be seen in Figs. 5.13 and 5.14, the Z_{dr} in melting ice seems to display an abrupt increase to values around 8 dB when entering the region with melting ice. The values of Z_{dr} also seem to drop quite dramatically after they spike. The Z_{dr} values stabilize after crossing the melting ice region, generally at negative values. These negative values are attributed to enhanced attenuation. The difference in Z_n and Z_c seems to increase dramatically after the Z_{dr} spikes.

The high Z_{dr} return in melting ice could be due to different reasons, and has been reported by previous studies [2, 47, 53]. A possible explanation for the increase in Z_{dr} could be an increase in the population of large drops. The melting ice generates large drops because of the water the ice sheds while melting. These drops can grow very fast in an updraft environment rich in liquid water content. These large drops also are more oblate and produce a higher return in the differential channel. Another possible explanation is that the melting ice particles produce high Z_{dr} per se. The

melting ice can reach a very large size due to the core of ice that stabilizes the drop. In addition, the melting ice can gain a very high aspect ratio due to the torus it develops.

Regions with melting ice also display a low ρ_{hv}. It can be seen in Fig. 5.11 that ρ_{hv} decreases right before Z_{dr} spikes. It can also be seen in this figure that ρ_{hv} also increases once the Z_{dr} stabilizes. The decrease in the ρ_{hv} in the melting ice regions could be attributed to diversity in sizes and the nature of particles.

Other authors have also found a decrease in ρ_{hv} in melting ice regions, like the simulation from [2, 53]. These authors attribute this low ρ_{hv} to partial beam filling. Nevertheless, the low ρ_{hv} tends to be tied to the melting ice based on the spectral polarimetric that shows a very low coherence in the melting ice part of the spectrum. It could be that the water coat in the ice can start tumbling and can produce a very amorphic shape that makes the copolar correlation decrease.

Once the melting ice portion of the bin is identified, the attenuation correction coefficients are enhanced to match the network-based reflectivity after crossing the melting ice region. This correction can be seen in Fig. 5.12. As shown in Fig. 5.12, the enhanced reflectivity catches the network-based reflectivity at the end of the melting ice region. However, the attenuation seems to be higher at the beginning and progressively catches up along the range. This pattern suggests that the melting ice coefficients vary along the range. This variation of the melting ice coefficients is discussed next.

5.5.5 Variability of the melting ice attenuation correction coefficients

The attenuation coefficients seem to have high variability in the melting ice region. The difference in the corrected reflectivity and the network-based reflectivity at the beginning of the melting ice region in Fig 5.12 suggests a variation in the attenuation coefficients along the range in the melting ice region. It can be seen in this figure that this difference increases until a certain point in the melting ice region. Then, this difference reduces until there is almost no difference between the network-based reflectivity and the corrected reflectivity at the end of the melting ice region. These changes in the difference between the two reflectivities can indicate that the attenuation co-

efficients change along the path, which means that the coefficients are not necessarily perfectly distributed along the melting ice region.

This variability in the attenuation coefficients could be due to differences in the concentration of melting ice particles. As the Doppler winds analysis showed, the melting ice particles seem to be related to the storm motion and how the inflows interact with the updraft. The concentration of melting ice particles can change depending on the inflows and the updraft strength and on which part of the updraft is scanned. In the updraft and its periphery, there could be size sorting and concentration sorting of these melting ice particles. Also, the melting ice can be in different stages, and depending on the stage; the attenuation could be different. As a result, melting ice particles' concentration and stage might change along the path.

The attenuation correction coefficients seem to change in the differential channel as well. As in the piecewise correction from the horizontal attenuation, the differential attenuation might be higher at the beginning of the melting ice region. As can be seen in Fig 5.13, the region with almost 70 dBZ also displays a spike in Z_{dr} of almost 8 dB. On the other hand, this region shows a lower values in the CHIVO's Z_{dr} in Fig. 5.14. This difference could indicate a change in the Z_{dr} correction coefficients.

The network-based coefficient represents the attenuation coefficients' averages in the melting ice region. The coefficients are computed to match the other radar measurements after crossing the melting ice region. This way of computing the coefficients means that the coefficients represent the bulk of the attenuation happening in the melting ice region. The attenuation coefficient seems to vary in this region of melting ice, probably depending on the concentration of ice particles and their drop size distribution. Further work needs to be done to understand the factors that caused this variability.

The attenuation coefficients seem to have a high variability across the azimuth too, as seen in Table 5.2. This table shows the attenuation coefficients for many azimuths that display signatures of melting ice. Azimuths from CSAPR and CHIVO were used to compute the coefficients presented in the table. The attenuation coefficients display high variability, depending on the region

that was scanned, which makes sense since the updraft properties can change and, as a result, the melting ice properties.

This variation in the coefficients was also reported by other authors [3] and [2]. The following section discussed how the coefficients that were computed using the network-based approach compared to those reported by other authors.

5.5.6 Network-based attenuation coefficients in melting ice compared to previous studies

Previous studies have also reported a wide variation in melting ice's attenuation coefficient. The study conducted by [3] shows that the melting ice attenuation in the C-band has a wide variability when compared with S-band observations. The attenuation coefficient average that [3] obtained in their study was 0.66. In our study, an average of 0.44 was found. The slight difference between [3] and our average could be due to the assumption that the S-band is not affected by melting ice made in [3]. Nevertheless, these two averages are close considering the high melting ice coefficient variability.

Scattering simulations at the C-band for melting ice also reported high variability in the attenuation coefficients [2]. These simulations used a thermodynamic model of the melting ice in updraft conditions. This study simulated melting ice of different sizes. High variability in the attenuation coefficients was found for a similar size of melting hail. A dependency on the hail size in the attenuation was also found in this study.

Fig. 5.18 shows how the coefficients found in our study using the network-based method compared to previous studies. The horizontal coefficients are shown in Fig. 5.18 (a), and the differential coefficients are shown in Fig. 5.18 (b). It is shown in each figure a boxplot made from the coefficients that were found using the network-based approach in Table 5.2. The bars in the middle of each plot represent the range of the coefficients found by [2] using scattering simulations from mid and large-melting hail sizes. The dots to the right of each figure represent the coefficients found by directly comparing C-band and S-band simultaneous observations by [3].

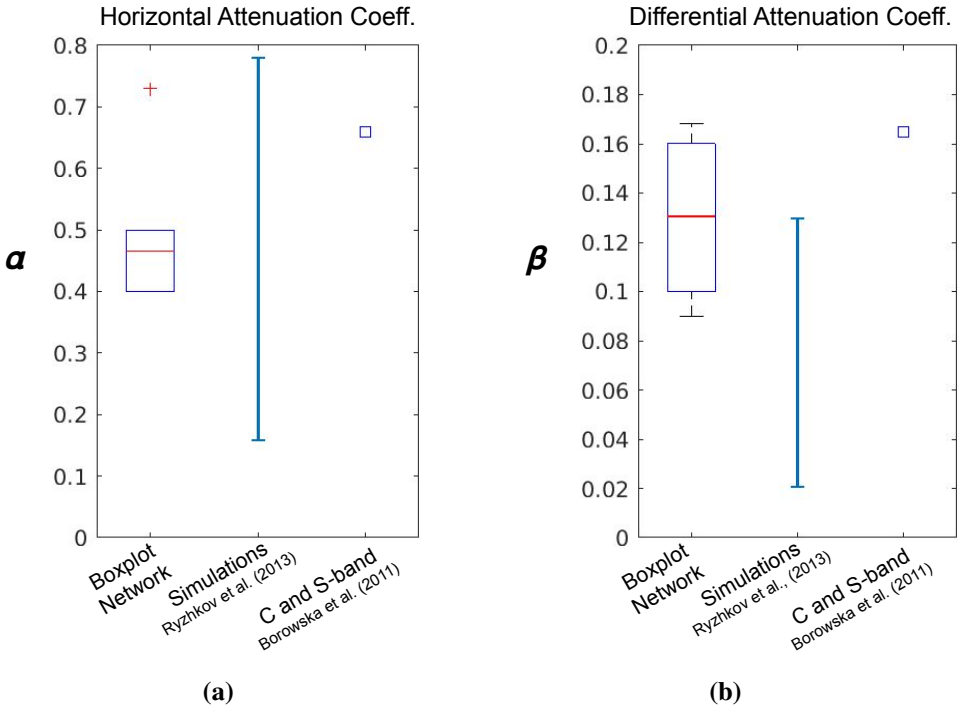

Figure 5.18: Networked attenuation coefficients for melting ice compared with previous studies. (a) shows the horizontal attenuation correction coefficient where $\alpha = a_h/K_{dp}$, and a_h is the horizontal attenuation. (b) shows the differential attenuation correction coefficient where $\beta = a_{hv}/K_{dp}$, and a_{hv} is the differential attenuation. To the left of (a) and (b), it is shown a boxplot for the melting ice coefficients that were found using the network-based approach. The bars in the middle of (a) and (b) represent the variability obtained from the scattering simulation by [2]. The right square in (a) and (b) represents the coefficients found by [3] using direct comparison with S-band observations.

The melting ice coefficients found using the network-based approach compare well with the scattering simulation conducted by [2, 53], as can be seen in Fig. 5.18. The network-based coefficients computed from simultaneous observations of two C-band radars in our study also compared well with the coefficients found using simultaneous observations of a C-band and an S-band radars by [3]. Even the outlier shown by the red cross for the network-based horizontal coefficients lies in the possible range of coefficients reported by [2] from simulations.

The high variability in the attenuation coefficients of melting ice could be due to many factors in the C-band. The melting ice experiences different stages while melting, resulting in different scattering responses in the C-band. The concentration of melting ice particles also plays an important role in attenuation. As discussed previously, a small concentration of melting ice can

significantly impact the C-band measurements. Finally, the part of the updraft that is scanned also seems to affect the attenuation, as the high variability across the azimuth suggests. The updraft strength can change both the concentration and the way the ice melts. Finally, the size of the ice plays an important role since this melting ice particle lies in the Mie scattering regime for the C-band, and resonance can affect the scattering.

Estimating the attenuation of melting ice can provide a valuable measurement that can help to understand microphysical interactions of the melting ice particles in the updraft. In this study, we focus on presenting the network-based approach as a method to obtain the melting ice attenuation. Future studies will focus on how the attenuation of melting ice can tell more about the size, concentration, and stages of the melting ice and how they interact in the updraft in terms of the microphysics.

The following section shows how the network-based approach to computing the attenuation coefficients is validated using disdrometer data.

5.5.7 Validation of the network-based attenuation coefficients using disdrometers

The networked-based approach to compute the attenuation was validated using disdrometers data over rain conditions. During the RELAMPAGO campaign, a disdrometer was deployed near the CSAPR site. The collected data by this disdrometer allows the computation of the attenuation coefficients over rain. The same network-based approach used to compute the attenuation coefficients over melting ice was also used to compute the coefficients over rain. The attenuation coefficients from the disdrometer and the network-based were compared to validate the network-based approach's ability to compute the attenuation coefficients.

A 95% confidence interval was created for the attenuation coefficients from the disdrometer and the network-based approach. These confidence intervals were created for the horizontal and the differential attenuation correction coefficients. As can be seen in Fig. 5.16, the disdrometer and the network-based approach intervals overlap for both the horizontal and the differential atten-

uation correction coefficients.

The overlap in the confidence intervals means that there is no significant statistical difference between the coefficients retrieved from the disdrometer and the coefficients retrieved from the network-based approach. Therefore, the network-based approach presented in this chapter provides a reliable tool to compute the attenuation correction coefficient. Thus, this method should also be valid for computing the attenuation coefficients over melting ice.

5.6 Summary

Due to the proliferation of C-band radars, the study of melting ice attenuation has become more critical, especially in the tropics and subtropics. The C-band radars need attenuation correction, and the melting ice produces an enhanced attenuation that regular correction algorithms cannot compensate satisfactorily for. In this study, the C-band radars deployed during the RELAMPAGO campaign were used to study the melting ice and its attenuation. A network-based approach was used to estimate the attenuation of regions exhibiting polarimetric melting ice signatures. The network-based approach to estimating the attenuation in the C-band is one of the new aspects of this study. A comprehensive radar analysis of the regions with melting ice is also a new aspect of this study. These radar analyses reveal new aspects of the melting ice in an observation way. The analyzes conducted in this study included Doppler wind, RHI analysis, spectral decomposition, and hydrometeor classification over regions with melting ice. Some of the conclusions for this study are the following:

1. Simultaneous dual radar observations in the C-band display similar polarimetric characteristics in regions with melting ice. CHIVO and CSAPR observed spikes in Z_{dr} followed by negative values downrange. The polarimetric signatures in this area display values of Z_{dr} of around 8 dB in the region with melting ice. The Z_{dr} values then drop until they become negative due to the lack of ability of the attenuation correction algorithms to compensate for the attenuation satisfactory in regions with melting ice. ρ_{hv} also tends to decrease in the region with melting ice, increasing again when Z_{dr} stabilizes.

2. The spectral decomposition confirmed a mix of phases in the region identified with melting ice. Moreover, the spectral decomposition shows that this region is mostly compounded by rain. The power return of rain is three orders of magnitude higher than the part of the spectrum with polarimetric characteristics of melting ice. However, the polarimetric variables are mainly by the melting ice part of the spectrum.

3. The Doppler winds show a recirculation of particles where melting ice was identified. A Z_{dr} column was also collocated at this region with melting ice. The Doppler winds also show a convergence of two inflows in the Z_{dr} column. One of the inflows seems to transport the ice from the upper levels, and the other inflow seems to bring warm and moist air into the updraft from the low levels. A conceptual model of the evolution of the melting ice in these conditions was also presented.

4. The attenuation of melting ice in the C-band was obtained using a network-based approach. The simultaneous radar observations from CHIVO and CSAPR were used to obtain a better estimate of the attenuation than for a single radar estimation. The Horizontal attenuation and the differential attenuation were computed for many radar bins that exhibit polarimetric signatures of melting ice from both of the radars. Statistics of these coefficients were also created from the radar bins that were found to have polarimetric signatures of melting ice.

5. The melting ice attenuation correction coefficients vary significantly in the region identified with melting ice. This variation could be due to the sensitivity of the C-band to the concentration of melting ice particles. It could also be that the melting ice concentration changes in different parts of the updraft, and as a result, the response of the radar also changes. The resonance effects also seem to affect this variation. Previous studies have also reported a wide variation in the attenuation correction coefficients.

6. The melting ice coefficients in the C-band computed using a network-based approach compared well with the coefficients in the literature using direct C- and S-band [3] comparison

and simulations [2, 53]. These studies also reported a wide variability of the attenuation correction coefficients.

7. The network-based approach that was used to compute the attenuation in melting ice was validated using disdrometer data over rainy conditions. First, the network-based attenuation correction coefficients were computed over rain. Subsequently, these coefficients were compared with coefficients retrieved from the disdrometer deployed during the campaign on the ground. The network-based coefficients and the disdrometer coefficient shows a nonsignificant statistical difference. As a result, the network-based approach is reliable for computing the attenuation correction coefficients. Therefore, this method should be valid to compute the attenuation coefficients over melting ice.

This study shows the potential of using the network-based approach to compute the melting ice in the C-band. A study case with melting ice is presented and analyzed in detail with advanced radar tools. The authors will analyze more cases of melting ice in the future.

Chapter 6

Dual polarization spectral analysis in updraft environments

6.1 Introduction

This chapter presents spectral polarimetric decomposition from I&Q radar samples in updraft environments. First, updrafts are identified using dual Doppler analysis and polarimetric signatures of updrafts such as Z_{dr} columns. Subsequently, the power spectrum (sZ), differential spectrum (sZ_{dr}) and coherence spectrum $(s\rho_{hv})$ are computed from I&Q radar samples obtained from the identified updrafts. Practical considerations about the spectrum computation from I&Q radar samples in updraft are also presented. The spectral analysis revealed that bimodalities in the spectrum can be found in updraft conditions. Furthermore, the separation in the spectrum of different kinds of particles allows us to study the microphysics of each set of particles in a mixed-phase scenario.

The network of C-band radars deployed during the RELAMPAGO campaign in Argentina is used in this study. CSU-CHIVO radar and the CSAPR-2 are used to perform dual Doppler analysis. The Dec. 14, 2018 case is analyzed. These two radars recorded a squall line between them during the Dec. 14 case, allowing the retrieval of the 3D wind field. In addition to the Doppler winds, CSU-CHIVO also recorded Range Height Indicator (RHI) scans in the direction where updrafts were identified, allowing vertical analysis of the storms. The I&Q time samples from CSU-CHIVO's RHIs are used to compute the polarimetric spectrum.

The spectral polarimetric can provide a huge insight into the microphysics of updrafts, their composition, and their evolution. The spectral polarimetric expands the radar variables in the Doppler spectrum. This variable can be studied in the full spectrum to infer particles' composition and concentration in a mix-phase scenario, commonly occurring un updraft. In addition, the size of the particles and size sorting of particles can be resolved with enough constraints from the spectral

analysis. However, the estimation of the spectrum in updraft environments required additional processing.

The computation of spectra is particularly challenging in updrafts since, in these environments, there is more turbulence. As a result, the spectrum tends to broaden, and the noise floor increases, making it challenging to separate signal from noise. As a result, special digital signal processing techniques need to be applied to estimate the spectrum in such conditions.

Polarimetric spectra have been computed in the past for filtering processing mainly [61] [62] [63]. However, the study of microphysics using the spectrum is relatively new. Simulations have been conducted to study how the spectrum behaves in different conditions [24]. However, the spectrum in updraft environments has not been shown in an observational way. This literature gap could be due to the need for a dataset from multiple radar observations to identify updraft environments. In addition, the estimation of the spectrum itself in such conditions is challenging. Some preliminary use of spectral polarimetry has been conducted by [64].

This chapter explores signal processing to obtain a clean spectrum in updraft environments. The more effective signal processing techniques are then chosen to estimate the spectrum in an identified updraft. Important considerations in computing the spectrum are also shown. The updrafts are identified using Doppler winds from CHIVO and CSAPR radars. The polarimetric spectrum from a ray that passes by one of the identified updrafts is shown. The microphysics of this updraft is analyzed, and the spectral decomposition infers the composition of the particles.

This chapter is organized as follows. The methods section presents the definition of the dual parametric spectra used in this study and their mathematical expressions. This section also explains two different ways the spectrum can be computed. Finally, the digital signal processing that is applied to the spectrum is also shown in this section. The Data section shows how the I&Q data were obtained for this investigation and the advantage of using RHI IQ data to compute the spectrum. It also shows how the updraft was identified for this case. The Results section walks the reader through the different ways the spectrum was computed until a clean spectrum was obtained after all the applied signal processing. This section also shows the spectrum for the identified updraft. The

discussion discussed the lessons learned by computing the spectrum from updraft environments and presented an analysis of the polarimetric spectrum from the updraft. Finally, the key points from this chapter are summarized in the conclusion section, and possible routes that can be taken in this investigation are shown.

6.2 Methods

Polarimetric spectral decomposition was performed over melting ice regions to understand more about the nature of the particles and how they dispersed over the Doppler spectrum. The in-phase and quadrature (I&Q) time sequences of the vertical and horizontal channels were acquired by the CSU-CHIVO radar deployed during the RELAMPAGO campaign.

When particles move at different velocities, they display a separation in the Doppler velocity spectrum [61, 65]. As a result, one can study the polarimetric signatures of particles in a mixed-phase scenario, as is the case of the melting ice.

The power spectrum (sZ), the differential spectrum (sZ_{dr}), and the coherence spectrum (sρ_{hv}) were computed for melting ice regions. This part of the chapter explains the mathematical expression that defined these spectra.

6.2.1 Estimation of the spectrum, FFT and autocorrelation

Polarimetric spectral decomposition was performed over melting ice regions to understand more about the nature of the particles and how they disperse over the Doppler spectrum. IQ time sequences of the vertical and horizontal channels were acquired by one of the C-band radars deployed during the RELAMPAGO campaign.

When particles move at different velocities, they display a separation in the Doppler velocity spectrum [61, 65]. As a result, one can study the polarimetric signatures of particles in a mixed-phase scenario, as is the case of the melting ice.

The power spectrum (sZ), the differential spectrum (sZ_{dr}), and the coherence spectrum ($s\rho_{hv}$) were computed for melting ice regions. The way these spectra were computed are explained in this part of the article.

6.2.2 Power spectrum (sZ)

The power spectrum represents the spectral decomposition of the reflectivity (Z). The power spectrum can be estimated by computing the power spectral density of the horizontal channel. The compensation due to the range and the radar constant should be included to make the values comparable to the reflectivity [62]. Hence, the spectral decomposition of the reflectivity in dB is given by the following expression:

$$sZ = S_{hh}(v) + 20\log_{10}(r) + C \quad \text{in db} \tag{6.1}$$

Where $S_{hh}(v)$ is the power spectra density of the received signal in the horizontal channel, r is the range, and C is the radar constant. The two last parts on the right side of (6.1) make the Doppler power spectrum comparable to reflectivity values.

6.2.3 Differential spectrum (sZ_{dr})

The differential spectrum can be seen as the spectral decomposition of the differential reflectivity (Z_{dr}). The differential spectrum can be calculated as the ratio of the horizontal and vertical power spectra [61, 65] in the following way:

$$sZ_{dr}(v) = \frac{S_{hh}(h)}{S_{vv}(v)} \tag{6.2}$$

Where $S_{vv}(v)$ is the power spectral density of the vertical channel. Note that the ratio is in linear units. In dB, this ratio becomes a difference. Note that the range and the C dependency cancel in the differential spectrum. Hence, only the power spectral density in the horizontal and the vertical channel are needed to compute the differential spectrum.

6.2.4 Coherence spectrum ($s\rho_{hv}$)

The coherence spectrum can be seen as the decomposition of the copolar correlation (ρ_{hv}) over the Doppler components v. The coherence spectrum can be computed as the module of the coherence function [61, 65] as follows:

$$s\rho_{hv} = \frac{|C_{hv}(v)|}{\sqrt{|S_{hh}(v)S_{vv}(v)|}} \tag{6.3}$$

where C_{hv} is the copolar cross-spectrum. Some examples of spectral decomposition over melting ice are presented in the results section in Figs. 6.16 and 6.17.

C_{hv} is the Fourier transform of the cross correlation between the horizontal and vertical channels. In other words, the following expression:

$$C_{hv}(v) = FFT(R_{hv}(n))(v) \tag{6.4}$$

And S_hh and S_vv are the power spectrum estimates of the horizontal and vertical channels.

6.2.5 Autocorrelation method

The estimation of the power spectrum is carried out in different ways. The spectrum computation from samples is an estimation of the PSD of the radar signal. The definition of the PSD is the Fourier transform of the autocorrelation function. As a result, the autocorrelation of the samples needs to be obtained to estimate the spectrum. In this way, a complex signal of the horizontal channel is first obtained:

$$H(n) := H_I(n) + jH_Q(n) \tag{6.5}$$

Where j is the imaginary unit.

$H(n)$ is the samples of the continuous signal $H(t)$. An estimation of the autocorrelation can be obtained using the crosscorrelation of the samples, defined as:

$$\hat{R}_{xy} = \begin{cases} \sum_{n=0}^{N-m-1} x_{n+m} y_n^*, & m \geq 0 \\ \hat{R}_{xy}^*(-m), & m < 0 \end{cases}$$

The output vector, c, has elements given by

$$c(m) = \hat{R}_{xy}(m - N), \quad m = 1, 2, ..., 2N - 1. \tag{6.6}$$

$R_{HH}(n)$ now has a length of $2N - 1$ where N is the number of samples used to compute the autocorrelation, in this case, 99. Note that when the autocorrelation is done, the energy of the signal increases to the square.

Now the spectrum can be estimated by computing the Fourier transform of the autocorrelation. This is done via the fast Fourier transform (FFT) in the following way:

$$S_{HH}^2(v) = FFT(R_{HH})(v) \tag{6.7}$$

To compute the spectrum and make it comparable with the reflectivity values, we can scale the values of $S_{HH}^2(v)$ as follows:

$$sZ(v) = 20 * log_{10}\left(\left|\frac{PRT}{N_s} * S_{HH}^2(v)\right|\right) + 20 * log_{10}(R) + c \tag{6.8}$$

Where PRT means the pulse repetition time of the radar, which is the inverse of the PRF, N_s is the number of samples, in this case, 99, R the range, and C the radar constant.

Since the estimate of $S_H H$ is to the square in (6.7), then (6.8) can be expressed as:

$$sZ(v) = 20 * log_{10}\left(\left|\frac{PRT}{N_s} * FFT(R_{HH})(v)\right|\right) + 20 * log_{10}(R) + c \tag{6.9}$$

This estimation of the spectrum does not take into account the windowing process. The equation above shows the way the power spectrum should be computed. However, this spectrum corresponds to applying a rectangular window.

6.2.6 An alternative way to compute the spectrum, the direct Fourier method

The discrete Fourier transform is also another way to estimate the power density spectrum of a signal [66]. Using this property of the Fourier transform, the autocorrelation of the samples can be skipped to compute the power spectrum. For the cross-correlation of the H and V channel, the direct Fourier method can also be used by applying correlation properties in the spectrum. The correlation can be seen as a convolution with an inverse sign. This inverse sign in the spectrum at the same time can be seen as the conjugation of a sequence. As a result, the cross-power spectrum can be obtained by a multiplication of the H and V channel power spectral densities and conjugating one of them.

$$sZ(v) = 20 * log_{10}\left(\left|\frac{PRT}{Ns} * FFT(H(n))(v)\right|\right) + 20 * log_{10}(R) + c \tag{6.10}$$

Where $H(n)$ is the complex signal defined in (6.5).

6.3 Data

The network of C-band radars deployed during the RELAMPAGO campaign in Argentina is used in this study. CSU-CHIVO radar and the CSAPR-2 are used to perform dual Doppler analysis. The Dec. 14, 2018 case is analyzed. These two radars recorded a squall line between them during the Dec. 14 case, allowing the retrieval of the 3D wind field. In addition to the Doppler winds, CSU-CHIVO also recorded Range Height Indicator (RHI) scans in the direction where updrafts were identified, allowing vertical analysis of the storms. The I&Q time samples from CSU-CHIVO's RHIs are used to compute the polarimetric spectrum.

6.3.1 I&Q time series from the RELAMPAGO campaign

The data for this investigation is obtained using the CSU-CHIVO radar. CHIVO radar was located South of Cordoba. CSU-CHIVO was brought to Argentina as part of the RELAMPAGO campaign. CSU-CHIVO has a dual polarization capability and a Sigmet processor. The signal processor of Sigmet has the capability to obtain I&Q time samples. IQ time series are samples of the baseband received radar signal. The radar receives the signal in a high microwave frequency of microwave of 5 GHz. The signal is brought to the baseband using multiplication and a low pass filter.

The in-phase and quadrature components are found by decomposing the radar signal into its real and complex components by using orthogonal functions. Since the sine and the cosine are orthogonal functions, then the radar received signal can be expressed as:

$$X(t) = I(t)sin\,(2\pi f_c t) - Q(t)cos\,(2\pi f_c t) \tag{6.11}$$

In this way, the complex envelope of the radar signal can be expressed in the base-band as the complex signal defined as:

$$X(t) = I(t) + jQ(t) \tag{6.12}$$

Where $X(t)$ is the base-band signal, I and Q the in-phase and quadrature component and j the imaginary unit.

The I&Q signals are then sampled and they enter the digital signal processor of the radar. Then, the radar variables, such as reflectivity and radial velocity, are computed from these samples.

The CSU-CHIVO radar obtained the I&Q samples. The I&Q data, nevertheless, are very large to store. To compute each radar variable, the equivalent of 64 samples are used. As a result, storing the I&Q samples requires about one and a half orders of magnitude more than storing the radar variables such as reflectivity. As a result, for the RELAMPAGO campaign, not all the time series were stored. However, for the December 14 case, time series were recorded.

6.3.2 Updraft and mix phase identification

We use the Doppler wind and dual-polarization observations from the CHIVO radar and CSAPR to identify updrafts. The study case we are using is December 14 at 2 UTC. We can see from this case an RHI in Fig.6.1, which is shown at azimuth 242 deg. One can see in this RHI that a Z_{dr} column is exhibited. The Z_{dr} column is a sign of an updraft. The Doppler winds reassure the presence of an updraft in this region. The Doppler winds were drawn subjectively in Fig. 6.2.

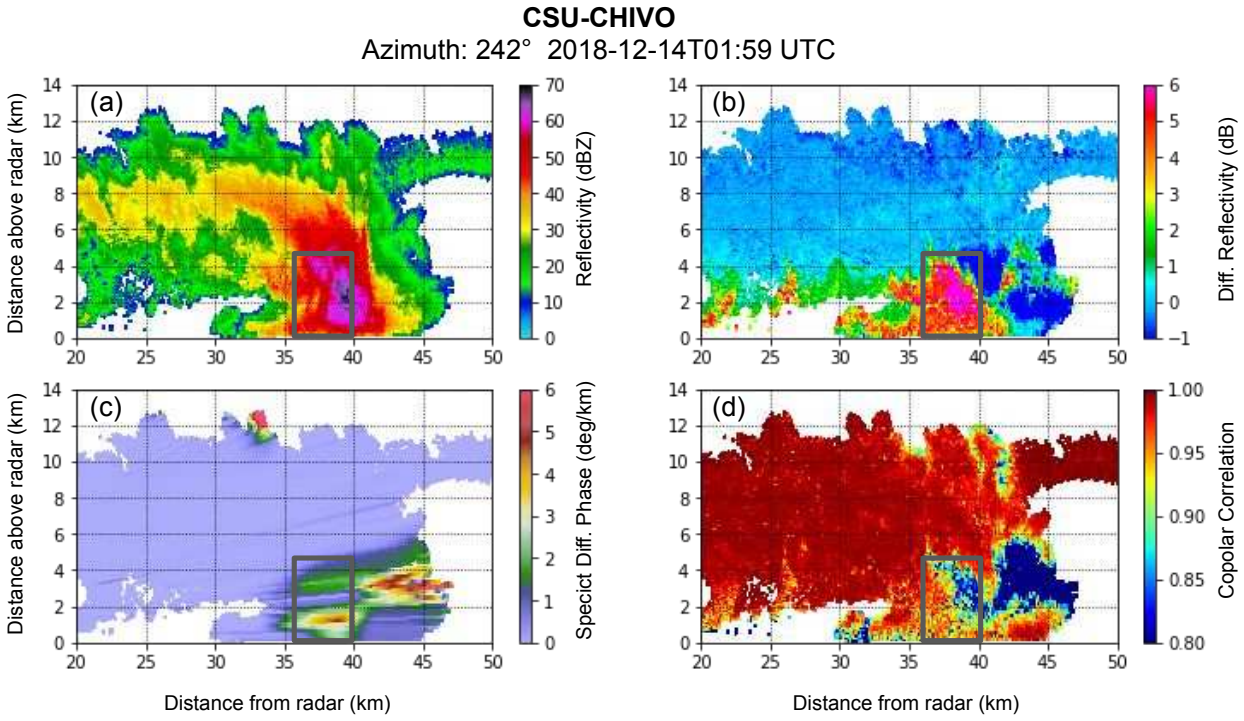

Figure 6.1: Reflectivity (a), differential reflectivity (b), specific differential phase (c), and copolar correlation (d) of the RHI in CSU-CHIVO radar where updraft was identified

Hydrometeor classification shown in Fig. 6.3 shows a mixed phase in the low elevation which makes sense due to the two inflows that converge in the square in Fig.6.1. As a result, this area is very suitable to study the spectral decomposition in this region to see how the polarimetric spectral behave in this region of mix phase and which insights the polarimetric spectral decomposition can provide.

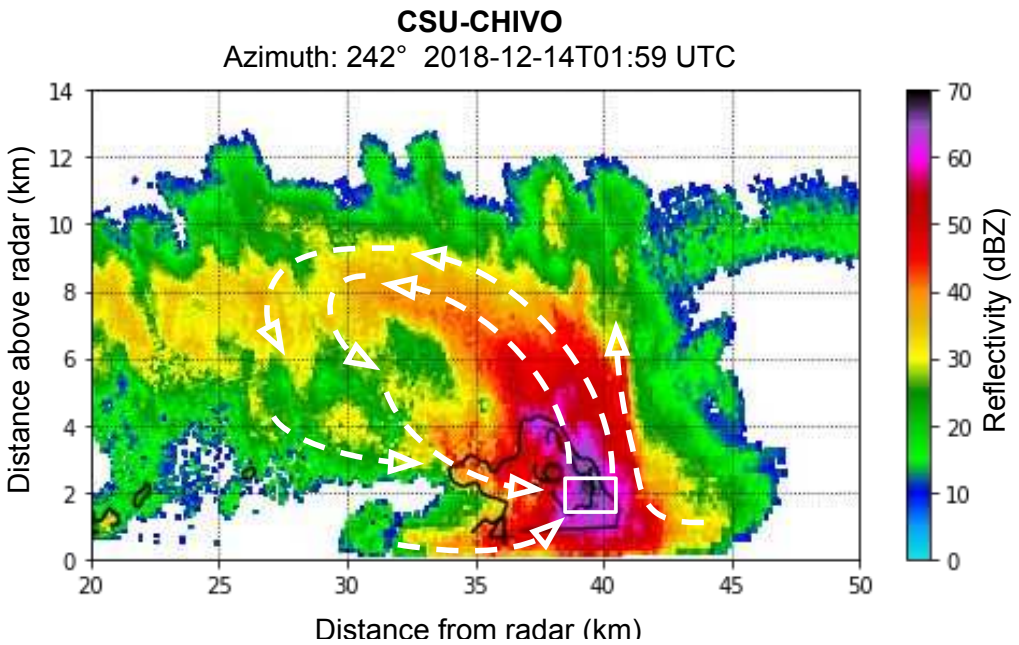

Figure 6.2: Reflectivity (solid), differential reflectivity (contours), and Doppler winds for the RHI of CHIVO radar in Fig. 6.1

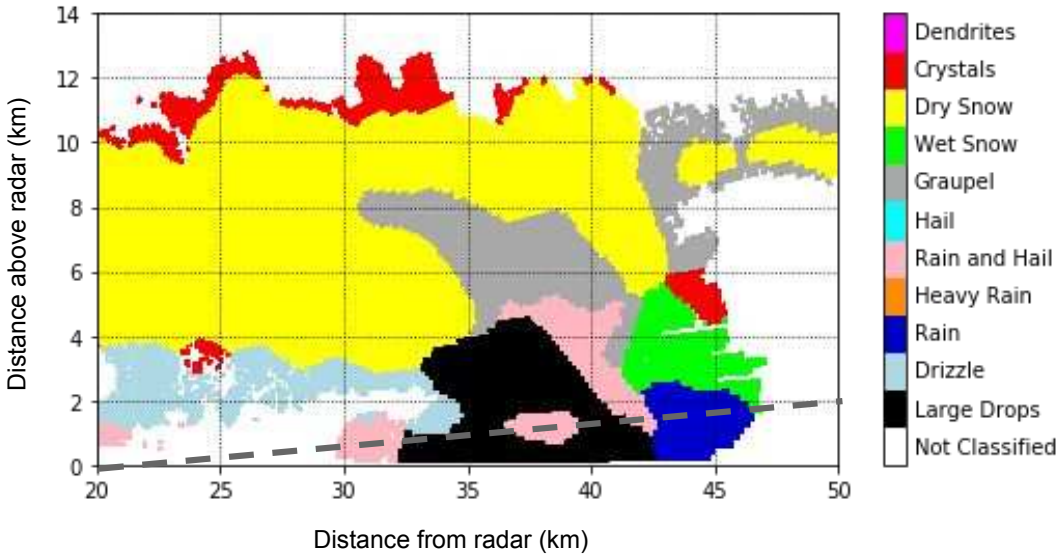

Figure 6.3: Hydrometeor classification inferred from the polarimetric measurements in Fig. 6.1

As can be seen in Fig. 6.2, this RHI displays a Z_{dr} column which is a sign of an updraft. The RHI also shows a convergence of another inflow from the mid-levels. It can also be seen from the Doppler wind that recirculation is observed near 38 km. From the hydrometeor classification in Fig. 6.3, it is possible to see that we have a mix of phases in this region; as a result, one has a

unique composition of polarimetric evidence of mix phase in an updraft environment. As a result, one would expect to observe in the spectral decomposition of a bimodality.

6.3.3 Advantage of RHI samples

The angle that is used to compute the spectrum is the 2.5 deg in elevation and azimuth 242 from the RHI taken at 01:59 on December 14, 2018, taken by CHIVO radar. This radar ray crosses a region of the mix phase at around 38 km, as can be seen in the hydrometeor classification in Fig. 6.3.

The RHI in Fig. 6.1 is used to compute the spectral decomposition. These RHI data are very valuable because there are many samples per degree in an RHI, which make this type of scan more suitable to conduct spectral decomposition. This provides the advantage of obtaining a better spectral decomposition. One can perform more averaging and reduce noise in the data.

For this RHI, the radar was operating in a single PRF. This scheme provides the advantage of simplifying the spectral decomposition because the samples are taken at the same time separation. Single PRF configuration provides the advantage of averaging the spectrum with the same properties and number of the same with a large number of samples. As a result, one can reduce the noise in the data.

The I&Q channel samples are taken over time, with the interval depending on the radar's PRF. Each sample corresponds to a specific location in the radar's polar coordinates. Since the radar rotates while sampling, there may be some variation in the pointing angle, but for our RHI case, this variation is only 0.2 deg to obtain 99 samples. This variation or delta in the pointing angle is considered good since 99 samples are acquired within this 0.2 deg delta. It's important to keep in mind the tradeoff between the number of samples and the width of the delta, as too many samples can lead to a broader delta. Still, more samples can also help with averaging and noise reduction during signal processing.

Let's suppose the following samples are used to compute the power spectrum:

$$H_I(n), \quad H_Q(n), \quad V_I(n), \quad V_Q(n). \tag{6.13}$$

Where H and V are the horizontal and the vertical channels of the dual-polarization radar, I and Q the in-phase and quadrature components, and $0 < n < N$ are the samples, with n from 1 to 99.

These samples are used to compute the spectrum via the Fourier transform. The Fourier transform provides a representation of this signal in the Doppler velocity domain. The Ts or the time of samples corresponds to the inverse of the PRF. The formula that relates the radial velocity with the frequency shift from the Fourier transform can be expressed as:

$$f_d = \frac{2v_r}{\lambda} \tag{6.14}$$

Where f_d is the frequency obtained from the Fourier transform, v_r the corresponding radial Doppler velocity and λ the wavelength of the radar.

6.4 Results

The dual-polarimetric spectrum is obtained for the region of a mixed phase and a convergence of inflows shown in Figs. 6.1 and 6.2. These spectra are presented in this section.

6.4.1 Power spectrum (sZ) estimation, insights from the autocorrelation and the Fourier transform

The power spectrum can be estimated in different ways. This part of the document discusses how the power spectrum should be computed in updraft environments. In addition, the power spectrum is computed in different ways to understand practical aspects of estimating spectrum in updraft environments.

By calculating the power spectrum, we can understand how the reflectivity is distributed across the Doppler velocity domain, indicating which part of the spectrum has the most energy. To do this, we need samples from the in-phase and quadrature (I&Q) channels, which correspond to the

real and imaginary parts of the complex envelope of the received signal. The radar's digital signal processor processes these samples to compute the reflectivity and other radar variables.

To compute the power spectrum, let's use the horizontal channel, i.e., the I&Q samples of the horizontal channel, i.e., the $H_I(n)$ and the $H_Q(n)$ from (6.13). Two methods are used to compute the power spectrum ($sZ(v)$), one is the autocorrelation, and the other one is the direct Fourier transform. The angle that is used to compute the spectrum is the 2.5 deg in elevation and azimuth 242 from the RHI taken at 01:59 on December 14, 2018, taken by CHIVO radar. This radar ray crosses a region of the mix phase at around 38 km, as seen in the hydrometeor classification in Fig. 6.3.

The power spectrum was calculated for the ray mentioned above. In this case, we first use a Blackman window to multiply the autocorrelation before computing the Fourier transform in the following way:

$$sZ(v) = 10 * log_{10}\left(\left|\frac{PRT}{N_s} * FFT(R_{HH}(n) * w_B(n))(v)\right|\right) + 20 * log_{10}(R) + C \qquad (6.15)$$

Where w_B is a Blackman window of size of $2N - 1$, the same size as the autocorrelation. The Blackman window is chosen because it provides the biggest sidelobe mitigation, and the main sidelobe is wider, providing a smooth spectrum effect. Fig. 6.4 shows how the power spectrum looks like using the configuration in (6.15):

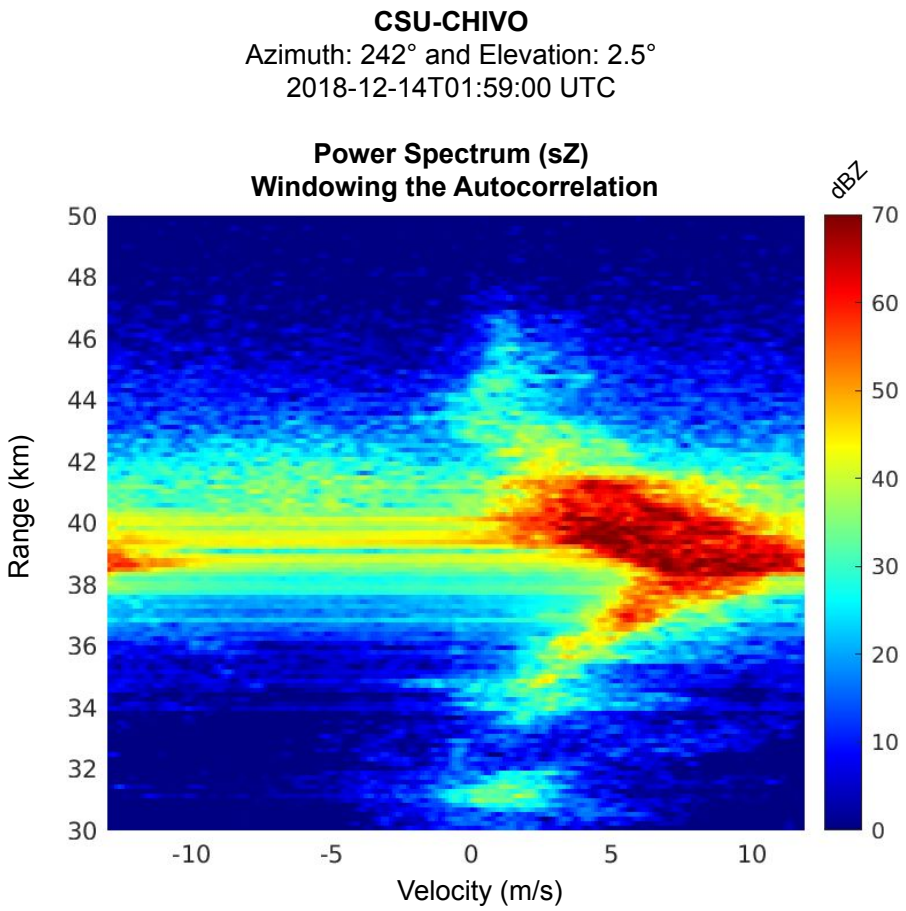

Figure 6.4: Power spectrum estimates using the autocorrelation method. The autocorrelation is multiplied with a Blackman window

Using the Blackman window to multiply the correlation as in (6.15), one can see a significant interference of the side lobes, and a striped pattern appears. In Fig. 6.4, one can see stripes from the 38 km extending along the velocity, and it is not possible to distinguish the spectrum values in the negative velocities because these stripes cover them.

The spectrum shown in Fig. 6.4 is estimated using the autocorrelation method. Another way to compute the power spectrum is by using the alternative direct Fourier transform over the samples [66]. As it is mentioned before, the power spectrum can be estimated as follows:

$$sZ(v) = 20 * log_{10}\left(\left|\frac{PRT}{Ns} * FFT(H(n))(v)\right|\right) + 20 * log_{10}(R) + C \tag{6.16}$$

Where H(n) is the complex signal defined (6.5).

In this case, since the autocorrelation is not used, the number of samples of the spectrum estimation is N. A Blackman window of length N is used before the Fourier transform as follows:

$$sZ(v) = 20 * log_{10}\left(\left|\frac{PRT}{Ns} * FFT(H(n) * w_B(n))(v)\right|\right) + 20 * log_{10}(R) + C \tag{6.17}$$

When the power spectrum is estimated using the direct Fourier transformation described in (6.17), one obtained the following estimation:

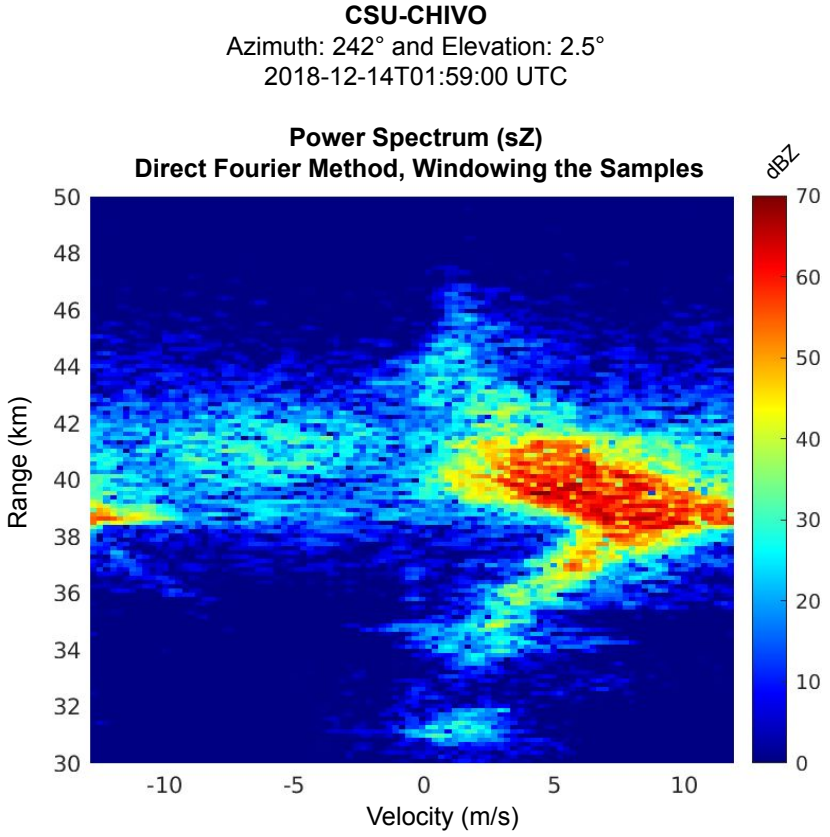

Figure 6.5: Power Spectrum estimate using the direct Fourier transform method and a rectangular window

When the Power Spectrum is estimated using the direct Fourier method, it is possible to see that the striped pattern in Fig. 6.4 is mitigated. With the direct method (Fig. 6.5), it is possible to see more clearly the part of the spectrum that was covered by the stripes in the autocorrelation

method (Fig. 6.4), especially in the negative velocities. It is more clear in Fig. 6.5 a bimodality in the spectrum starts from 38 km. This reduction and mitigation of the striped pattern question why the direct Fourier method provides a better spectrum estimation than the autocorrelation.

To answer this question, the power spectrum is computed not using a window to see how the spectrum would look like by using a rectangular window with the direct Fourier method. Fig. 6.6 shows how the power spectrum looks like using a rectangular window and the direct Fourier method:

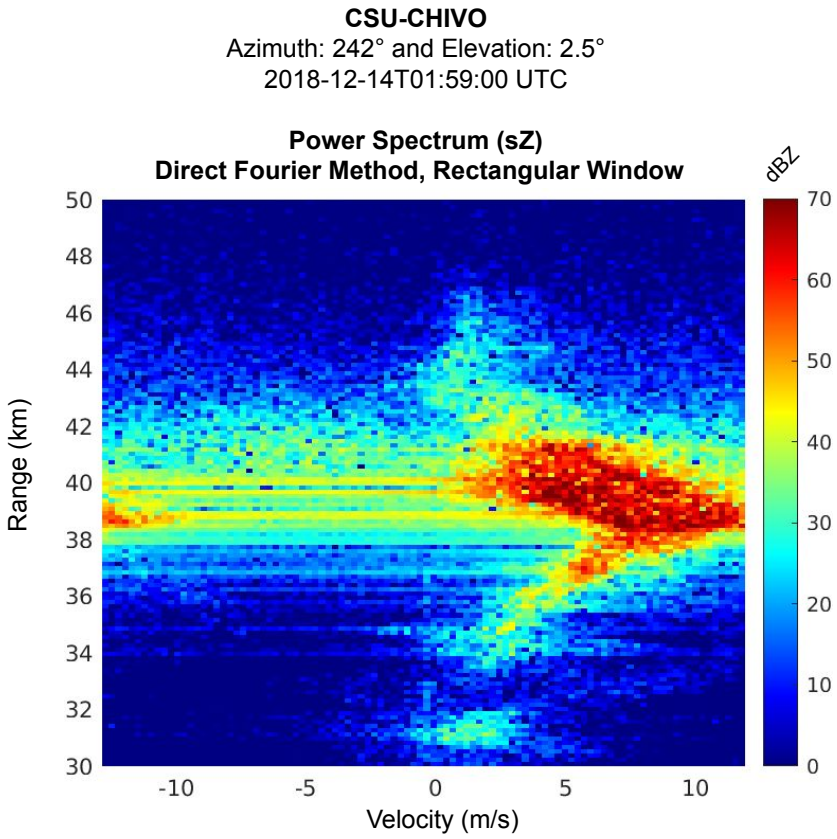

Figure 6.6: Power Spectrum estimate using the direct Fourier transform method and a rectangular window

Using a rectangular window with the direct Fourier method, it is possible to see that the spectrum estimate looks very similar to the one using the autocorrelation method in Fig. 6.4. This provides a hint of a possible windowing of the samples before applying the autocorrelation would help to estimate the spectrum better using the autocorrelation method.

As a result, the samples are windowed using a Blackman window, and then the autocorrelation is computed to estimate the spectrum using the autocorrelation method in the following way:

$$R_{HH}(n) = H(n) * W_B(n) * *H(n) * W_B(n) \tag{6.18}$$

Subsequently, the Fourier transform is computed to estimate the power spectrum using the autocorrelation method. Fig. 6.7 shows the estimate of the power spectrum using the autocorrelation method but this time windowing the samples with a Blackman window:

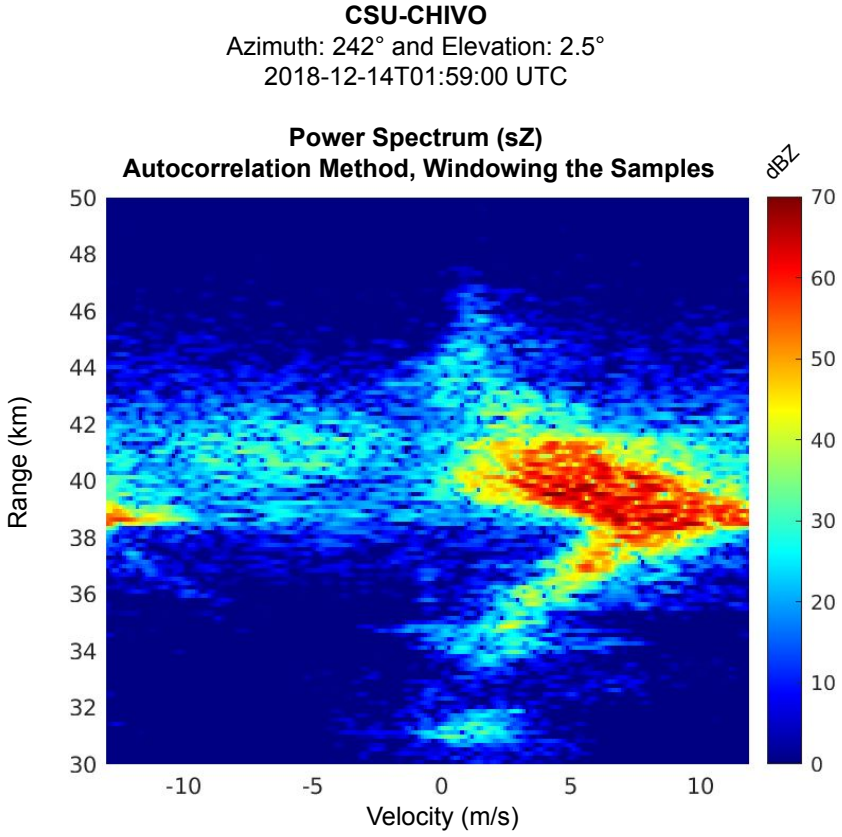

Figure 6.7: Power spectrum estimate using the autocorrelation method and multiplying the samples with a Blackman window

Note from Fig. 6.7 that the spectrum looks very similar to the one obtained using the direct Fourier transform in Fig. 6.5. The striped pattern is mitigated, and now we can better observe the spectrum with the autocorrelation method.

6.4.2 Coherence spectrum, challenges and practical considerations

The autocorrelation method is used to compute the coherence spectrum. The correlation is used to estimate the cross-polar spectrum C_{hv} and the horizontal and vertical power spectrum. These correlations are windowed in the power spectrum to obtain a better spectrum estimate as in Fig. 6.4. Using the same 99 samples as in the estimation of the power spectrum, the coherence spectrum is estimated.

The coherence spectrum can be seen as the spectral decomposition of the copolar correlation. It can be seen as the values of the copolar correlation along the Doppler velocity.

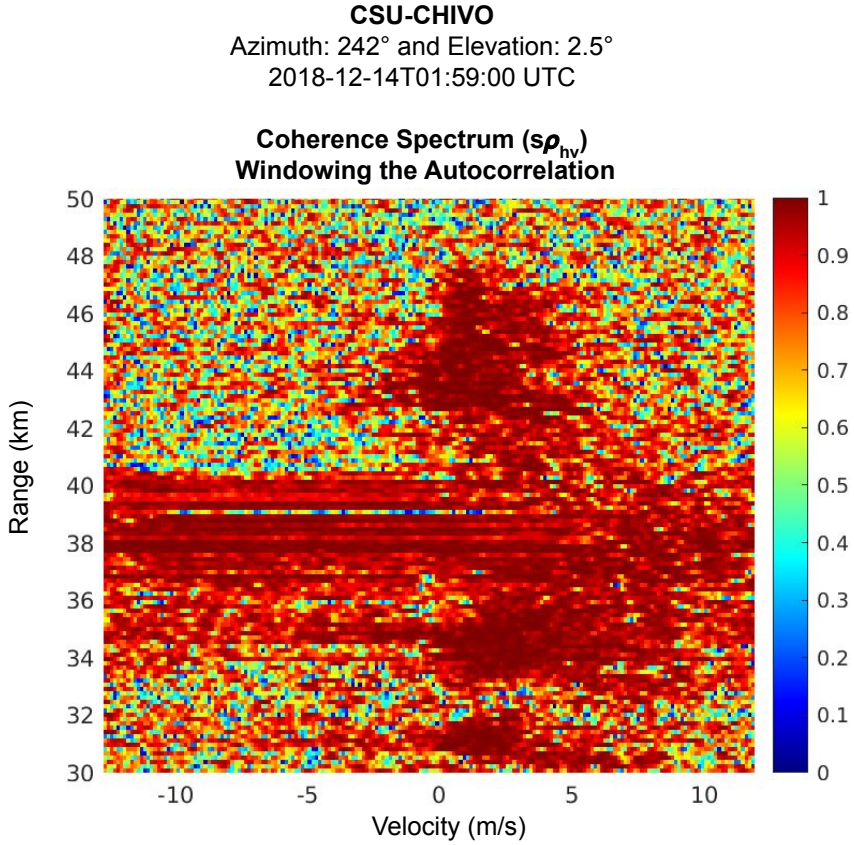

Figure 6.8: Coherence spectrum computed using a Blackman window to multiply the autocorrelation and the cross-correlation

Fig. 6.8 shows the coherence when a Blackman window is used to multiply the correlation and crosscorrelation necessary to compute the coherence spectrum according to (6.3). Note that

the striped pattern also accrued for the coherence spectrum as in the power spectrum when the correlation was windowed to compute the spectrum. This is because the part of the spectrum that is covered by the stripes is the one that showed a bimodality in the power spectrum. As a result, this part of the coherence would be more relevant since it can reveal important aspects of ρ_{hv} in mixed phases.

Like the power spectrum, one can window the samples instead of the correlations and see if it helps obtain a better estimate. Thus, when we apply a Blackman window to the samples and not to the autocorrelation, the following spectrum is obtained:

The coherence spectrum becomes a solid one for all the values. The reason is that the definition of coherence in (6.3). Intuitively, if the energy is preserved, then the unit is obtained from the quotient in the coherence equation in (6.3). Another way to see the coherence spectrum is as a measurement of how coherent the spectrum is over many realizations. As a result, some average is needed to allow some variation. On the other hand, if no average is performed, the coherence does not perceive any changes in the spectrum, and one is obtained from (6.3).

A window in the autocorrelation can provide an average in the spectrum to induce variation in the spectra and obtain coherence values different from one. For instance, a Blackman window has zeros at the end and the start of the window [67]. These zeros can be seen as a padded window, which has an averaging effect in the spectrum [67]. As a result, we can induce some variation in the spectrum and obtain some values in the coherence by creating some averaging using a window in the autocorrelation.

To have some reasonable values in the coherence, we need some averaging. The coherence tells how much variation one particular gate in the radar data has. The coherence can also be seen as how correlated two channels are over time. As a result, the average of the coherence and its normalization with the power of the signals needs to be averaged to obtain a measurement of how much fluctuation one channel has with respect to the other. As a result, using a window in the autocorrelation provides a padded window with zeros at the edges. These zeros serve as a window averaging in time, which produces averaging in the spectrum.

Mathematically, another way to see why a solid one is obtained when no averaging is done is by using the direct Fourier method to compute the spectrum. Using (6.3) and replacing the cross-correlation spectrum by the product of the horizontal and vertical power spectrum, it yields:

$$s\rho_{hv} = \left| \frac{C_{hv}(v)}{\sqrt{S_{hh}}(v)S_{vv}(v)} \right|$$

$$= \frac{|(F\{H(n)\})^* * F\{V(n)\}|}{\sqrt{F\{H(n)\} * F\{V(n)\}}} = 1 \tag{6.19}$$

A one is obtained from the last equation because the energy of the cross-spectrum is the same as the multiplication of the power spectrum of both channels. However, when the power and the cross spectra are averaged, the story is different. The reason is that the Blackman window has zeros at the end of the window; in another world, the window provides an average of two spectra in time. Suppose we have two spectra for the horizontal and the vertical channel. Let's analyze these spectra for a particular value in the Doppler velocity (v_o). At v_o, suppose the horizontal power spectrum has a value of X_1 for the first spectral estimate and X_2 for the second spectral estimate. Similarly, let's denote Y_1 and Y_2 to the first and the second spectral estimate at v_o for the vertical channel. In this case, if the spectra are averaged to obtain the coherence, we have:

$$s\rho_{hv} = \frac{|C_{hv}(v)|}{\sqrt{S_{hh}(v)S_{vv}(v)}}$$

$$= \frac{|X_1Y_1 + X_2Y_2|}{\sqrt{(|X_1| + |X_2|)(|Y_1| + |Y_2|)}} \tag{6.20}$$

Cauchy-Schwarz inequality in complex numbers guarantees that (6.20) is less than one.

The absolute value in the numerator of (6.20) starts deviating from the multiplication in the denominator. As a result, averaging is necessary for computing the coherence spectrum. Otherwise, a solid one would be obtained. The window outside the correlation can be used for averaging, and the window inside the autocorrelation can be used to reduce the effect of the sidelobes. When one uses these two windows to compute $s\rho_{hv}$, it yields the estimate shown in Fig. 6.9.

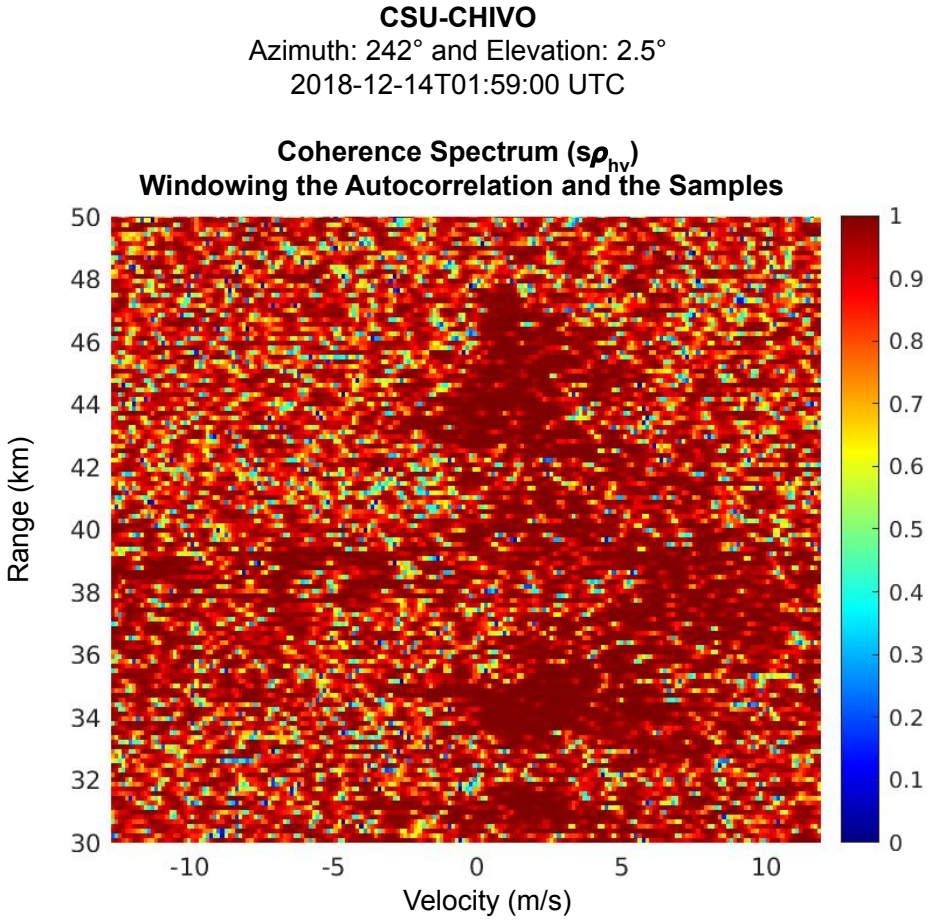

Figure 6.9: Coherence spectrum computed using Blackman window to multiply the autocorrelation and the samples

In Fig. 6.9, we can see $s\rho_{hv}$ showing values near one where the high energy of the spectrum was observed in Fig. 6.7. In this case, when a Blackman window was used to multiply the correlation, $s\rho_{hv}$ shows values different than one, assigning values near one where the high part of the energy is concentrated in the spectrum.

6.4.3 Spectral average, practical considerations

The average is an important process for the estimation of the spectrum. As can be seen, the average is necessary to obtain reasonable results in $s\rho_{hv}$. Averaging is also important to obtain a smoother spectrum in the spectral estimate and reduce the noise. In this part of the document, we explain two methods for averaging, one is averaging in time, and the other is averaging in frequency via the convolution properties. In addition, after the average is done, we also compute smooth filtering using Gaussian windows.

Time average

To compute Fig. 6.10, we use 64 out of the 99 samples to compute individual spectra. Hence, a sequence of 35 spectra was computed using a moving a rectangular window of L = 64 through the 99 samples. This method is also known as time-dependent Fourier analysis [67]. These 35 spectra were subsequently averaged to obtain the spectrum in Fig. 6.10. This average is done in linear units over the absolute values of the spectrum estimates.

In Fig. 6.11, a second component is now clearer to see in the negative velocities at 41 km in range. The shape and extension of this secondary component are easier to see. It can be seen that even a separation in the spectrum of this second component appears from 38 km in range and extends to 43 km. This second component is less prominent than the main component by around 30 dB.

Averaging with Gaussian filters along the range and velocity

The spectrum in Fig. 6.10 is smoothed out. One way to smooth the spectrum is by applying a circular convolution with an averaging window. A Gaussian moving window is used with $N = 5$ in

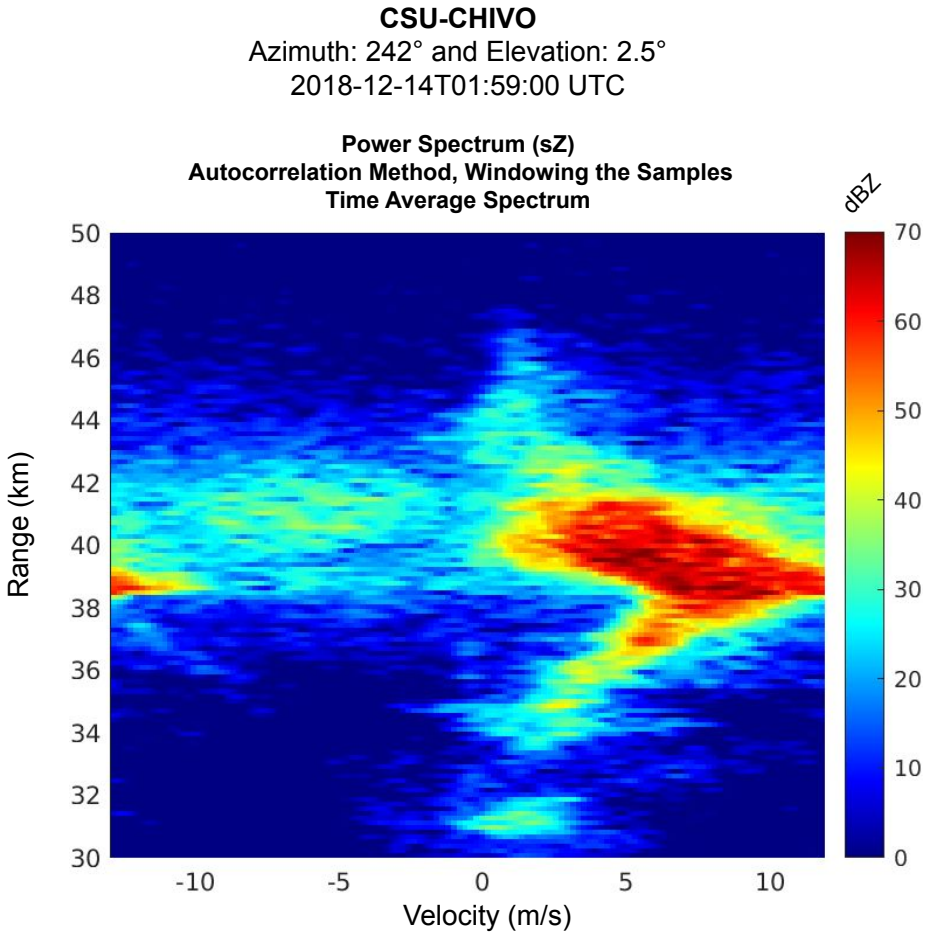

Figure 6.10: Power spectrum estimation after averaging spectrum over time using 64 samples

this case. This Gaussian window is convoluted with every gate along the velocity axis. A circular convolution is used to preserve the number of samples because the spectrum in the discrete Fourier domain has a periodic property.

Similarly, the spectrum is average along the range using a Gaussian window of length 5. This smooths the spectrum along the range to provide a better interpretation. In addition, the Gaussian windows provide a suitable shape for convolution along the range since more weight is given to the gates closer to the one being resolved.

In Fig. 6.11, it is possible to see that it looks more clear on the spectrum. In addition, the bimodality in the spectrum at around 41 km is clearer. This spectrum is constructed using the average time from the previous spectrum and a Gaussian window along the velocity and range. The

Gaussian window is selected instead of a rectangular window for the convolution and filter process because the Gaussian window provides more weight to the center point of the window. This is also why L = 5 lengths are chosen instead of 4 or 6 to have an odd number representing the center.

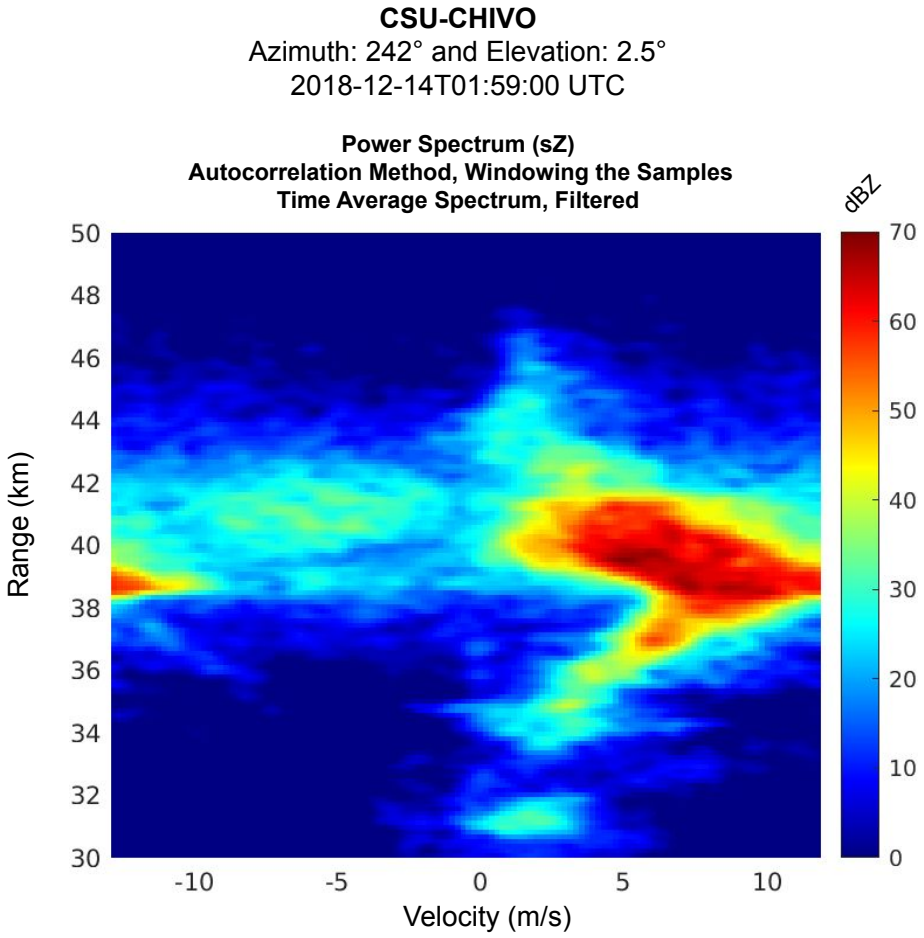

Figure 6.11: Power spectrum with time average of 64 samples and filtered with a Gaussian window of length five along the velocity and the range axis

The same process is done to compute the differential spectrum. The differential reflectivity spectrum is shown in Fig. 6.12:

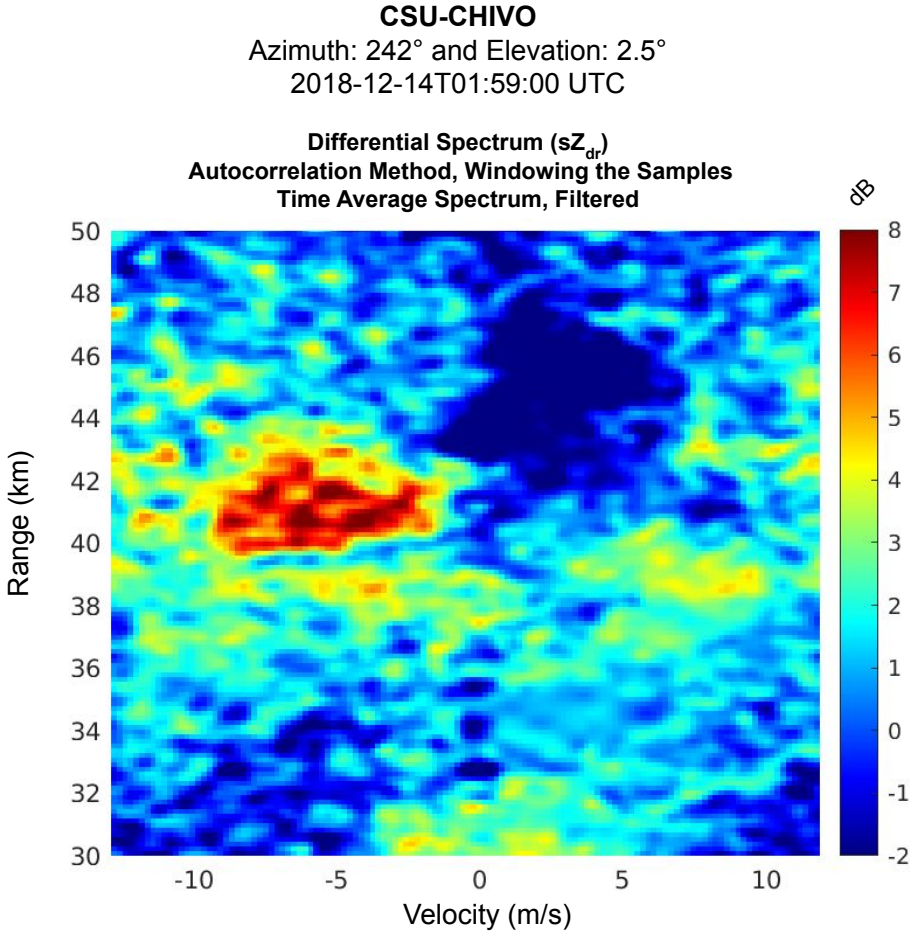

Figure 6.12: Differential reflectivity spectrum, using the same method as Fig. 6.11sρ_{hv}

The differential reflectivity spectrum is computed by taking the quotient between the horizontal and the power spectrum as described in (6.2). As in the power spectrum, a number of 64 samples is used to average a total of 99 samples. Then, a Gaussian filter along the range and the velocity axis is used to smooth out the spectrum.

It can be seen in this spectrum that the secondary lobe, which can be seen in the power spectrum, displays in the differential spectrum very high values, near 8 dB. This means this part of the spectrum displays signatures of melting ice.

$s\rho_{hv}$ Averaging and Windowing

For $s\rho_{hv}$, the same process is applied as in the power spectrum, however, with some differences. In this case, the cross-spectrum, horizontal, and vertical spectra are averaged separately in time. Then the coherence spectrum is computed by taking each of the averages of the spectrum and applying (6.3). One can also compute each of the coherence spectrums and then average the coherence spectrum directly. However, computing the average spectra first and then computing the coherence spectrum from the average spectra seems to provide better results.

The coherence spectrum after averaging in time is shown in Fig. 6.13. The spectrum is computed using the 64 samples and separately computing the cross-spectrum between the horizontal and the vertical channel and the horizontal spectrum and vertical spectrum. Then the coherence is computed based on (6.3).

It can be seen in Fig. 6.13 that the noise floor of the coherence spectrum reduces, and the values with high coherence are also clearer and easier to identify. A Blackman window is used to multiply the samples and the correlations to compute this spectrum.

We try different windows in the cross-spectrum and the power spectra to see if it produces a better result that lets us identify the areas with high and low coherence better.

In Fig. 6.14, we used different windows in the coherence equation. The Blackman window is used to compute the cross-correlation in the numerator part of the quotient of (6.3) The Hann window is used in the correlation of the H and V channel in the denominator in (6.3). These windows are used to multiply the samples. It can be seen that this combination of windows produces a lower

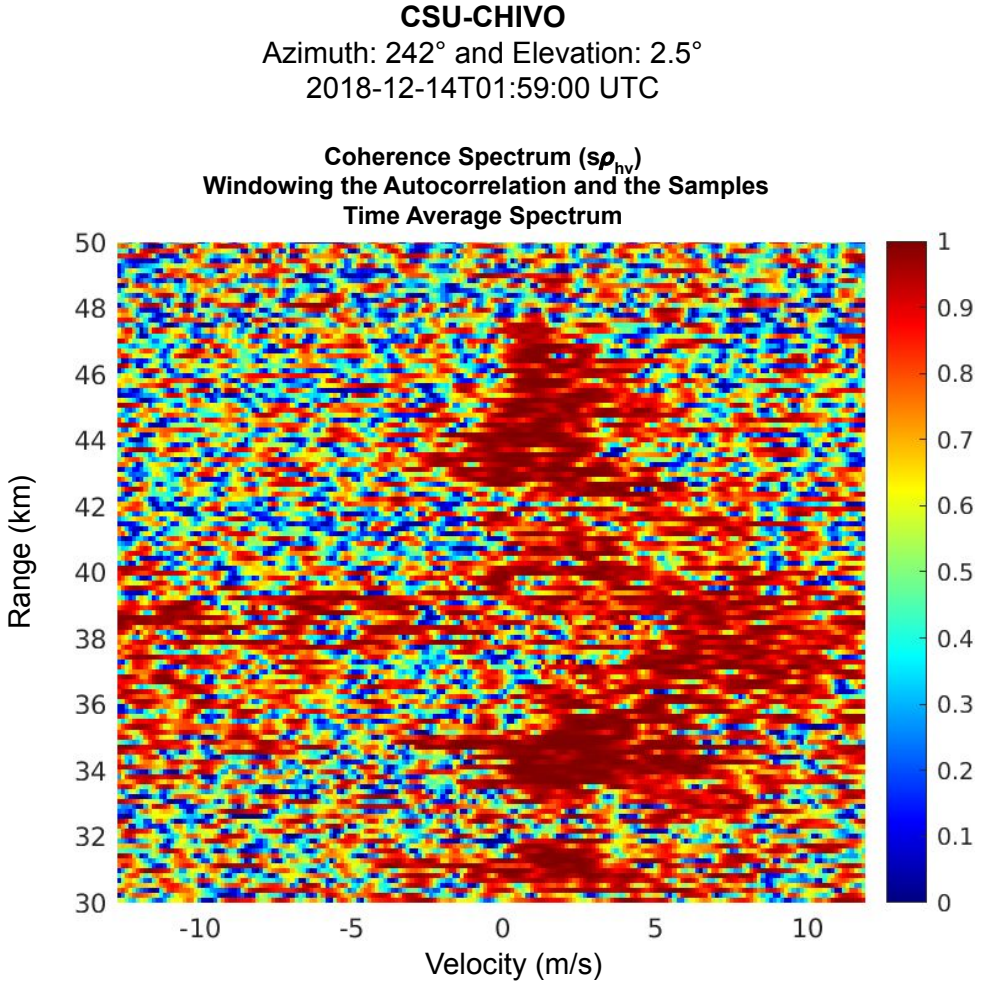

Figure 6.13: Coherence spectrum, windowing the autocorrelation and the samples, and doing spectrum averaging over 64 samples.

noise floor for the coherence spectrum in areas with low power. The Hann window is used because it is one of the closest to the rectangular window, and the Blackman is one of the farthest in terms of their properties.

Similarly to the power spectrum, the coherence spectrum is smoothed using a Gaussian filter along the velocity and the range axis. Fig. 6.15 shows the smoothed coherence spectrum.

A Gaussian window of length five is used to average along the velocity axis and the range. It can be seen that the signal with higher values corresponds to the values that show higher values in the power spectrum, and it is less spotty than using other techniques.

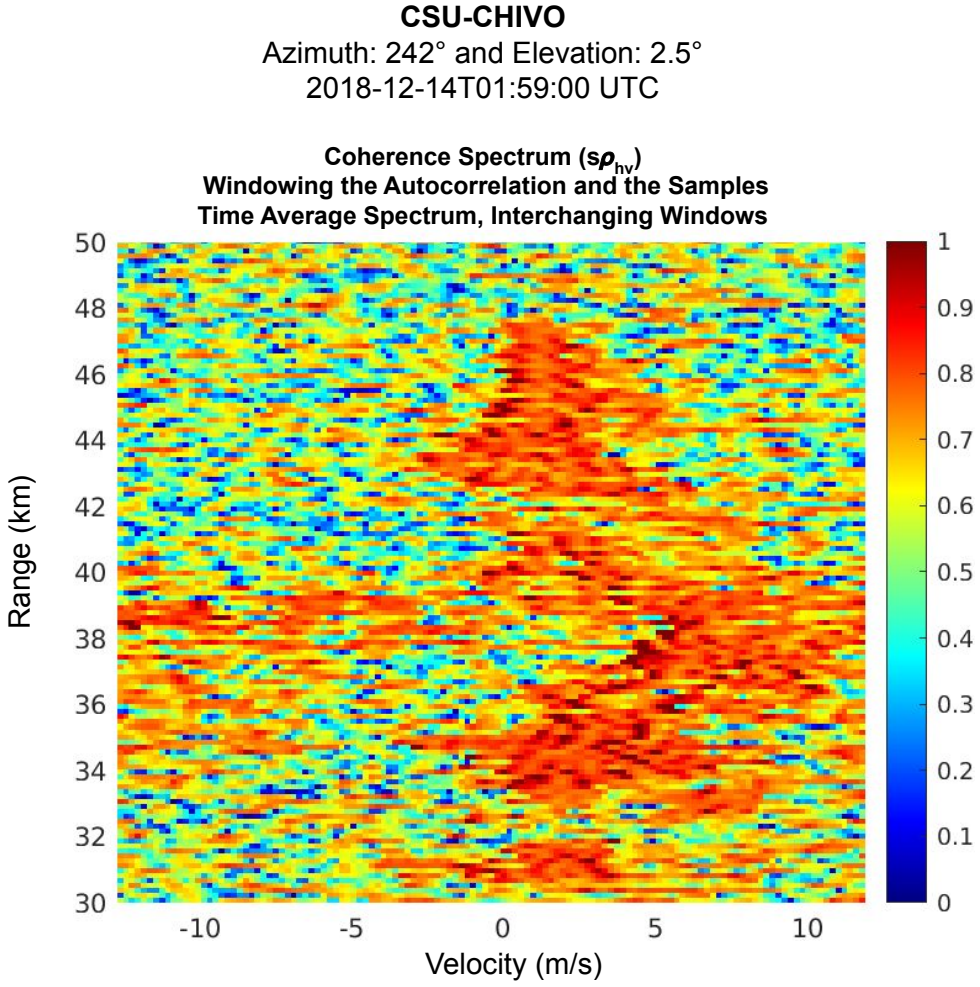

Figure 6.14: Coherence spectrum computed as Fig. 6.13, this time using a Blackman window for the coherence spectrum and a Hann window for the horizontal and the vertical spectra

6.4.4 Spectral decomposition of melting ice in an updraft environment

Spectral polarimetric decomposition is performed in the mix of phase regions resolved by HydroClass in the low elevations, as denoted in Fig.6.3. The polarimetric signatures in this region suggest the presence of rain and melting ice. HydroClass resolved a mixture of hail and rain around 38 km in range. The spectra in this region are analyzed to validate the mixture of phases and to get insight into the hail and rain distribution.

The spectral decomposition is computed from the I&Q data in the RHI shown in Fig. 6.1. The spectra are computed along the 2.5° elevation angle. The power spectrum (sZ), differential spectrum (sZ_{dr}), and coherence spectrum ($s\rho_h v$) corresponding to this elevation are shown in Fig.

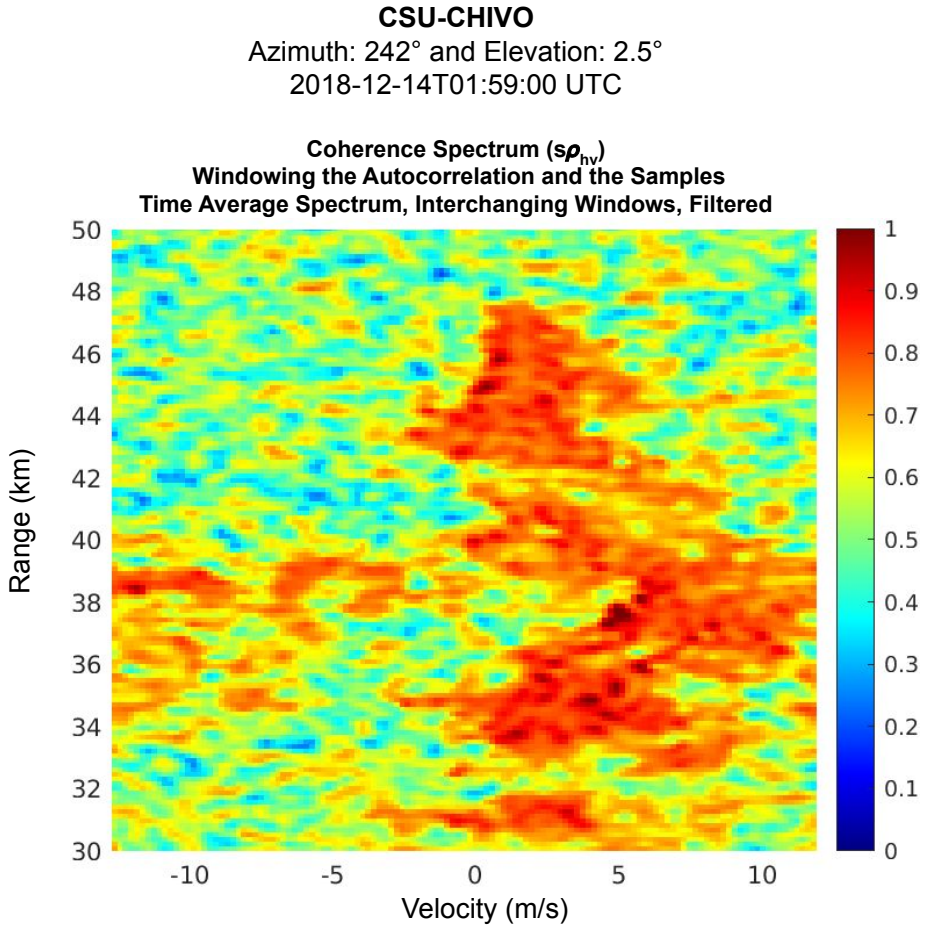

Figure 6.15: Coherence spectrum Filtered using a Gaussian filter. The coherence spectrum is computed as in Fig. 6.14

6.16. These spectra are computed by averaging, windowing, and smoothing techniques mentioned in the previous sections.

As mentioned before, the power spectrum represents the reflectivity decomposition along the radial Doppler velocities spectrum. Similarly, the differential and the coherence spectra represent the Z_{dr} and the hv decomposition in the Doppler velocity spectrum. IQ data from the RHI are used because they provide a bigger number of samples per degree than a PPI. These more samples allow us to perform spectral averaging to obtain more detailed spectrum estimates.

As can be seen in Fig. 6.16, the spectral decomposition shows two distinct signatures in the positive and negative velocities from 38 to 42 km in range, collocated with the region with melting ice. This portion of the spectrum coincides with the mix phase inferred by HydroClass. The power

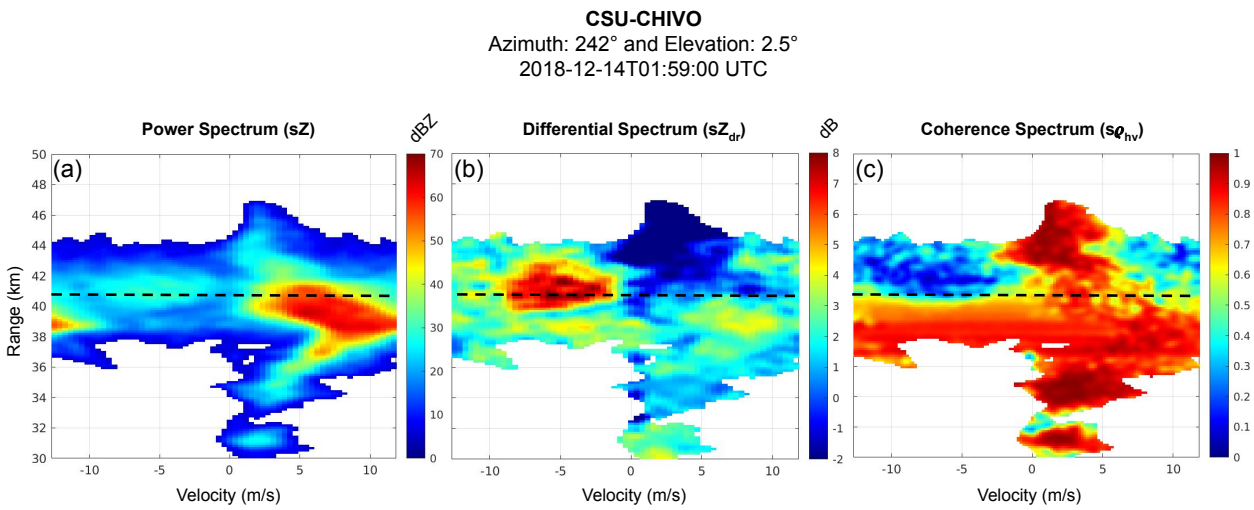

Figure 6.16: Spectral decomposition from CHIVO dual polarimetric measurements along the 2.5° elevation. Power spectrum (a), differential spectrum (b), and coherence spectrum (c).

spectrum shown in Fig. 6.16(a) displays a bimodality from 38 to 42 km in range. The main part of the energy is concentrated in the positive velocities. The positive part of the spectrum also displays a moderate differential return and a high coherence. On the other hand, a secondary component is observed in the negative velocities. A spike in the differential spectrum and low coherence are observed in the negative part of the spectrum.

Fig. 6.17 shows the values of the spectrum at 40.5 km in range. It is evident that the power spectrum displays a bimodality, one main component at around 5 m/s and a secondary at -5 m/s. The difference between the main and the secondary component of the power spectrum is about 30 dB. The main part of the spectrum displays a differential return of about 2 dB and a coherency near 0.8. These signatures are associated with rain. The secondary part of the spectrum shows high values in the differential spectrum near 8 dB and low coherence near 0.2. These signatures in the spectrum are associated with melting ice.

6.5 Discussion

Estimating the dual-polarimetric spectrum can be challenging, especially in updraft environments. In updraft environments, turbulence and inflows' convergence can broaden the spectrum, making it hard to distinguish noise from weather signals. In addition, the noise floor also tends

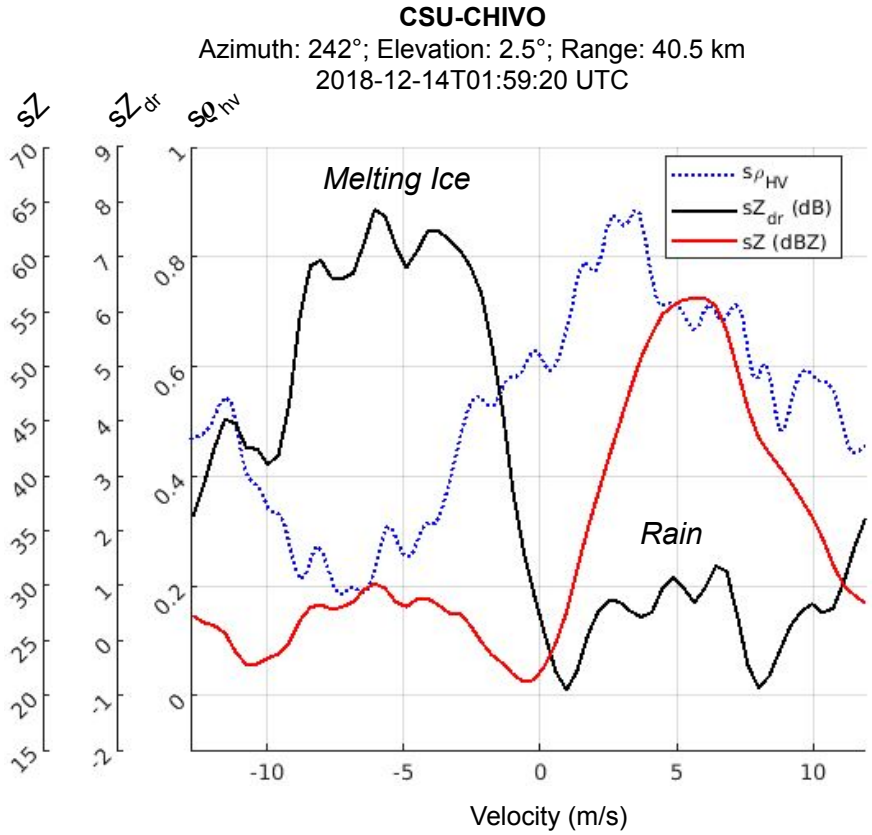

Figure 6.17: Spectral decomposition of the dual polarimetric measurements from CSU-CHIVO radar at 40.5 km in range, 2.5° in elevation, and azimuth 242°. Power spectrum (sZ) is shown in red; the differential spectrum (sZ_{dr}) is shown in black, and the coherence spectrum (ρ_{hv}) in dotted blue.

to increase in this kind of environment, making it more challenging to read and understand the spectrum.

This chapter explores different techniques to estimate the spectrum in updraft environments. These techniques are discussed, and the findings from applying them are analyzed. The advantage of using two methods to compute the spectrum differently is also discussed. In addition, the signal processing performed in terms of averaging, windowing, and filtering the spectrum in updraft environments is also explained. This signal processing allows us to obtain a clear spectrum and reduce the noise floor. The expansion in the spectrum of the dual polarimetric variables allows us to better understand the microphysics in updraft environments, which will be explained and discussed at the end of this section.

6.5.1 Lessons learned by computing the spectrum via the autocorrelation and the Fourier transform

To understand important aspects of the spectrum in updraft environments, the dual-polarimetric spectra were computed in two different ways. The first way was by using the autocorrelation of the I&Q samples, while the other method applied the Fourier transform directly to the samples. By computing the spectrum in these two ways, we could exploit the duality between the multiplication and convolution in time and frequency of the Fourier transform. This approach revealed various important aspects of windowing the spectrum, properties of the Fourier transform, convolution, and correlation.

One of the lessons we learned from computing the spectrum in different ways was that windowing the autocorrelation in the power spectrum was not enough. A striped pattern that appears needs to be removed to better observe the part of the spectrum that crosses the updraft, especially when the spectrum starts to broaden. This part of the spectrum was when we started observing a mixed phase in HydroClass. Therefore, resolving the spectrum better in this part is more important. Computing the spectrum using the direct Fourier transform also helped us to understand the importance of windowing the samples in the correlation method.

The direct Fourier transform method was very useful in understanding an important aspect of the spectrum that helps us to suppress noise in updraft environments. This method was also useful for intuitively analyzing the coherence spectrum using an average of two spectra. This way, we could understand why the average is important in the coherence computation. In addition, we could mathematically see why the coherence expression gave us a unit value when no average was performed.

In conclusion, computing the spectrum in two ways reveals important aspects of spectrum properties that can be used to obtain a better spectrum in broad and updraft environments.

The importance of windowing the samples to reduce the noise floor

Windowing the samples helps suppress sidelobes interference when the spectrum has bimodalities. As a result, windowing the samples helps reduce the striped pattern observed in Fig. 6.4. In this figure, only the correlation is windowed. When only the autocorrelation is windowed, the spectrum in Fig. 6.4 looks very similar to the spectrum using the direct Fourier method with a rectangular window in Fig.6.7. The reason why windowing the sample was suggested was that in the direct Fourier transform method, the window is applied directly to the samples, and subsequently the Fourier transform is applied. Thus, this pattern suggests that windowing the samples will help to reduce the striped pattern in the spectrum of Fig. 6.4. The reason windowing the samples helps to mitigate the striped pattern effect is that the samples are initially multiplied by a rectangular window. This effect propagates through the convolution that is performed through the autocorrelation.

This is not the first time this striped pattern has been observed in the spectrum. Other authors have also obtained striped patterns in the spectrum with high noise floors [68]. This author attributed the striped patterns to spectrum leakages of the energy due to an interference signal by other sources. In [68], a striped pattern was found when seeing clutter mixed with the weather. This explains why these stripes tend to appear when there are bimodalities or turbulence or more than one source in the spectrum. The noise floor increases, and the sidelobes from the window in the autocorrelation spread this energy across the spectrum.

Selection of the windows

A Blackman window is used to multiply the samples because, from the common windows, it provides one of the best signals to sidelobe suppression, and its wide main lobe helps to smooth the spectrum. Although the window that produces the narrower main lobe width is rectangular, the sidelobes are significantly high, producing the striped pattern in Fig. 6.7. The Blackman window, on the contrary, provides a good sidelobe suppression and its wider main lobe helps to average some of the fluctuations that naturally occurred when more samples are used to estimate the spectrum.

Coherence ($s\rho_{hv}$) and the importance of averaging

The averaging process is necessary to compute $s\rho_{hv}$. If no averaging is performed, a solid one is obtained. The reason is that the energy in the numerator and denominator in (6.3) is the same, and the unit is obtained.

The zeros in the Blackman window serve as an averaging window in time. The numerator and denominator in (6.3) start deviating, as can be seen in (6.20) when averaging is performed. On average, values near one are shown when the vertical and the horizontal channel are more correlated and lower values when these channels are less correlated. As a result, using averaging would let us better estimate the coherence. Coherence is a measurement of an average of the coherent the two channels are. As a result, the correlation window can be used to average in time and obtain a representation of how coherent this average is.

In addition, using a combination of different windows help to reduce the noise floor and obtain a better coherence estimate. The use of a Blackman window to multiply the vertical and the horizontal power spectrum in the denominator of (6.3) and a Hann window in the numerator to multiply the cross-channel spectrum reduces the noise floor more efficiently in the computation of the coherence.

In conclusion, a window to multiply the samples and a window that multiplies the correlations and cross-correlations are needed to compute the coherence spectrum. The window that multiplies the samples helps mitigate the striped effect observed in Fig. 4.5. On the other hand, the window that multiplies the correlations helps to obtain the average needed to obtain values different from ones.

Averaging in time

The averaging in time helps produce a better spectrum view in updraft environments. For example, the main and the secondary component in the mix phase region is clearer after averaging in time is done in Fig. 6.10. It can be seen that the average helps reduce the noise. In addition, the variation in the spectrum is average (Fig. 6.10) is less than when all the samples are used to

compute the spectrum in Fig. 6.7. The average in time also helps to see more precisely where the locations of the main and secondary lobe in the mix phase region are.

In this case, the averaging of many spectra is possible because the spectrum estimates are still coherent over a short period. The samples that are used to obtain the spectrum estimates can be seen as a realization of the same process. The reason is that the time between one sample and the other is very short. The power spectrum is an estimation of the PSD of the signal. The short time that passes between the first and the last spectrum is very small due to the small delta in degrees that the pointing angle of the radar changes, which is only 0.2 deg, providing enough coherence in the data to compute this set of the spectrum.

The effect of averaging in time can also be obtained by using a padded with zeros window to multiply the autocorrelation. This process helps in a computational way since one can obtain similar results as in the time average using a window that moves in time. In this case, we choose to do the average using 64 samples.

6.5.2 Microphysical analysis

The spectral processing discussed before allows us to obtain a clean spectrum to analyze the microphysics of particles in an updraft environment. The polarimetric spectrum can be seen as expanding the radar variables in the spectrum domain. In this sense, it is possible to identify how the particles disperse in the Doppler spectrum when a clean spectrum with a low noise floor is estimated.

Spectral analysis from the IQ data was performed in the region where HydroClass resolved a mix of phases. The polarimetric spectral decomposition for this region is shown in Figs. 6.16 and 6.17. It can be seen in these figures that the Doppler spectrum displays a bimodality. This bimodality confirms a mix of phases. The spectrum shows two kinds of particles moving at different velocities.

Moreover, one spectrum component displays rain signatures, and the other displays a melting ice signature. In addition, the rain component broadened near the mix phase. This broad spectrum

could be due to the different sizes of drops that the melting ice generates along its way in the updraft. The spectrum component that displays the signature of melting ice is significantly lower in power return than the one from rain. Nevertheless, these components dominate the polarimetric returns and the attenuation.

6.6 Summary

6.6.1 Summary

The dual-polarimetric spectral decomposition is a powerful tool for studying microphysics in updraft environments. However, computing polarimetric spectra in this environment is challenging due to the turbulence, mixed phases, and high noise the estimates can experience. In this chapter, we explored digital signal techniques that enhanced the quality of the spectrum estimates in an updraft environment. In addition, the microphysics of a case where a convergence of inflows occurred is studied. Some of the key points of this chapter are summarized:

1. Windowing the autocorrelation is not enough to estimate the spectrum in updraft environments.

2. Windowing the autocorrelation can be used to average the spectrum in time in a very efficient way.

3. Windowing the samples is also necessary before performing the autocorrelation to estimate the spectrum in updraft environments. Windowing the samples helps reduce the noise floor in estimating the spectrum.

4. Averaging in time is necessary to estimate the coherence spectrum. Otherwise, a value of one is obtained when computing the coherence.

5. Using a combination of windows in the numerator and denominator of the coherence spectrum can help reduce the noise floor.

6. Dual polarimetric spectral decomposition reveals how the spectrum is dispersed in the mixing phase region where updrafts converge occurs.

The importance of this chapter is that it can be useful as a guide to computing polarimetric spectral decomposition in regions with turbulence, mix-phace, and updraft environments, where the spectrum becomes challenging to be computed because of the increase in the noise floor. In addition, the polarimetric spectral decomposition in an identified updraft reveals the polarimetric signatures of a mixed-phase region. The spectral decomposition in this region has a huge potential to unveil the composition of updrafts and to study their morphology and evolution.

6.6.2 Future work

As can be seen, the polarimetric spectral can provide a big insight into the mixing ratio of updraft environments. For example, the 30 dB difference between the rain and hail part of the spectrum in Fig. 6.17 indicates that the power return from the melting ice is three orders of magnitudes lower than the power return from rain. These values in reflectivity do not necessarily mean that the values of melting ice are 30 dBZ. Instead, it means that the energy return from this concentration of ice particles in the volume is 30 dB less than the rain.

The combination of mixing ratios that can produce these returns in the spectrum needs to be simulated. However, scattering simulations of updraft are challenging because the interaction of the particles needs to be represented, as also how these particles interact individually electromagnetically. As a result, it is suggested as future work to simulate the spectral decomposition of the updraft environment. This work would be significant for obtaining mixing ratios of updraft using observations.

As another future work, we want to include other spectral decomposition estimates such as $\phi_d p$ and SQI. We also want to explore how the direct Fourier transform can help to understand and better estimate these dual polarimetric decompositions. In addition, the properties of the cross-spectrum using the multiplication properties would be explored. Other future work includes:

1. Simulations of dual polarimetric spectral spectra in updraft environments to obtain mixing ratios from observed updrafts

2. Estimation of other dual polarimetric spectral decompositions such us SQI and $\phi_d p$ decompositions and the direct Fourier method

3. Analysis of more updraft during RELAMPAGO

4. Analysis of updraft trajectories and how the spectral changes

Chapter 7

Insights from comparing multiple radar observations with convective-permitting high-resolution simulations

7.1 Introduction

Numerical simulations are often challenged to represent the convective distribution and intensity in South America. Limited atmospheric observations in South America prevent a better understanding of processes leading to and sustaining heavy rainfall in these regions. Furthermore, the poor representation of convective processes in the global South leads to poor performance of models in these regions, affecting models' ability to predict the weather globally. The radar network from the RELAMPAGO [58] campaign provides an unprecedented dataset to study the evolution of the storms in this region of Argentina and to evaluate how well models represent convective-scale processes observed by radars.

In this study, multiple radar observations were compared with numerical high-resolution simulations. The insights from this comparison are shown in this chapter. These simulations are compared with radar observations to understand the difference and similarities between the observed and simulated storms. A representative case during the RELAMPAGO field campaign is simulated using different configurations of the Weather Research & Forecasting Model (WRF). These configurations included different spin-up times, microphysics schemes, and resolutions. The model and radar comparison is conducted to see the ability of the different configurations to represent the radar observations.

7.2 Data and Methods

The December 14, 2018, case from the RELAMPAGO field campaign is used for this study. The December 14, 2018, case was used because it produced a significant amount of rain and hail near the SdC. The storms for this case were well captured by the network of C-band radar deployed in the RELAMPAGO domain. Numerical simulations from this case also well captured the structure and the extension of the storm observed by satellite in a synoptic scale [69]. The radar observations are used to evaluate how the models resolve finer scale processes for this case.

7.2.1 Radar observations and retrieval

The radars that are used in this study are the CSU-CHIVO, the CSAPR-2 radar, and the RMA radar. The observations from 1 UTC to 8 UTC were used on December 14, 2018. The reason is that the weather started occurring at this time in the East side of the Sierra, where the radar coverage is. The radar data from this case is calibrated according to [55]. Attenuation and bias correction is performed to the reflectivity in addition to a second trip suppression. The rain estimates from these radars are computed using DROPS 2.0 [70]. This software uses a combination of rain relations to compute the rain estimates. The rain estimation from CHIVO, CSAPR, and RMA radars is merged using a masked average. Blockage from each of the radars is removed. In addition, the radar data is converted into cartesian coordinates. Then the max. reflectivity is computed over the column. For rain estimates, the 1 km CAPPI is used.

7.2.2 Numerical Weather Simulations of the Dec. 13-14, 2018 case

The Dec. 13-14, 2018, was simulated using the WRF model. These simulations were conducted using CONUS configuration over the RELAMPAGO domain with nesting subdomains of 27, 9, 3, and 1 km resolutions. Fig. 7.1 shows the domain for this simulation:

Precipitation in the Eastside of the SdC was captured by the radars from 00 UTC on Dec. 14, 2018. As a result, different spin-up times from 00 UTC were used. In the next table, the different

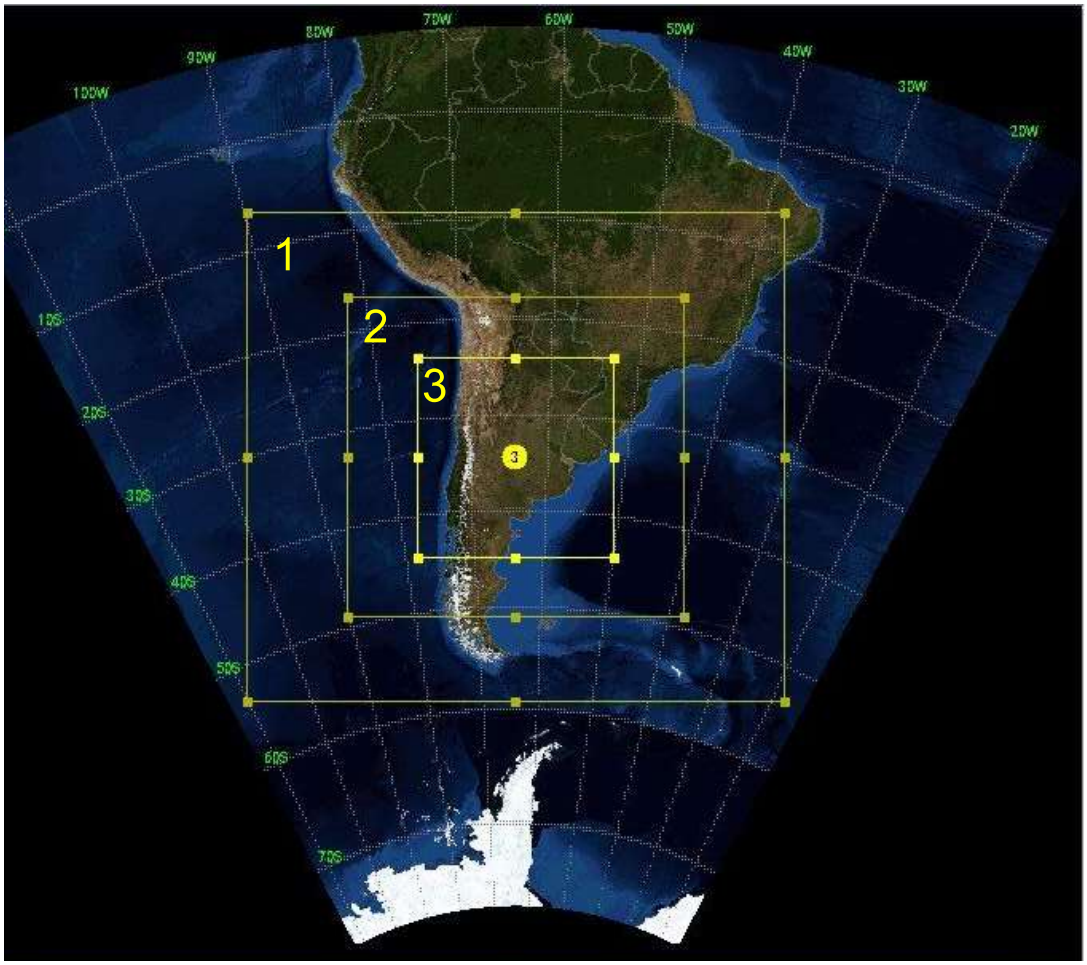

Figure 7.1: Domain of the WRF simulations

configurations of WRF are presented. These configurations were used to obtain a sensitivity test for the spin-up time, the resolution and microphysics scheme.

Table 7.1: WRF configuration for the different simulations

Characteristic	Parameter
WRF version	4
Boundury and initial condition	ERA 5
Configuration	CONUS
Domain 1, 2, 3, 4 resolutions	27, 9, 3, 1 km
Microphyiscs	Thompson aerosol [71], NSSL [72], Morrison [73]
Spin-up time from 00 UTC Dec. 14, 2018	24, 12, 6 hours

7.3 Results

7.3.1 Radar observations of the Dec. 14, 2018 case

The radar observations for the Dec. 14, 2018, case are presented. The CHIVO radar reflectivity is used in this analysis. The max. reflectivity is computed over the vertical column of the CHIVO radar. The data from the CHIVO radar is converted into the cartesian grid. Subsequently, the max. reflectivity over the column is computed. The sequences of figures shown in Figs. 7.2 shows the initiation of convection near the CHIVO radar domain.

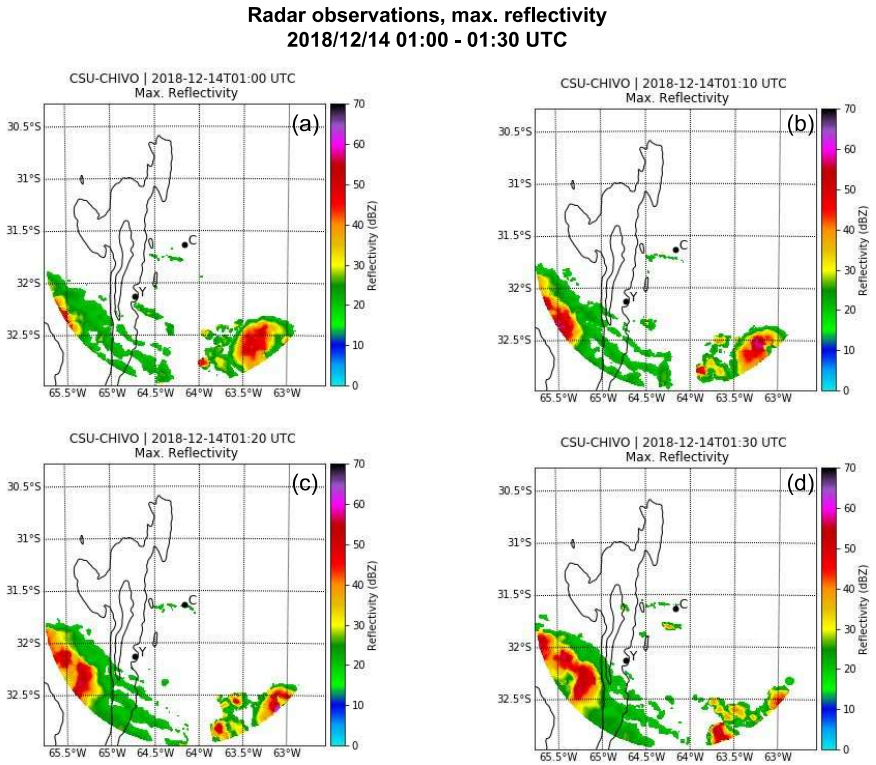

Figure 7.2: Max. reflectivity from CSU-CHIVO radar from 1:00 UTC to 1:30 UTC before the convection initiation (CI) starts in the East slope of the SdC.

As can be seen in Fig. 7.2, a boundary was moving North toward the CHIVO radar domain. The source of this boundary could have been from the outflow of the system passing by the South of the SdC. These systems can be seen in radar scope to the Southwest and Southeast of the CHIVO domain. The cold pool from the outflows of the storms South of the CHIVO domain seemed to

provide the lifting mechanisms necessary to initiate convection in the East slope of the terrain. As seen in Fig. 7.2(d), after the boundary interacted with the terrain, the convection initiated near the CHIVO domain. The convective initiation (CI) continues in Fig. 7.3.

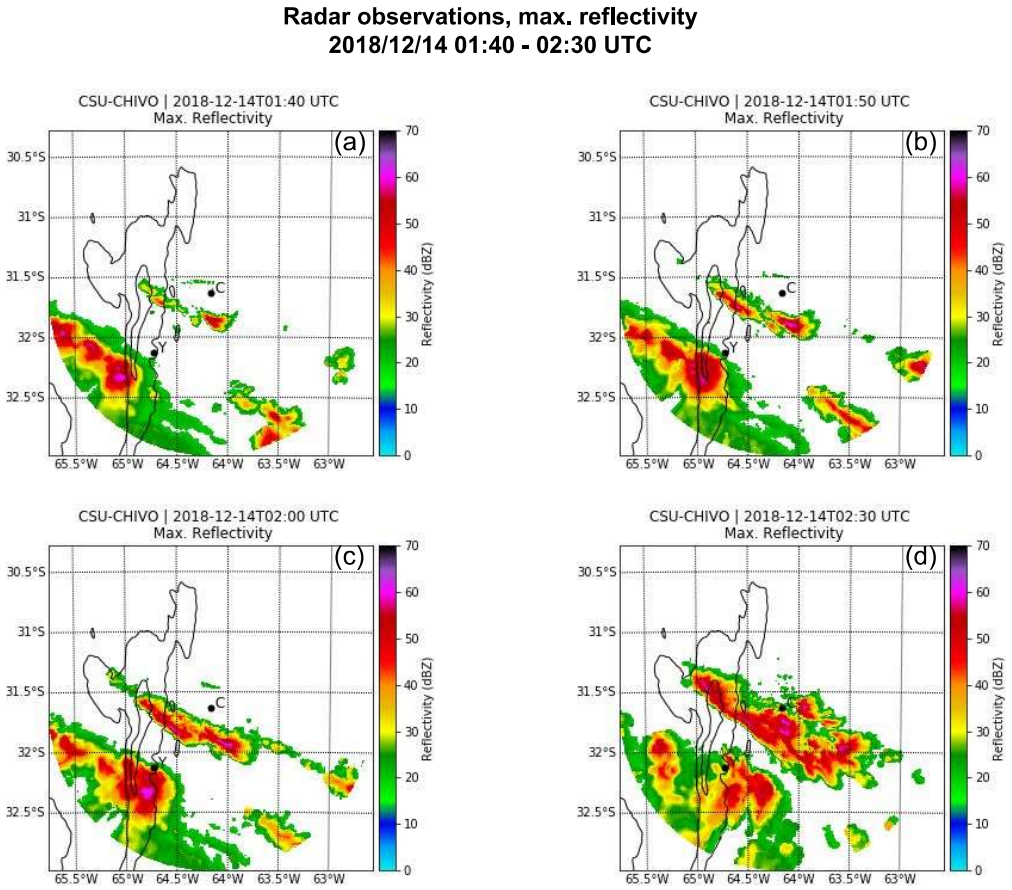

Figure 7.3: Max. reflectivity from CHIVO radar from 1:40 to 2:30 UTC after the boundary pass and the convective initiation starts in the terrain.

In Fig. 7.3, it is possible to see that after the boundary passed by the CHIVO radar domain, the new cells that initiated grew considerably fast, forming a convective line near the radar. Just one hour passed from the time that the initiation was observed by the radar in Fig. 7.2(d) to the time when the squall line was mature and even bigger than the initial system approaching the SdC from the Andes.

After the boundary interacted with the East slope of the sierras providing the lifting mechanism to initiate convection, new cells started on the East side of the Sierras, these cells evolved rapidly, producing a squall line as seen in Fig. 7.3. This squall line also produced outflows that, with the interaction with the terrain, generated new initiation, as seen in Fig. 7.4.

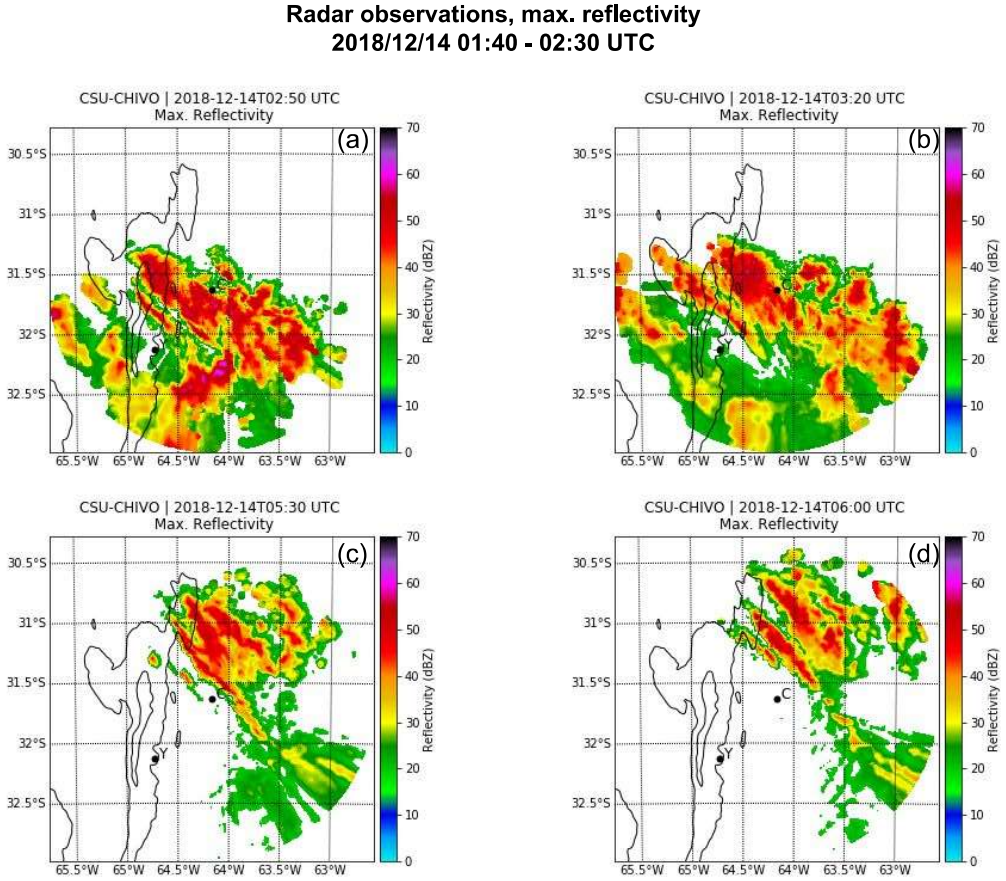

Figure 7.4: Max. reflectivity from CHIVO radar from 2:50 to 6:00 UTC. These different times illustrate how the back-building pattern occurs during this case.

Fig. 7.4 shows how new convection initiated in the East slope of the terrain after the main squall line formed in Fig. 7.3. As shown in Fig. 7.4(a), the main system near the CHIVO radar seemed to generate new convection. New convection originated in the East side of the SdC and organized into a convective line. This new convection grew fast, as seen in Fig. 7.4(b), producing

a secondary convective line in a short time. This same pattern of new convective lines forming in the East slope of the SdC was observed for this case until 6 UTC, as can be seen in Figs. 7.4 (c) and (d).

This train of the convective line passed by the same location producing more precipitation every time a new convective line originates in the east slope of the Sierras. This train of cells produced the significant rain observed in this case. The new cells do not grow as fast and vigorously as the first one, probably because the atmosphere stabilizes every time a new convective line forms.

In summary, the radar observed a boundary that initiated the convection in the East slope of the Sierras. This convection grew very fast, organizing in a convective line. Subsequently, more convective lines were formed in the east slope of the SdC, forming a train of convective lines moving East that later merged into a large-scale system. The interaction of cold pools from the older convective lines with the East slopes of the SdC produced the CI. This train of cells produced significant rain that generated floods in the East part of the SdC.

7.3.2 WRF Simulations of the Dec. 14, 2018, case

Simulations using the WRF model are carried out for the Dec. 14 case. These simulations were conducted using the CONUS and Thompson aerosol-aware microphysics configurations over the RELAMPAGO domain with a nesting subdomain of 27, 9, and 3 resolutions. In this part of the document, we show how this configuration, which produced a good representation of the storms in this region in Argentina [74], resolves the convection observed for this case. The figures that are shown in this section are from the 3 km resolution simulations.

The evolution of the model simulations is studied when the simulated system is close to the radar domain. We conducted comparisons with radar observations to see if the models accurately represent what happens near the SdC because this region is known for having severe weather and rapid upscale growth. So it is of special interest to see how the models resolve the initiation and upscale growth in the East part of the SdC. In addition, this case displays some of the most

characteristic convective features in this region of Argentina that lead to severe weather and upscale growth.

Figs. 7.5-7.8 show the evolution of the studied storm system. It can be seen in these figures that the model resolved mostly one convective system crossing the SdC and growing bigger. Instead, the radar observed multiple convective lines originating in the East slope of the SdC and merging, creating a bigger system. From the radar, it could be seen in Figs. 7.4 that multiple convective lines originated in the East slope of the SdC. From the model, the storm system seems to move across the SdC growing bigger while advancing, as can be seen in Fig. 7.5 and 7.6.

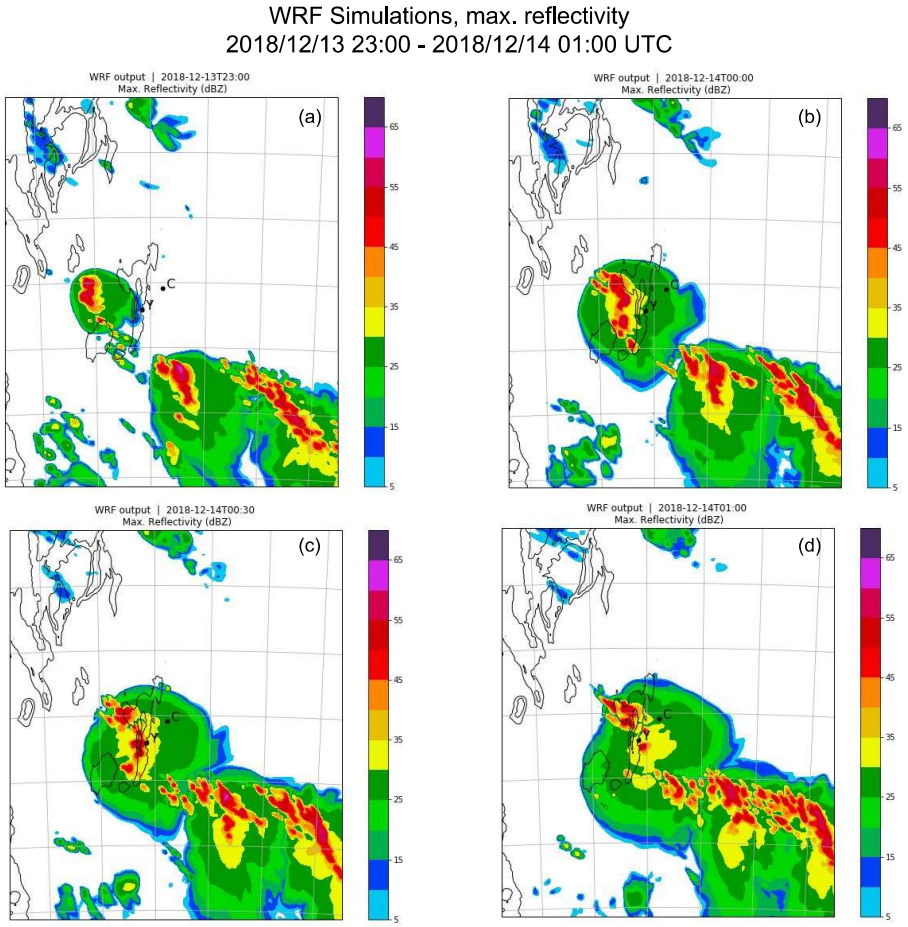

Figure 7.5: Max. reflectivity from WRF simulations from 23:00 UTC to 01:00 UTC.

Fig. 7.5 shows a sequence of max. reflectivity from the 3 km simulation when the convective system approached the SdC from the Andes. As can be seen in Figs. 7.5 (a) and (b), the model simulations placed convection on the westside of the SdC moving East from the Andes, as satellite observations also showed [69]. The cell splits into two, one moving North and the other one moving South, as seen in Fig. 7.5 (c). The North cell seems to initiate new convection to its West while approaching the SdC, as seen in Fig. 7.5(b). The South cell seems to cross the SdC, as can be seen in Fig. 7.5 (c) and (d), instead of passing by the South of the SdC as was observed by the radar.

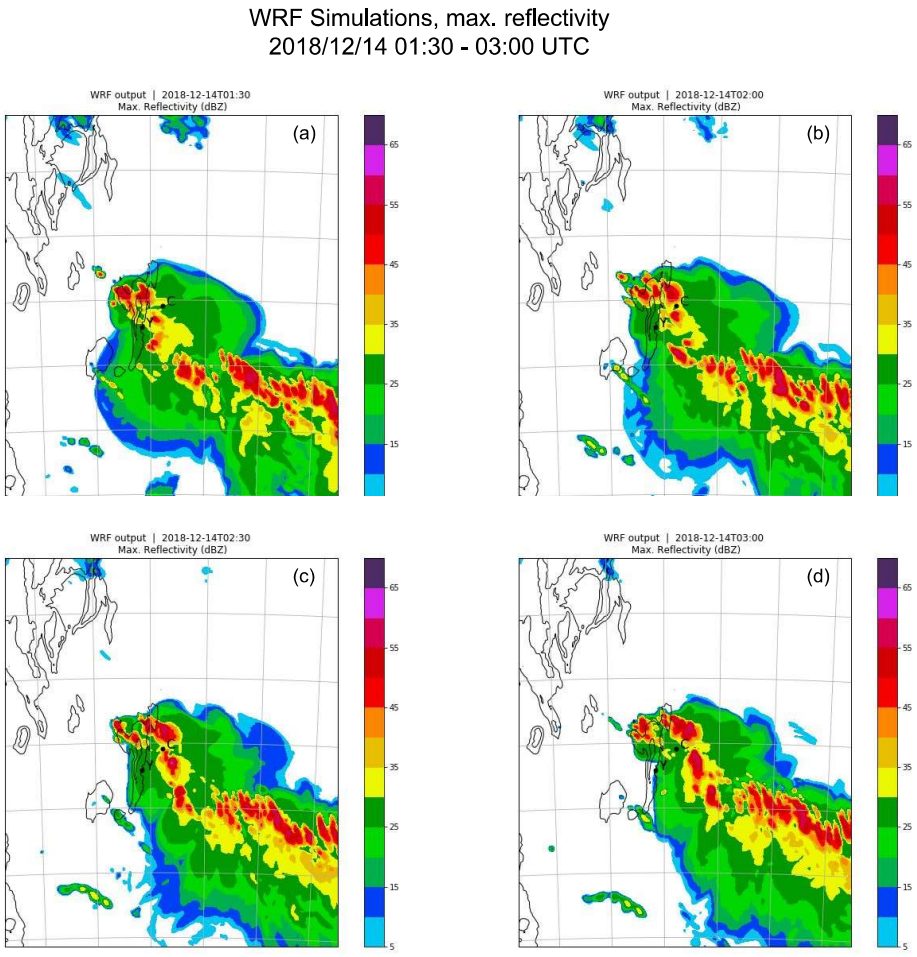

Figure 7.6: Max. reflectivity from WRF simulations from 01:30 UTC to 03:00 UTC

Fig. 7.6 shows the 3 km simulation when the convective system crosses the SdC. As can be seen in this sequence of figures, the North cell initiates more convection on the West side of the sierras, as can be seen in Fig. 7.6 (a) and (b). In addition, it can be seen in Fig. 7.6 (c) that the train of cells observed in the North part of the SdC is from the initiation that the North cell produces while approaching the terrain from the West. These new cells are not a product of initiation in the East slope of the SdC. The North and the South cells seem to initiate new convection in the East slope of the Sierras can be seen in Fig. 7.6 (d).

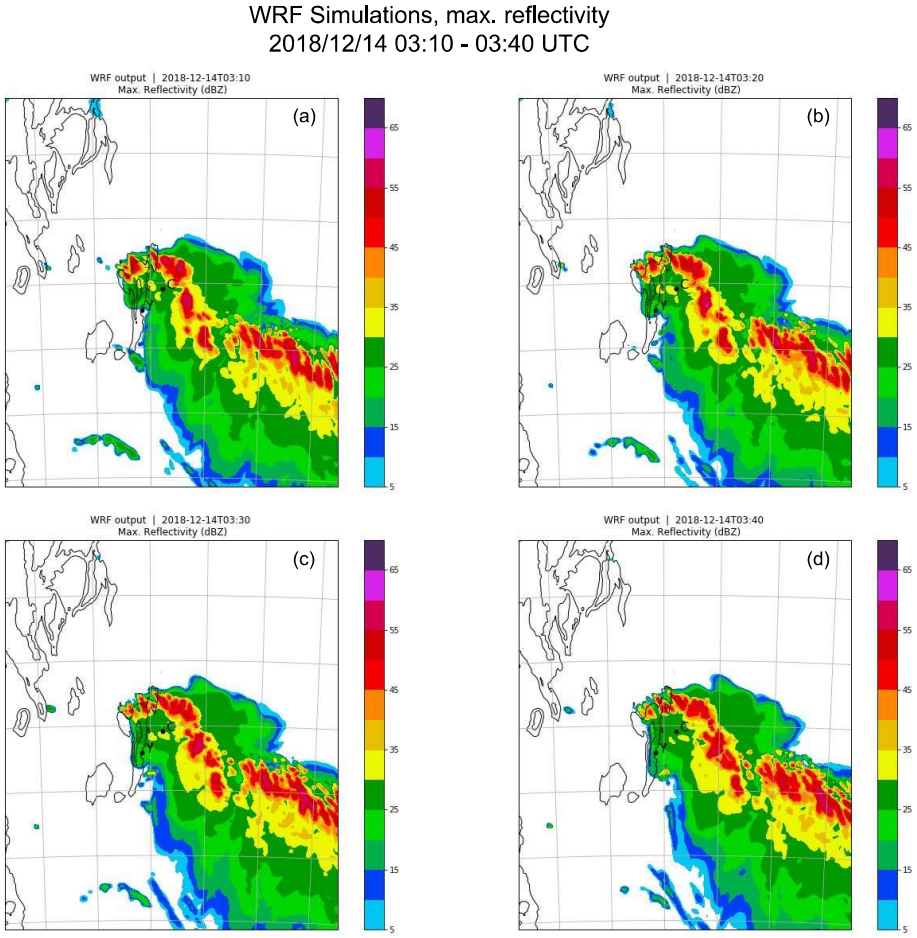

Figure 7.7: Max. reflectivity from WRF simulations from 03:10 UTC to 03:40 UTC

Fig. 7.7 shows the 3 km simulations when the convective system was located on the Eastside of the SdC. The purpose of this figure is to illustrate that new convective cells seem to initiate in

the Eastern slope of the SdC; however, the new cells do not develop into convective lines as was observed by the radar. New convective cells originate from this convective line near the terrain, as can be seen in Fig. 7.7 (a) and (b). However, as can be seen in Fig. 7.7 (c) and (d), these new cells do not grow as was observed for the radar in Fig. 4. The North and South cells seem to merge on the East side of the SdC, forming a large-scale convective line, as seen in Fig. 7.7.

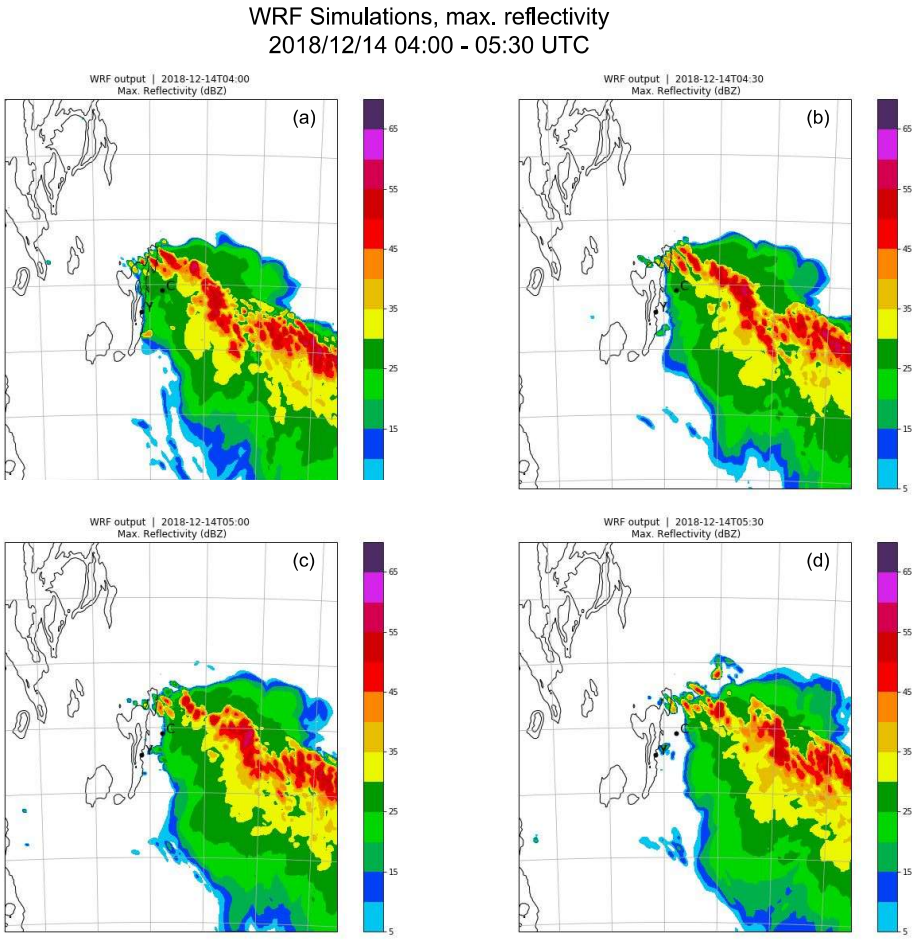

Figure 7.8: Max. reflectivity from WRF simulations from 04:00 UTC to 05:30 UTC

As seen from Fig. 7.8, more convection seems to initiate near the East slope of the terrain to the South of the SdC. However, they do not grow as was observed by the radar. The new convective cells seem not to have enough conditions to grow and form new convective lines. Instead, a main system seems to propagate East of the Sierras. The train of cells observed to the North of the SdC

is a product of the back-building occurring in the West part of the Sierras, as can be seen in Fig. 7.8 (a) and (b).

In summary, model simulations resolved for this case, a convective system passing by the SdC. This convective system was growing bigger but did not produce new initiation while moving East of the SdC. On the other hand, the radar observed a different pattern, as described in the previous section. As a result, a sensitivity test is conducted to evaluate how different models' configurations represent the features observed by the radar for this case.

7.3.3 Comparison of model simulations and radar observations for the Dec. 14, 2018, case

A series of sensitivity tests are conducted to see which model configuration better represents the precipitation near the radar domain. For this sensitivity test, different microphysics schemes were used, in addition to different spin-up times. The rain accumulation from December 13, 2018 at 20 UTC to December 14 at 8 UTC from the 3 km resolution models using the NSSL, Morrison, and Thompson aerosol-aware microphysics schemes is shown in Fig. 7.9. A high-resolution 1 km rain map is also shown in Fig. 7.9. This high-resolution simulation was carried out using the Thompson aerosol-aware microphysics. Fig. 7.9 also shows the rain estimate from the ground radars CHIVO, CSAPR, and RMA.

As shown in Fig. 7.9, the rain maps show significant rain from the radars and not much rain from the models near the SdC, close to the radar domains. The rain maps for the different microphysics show a significant amount of rain to the North and South of the SdC instead. The downscaling seems to help better resolve the rain near the east slope of the Sierras. Nevertheless, there is still more rain observed from the radars.

Hovmoller diagrams were also computed to see the evolution in time of the rain. It can be seen in Fig. 7.10 that the Hovmoller diagram from the CHIVO radar captures the back-building process observed in Fig. 7.4. It can also be seen in Fig. 7.10 that the Thompson aerosol-aware microphysics seems to capture this back-building process better.

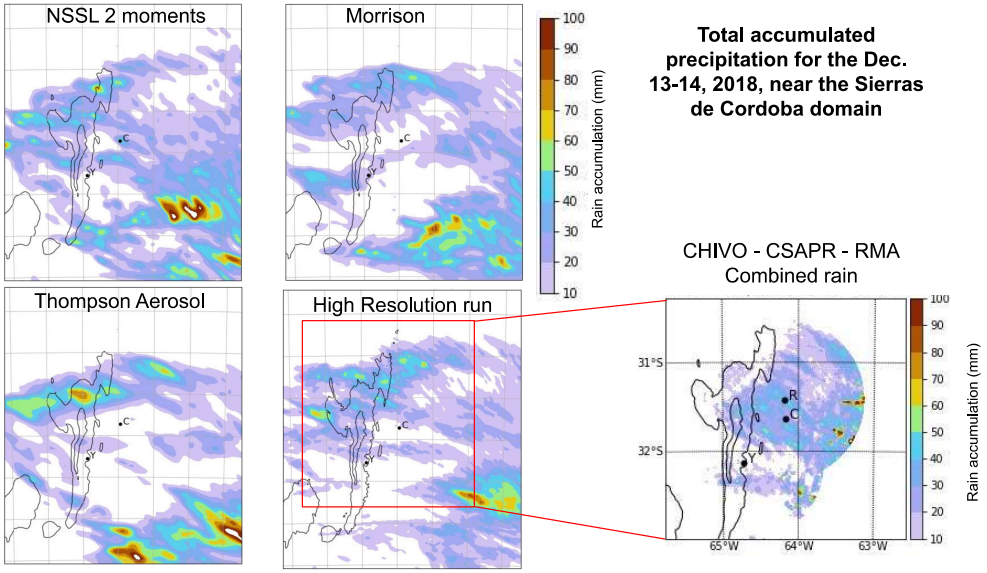

Figure 7.9: Total rain accumulation for the Dec. 14, 2018 case. The four panels to the left are rain accumulation from models, and the panel to the right corresponds to the radar's estimates.

It can also be seen from the Hovmoller diagrams in Fig. 7.10 that the models resolved mostly a storm system passing by the Sierras. However, the radar diagram in the bottom-right panel shows that the system that originates near the Andes passes the SdC from the South without crossing the SdC. New cells initiated around 1:30 UTC and grew very fast and stayed stationary in the same longitudes for a while, producing the significant amount of rain observed for this case. This stationery rain could be explained by a back-building process producing new cells one after another.

The NSSL microphysics seems to capture the rain spatial distribution better in the rain maps in Fig. 7.9 but not the back building in Fig. 7.10. On the other hand, Thompson-aware's microphysics seems to capture the back building but not necessarily the rain spatial distribution. The downscaling of the Thompson aerosol-aware microphysics seems to capture the rain better and reproduce the back-building process observed by the radars.

The Thompson aerosol-aware microphysics was also used to conduct a sensitivity test with different spin-up times. The rain maps from this sensitivity test with the different spin-up times are shown in Fig. 7.11, and the Hovmoller diagrams are shown in Fig. 7.12. As can be seen in Fig. 7.11, the rain near the terrain seems to be better resolved by the models with less spin-up time

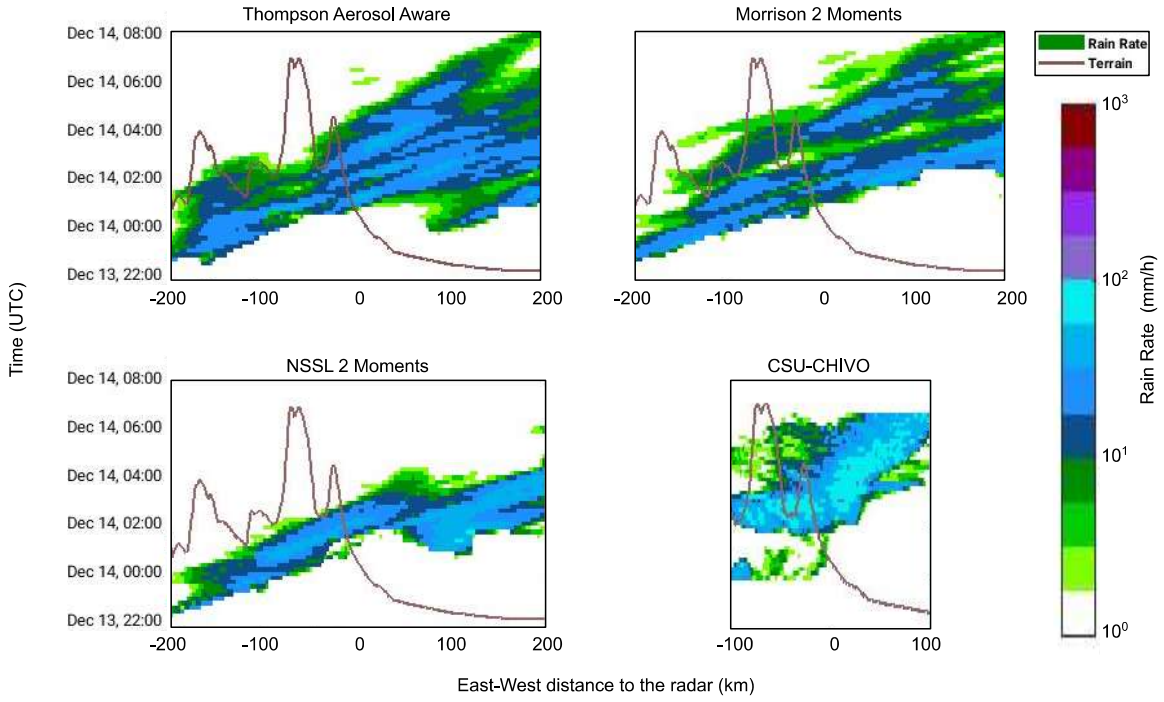

Figure 7.10: Rain rate evolution from Simulations and radar estimation. The vertical intense rain rate shown in the bottom-left panel suggests the initiation of new cells on the eastern slope of the SdC.

(6-hour spin-up time). Although 12-hours is a more standard spin-up time, the closest timing of spin-up before precipitation produces better results for nowcasting and compares better with radar observations (C.Radhakrishnan 2023, personal communication).

The Hovmoller diagrams with the different spin-up times are shown in Fig. 7.12. It can be seen in Fig. 7.12 that the 6-hour spin-up displays a more similar pattern to the rain temporal distribution from the radar. The back-building process seems to be better resolved by the models with 6-hour spin-up.

7.4 Summary

Radar measurements and model simulations were compared for a representative case during the RELAMPAGO field campaign. Various insights can be taken from the comparison conducted in this investigation. Different parameterizations were set in the model simulations to see if these

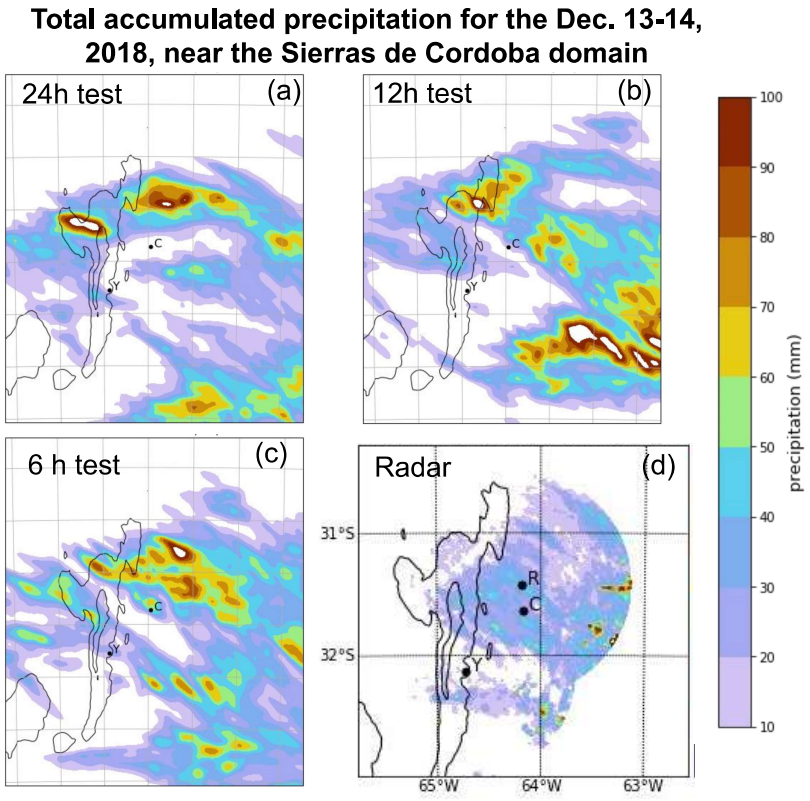

Figure 7.11: Rain accumulation from models (a), (b), and (c). And accumulation from radar rain estimate (d)

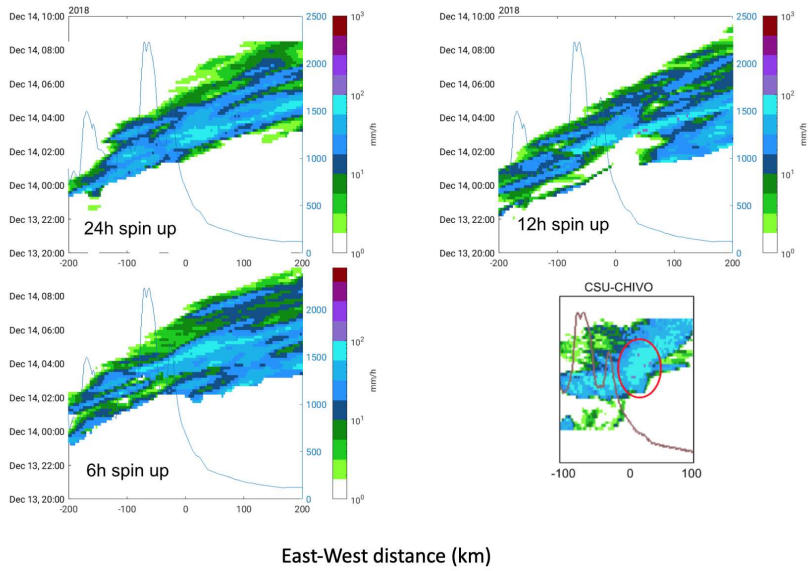

Figure 7.12: Hovmoller diagram showing the rain rate evolution from Simulations and radar estimation.

configurations could better represent the precipitation in this part of South America. Some of the insights from this comparison are:

1. Radar observations show that the interaction of outflows with the terrain produces most of the CI observed in the radar domain. The radar also observed a back-building process. The cold pools from the storms in the East side of the sierras seem to initiate new convection one after another, producing a train of convective lines that generates the significant amount of rain observed for this case. On the other hand, the models resolved mostly one convective system crossing the SdC and upscale growing while moving East.

2. The Thomson aerosol-aware microphysics resolves the back building that was observed from the radar. However, the back-building by this microphysics was resolved differently as the radar observed it. The back-building in the simulations originated on the West slope of the SdC. On the other hand, the train of cells from the radar perspective originated on the Eastern slope of the SdC. Although, the SdC blocked the radar's view on the Western slope and as a result, we were not able to estimate the rain from radars on the Westside of the SdC.

3. Downscaling the resolution of the simulations from 3 km to 1 km helps to better resolve the back-building process in the SdC observed by the radars. At the same time, it helps to represent the spatiotemporal distribution of the rain in complex terrain.

4. A shorter spin-up before precipitation helps the models to represent better the precipitation near complex terrain. A spin-up time of 6 hours seems optimal to better represent the spatiotemporal distribution of rain near complex terrain while allowing the model a reasonable time to warm up.

The radar measurements collected during the RELAMPAGO campaign provide unprecedented high-resolution observations of some of the tallest storms in South America and the world. These radar data allow us to observe in detail the evolution of one of the campaign representative cases. Simulations of this case show a good representation of this case storm system on a large scale.

However, the simulations represent differently the spatiotemporal distribution of convective precipitation observed by radars on a microscale. The results of this study can be used to point out some of the convective processes that the models are challenged to resolve in this region. We expect that this observational and modeling study will contribute to producing a better representation of storms in South America in the future.

Chapter 8

Dissertation Summary

8.1 Summary

In this dissertation, the network of radars deployed during the RELAMPAGO campaign is used to study microphysical processes occurring in convective storms. This radar network analysis is performed to understand how multiple radar retrieval can be used to understand better convective precipitation. Some of the key points of this dissertation work are summarized in this chapter.

First, a cross-validation of the network of C-band radars with GPM was conducted. The radars in the network were compared to each other. A novel method to self-calibrate the measurements as a radar network was developed. Some of the key points from the cross-validation of the network of C-band radar with GPM are: In order to use cross-calibration between radars in conjunction with attenuation correction, a locally precise attenuation correction must be done. A generic correction process is not accurate enough for cross-calibrating radars. The bias between KuPR and the GRs reduces when the locally tuned attenuation coefficients are used to correct attenuation.

The radar signal attenuation in melting ice was estimated from radar observations. Experimental data to estimate the attenuation in melting ice is very rare. This is perhaps the first time that the attenuation of melting ice is obtained from observations. Some of the key points from measuring the attenuation of melting ice from the network of C-band radars are: The attenuation of melting ice in the C-band was obtained using a network-based approach. The simultaneous radar observations from CHIVO and CSAPR were used to obtain an estimate of the attenuation using the principle of self-consistency. The attenuation and the differential attenuation was computed for many radar bins that propagated through melting ice from both of the radars. The above procedure was validated by comparison with ground disdrometer observations using simple propagation equations in rain regions. The melting ice attenuation correction coefficients in the C-band deter-

mined experimentally in this thesis compared well with the coefficients in the literature obtained from electromagnetic scattering simulations.

Another important contribution in this dissertation is the analysis of mixed-phase precipitation using spectral polarimetry. Computing polarimetric spectra in this environment is challenging due to the turbulence, mixed phases, and high noise the estimates can experience. Various spectral processing techniques were used to enhance the quality of the spectrum in an updraft environment. In addition, the microphysical inference using dual-polarization processing is presented. Dual polarization spectral decomposition reveals how the spectrum is dispersed in the mixed-phase region where updrafts exist.

Radar measurements and model simulations were compared for a representative case during the RELAMPAGO field campaign. Different parameterizations were set in the model simulations to see if these configurations could better represent the precipitation in this part of South America.

The network of radars deployed during the RELAMPAGO campaign captured in detail some of the tallest storms in South America and the world. The storms observed during the campaign produced severe weather on the ground in the form of significant amounts of hail and heavy rain. The RELAMPAGO radar dataset allows us to have a detailed look into the microphysics of storms in South America and understand practical considerations of radar measurement in this region. We expect that the work presented in this dissertation contributes to the development of the radar field in South America.

8.2 Future work

Electromagnetic scattering simulations of melting ice and hail are proposed as future work to support the experimental observations. Scattering simulation of in-situ observations can be compared with radar measurements. In addition, more cases will be used to study the radar signal attenuation in melting ice. Dual polarization spectral decomposition can be analyzed for more cases in updraft environments. More cases with different microphysical diversity, especially graupel can be analyzed and compared with GPM.

Bibliography

[1] Kristen Rasmussen, Angela Rowe, Deanna Hence, and Paola Salio. RELAMPAGO Science Summary for 13 December 2018, 2018.

[2] Alexander V Ryzhkov, Matthew R Kumjian, Scott M Ganson, and Pengfei Zhang. Polarimetric radar characteristics of melting hail. Part II: Practical implications. *Journal of Applied Meteorology and Climatology*, 52(12):2871–2886, 2013.

[3] L Borowska, A Ryzhkov, D Zrnić, C Simmer, and R Palmer. Attenuation and differential attenuation of 5-cm-wavelength radiation in melting hail. *Journal of Applied Meteorology and Climatology*, 50(1):59–76, 2011.

[4] National Research Council et al. *Weather radar technology beyond NEXRAD*. National Academies Press, 2002.

[5] AV Ryzhkov and DS Zrnic. Radar polarimetry at S, C, and X bands: Comparative analysis and operational implications, paper presented at 32nd Conference on Radar Meteorology. *Am. Meteorol. Soc., Norman, Okla*, 2005.

[6] World Meteorological Organization. Weather radar database, 2023.

[7] I. Arias and V. Chandrasekar. Cross Validation of GPM and Ground-Based Radar in Latin America and the Caribbean. In *IGARSS 2018 - 2018 IEEE International Geoscience and Remote Sensing Symposium*, pages 3891–3893, July 2018.

[8] D. S. Zrnic. S, C, and X Bands For Weather Surveillance. Technical report, NOAA/NSSL, 2017.

[9] Viswanathan N Bringi, TD Keenan, and V Chandrasekar. Correcting C-band radar reflectivity and differential reflectivity data for rain attenuation: A self-consistent method with constraints. *IEEE transactions on geoscience and remote sensing*, 39(9):1906–1915, 2001.

[10] Lawrence D Carey, Steven A Rutledge, David A Ahijevych, and Tom D Keenan. Correcting propagation effects in C-band polarimetric radar observations of tropical convection using differential propagation phase. *Journal of Applied Meteorology and Climatology*, 39(9):1405–1433, 2000.

[11] VN Bringi and V Chandrasekar. *Polarimetric Doppler weather radar: principles and applications*. Cambridge university press, 2001.

[12] V Chandrasekar, Robert M Beauchamp, and Renzo Bechini. *Introduction to Dual Polarization Weather Radar: Fundamentals, Applications, and Networks*. Cambridge University Press, 2023.

[13] TD Keenan, LD Carey, DS Zrnić, and PT May. Sensitivity of 5-cm wavelength polarimetric radar variables to raindrop axial ratio and drop size distribution. *Journal of Applied Meteorology*, 40(3):526–545, 2001.

[14] Eugenio Gorgucci and Luca Baldini. Attenuation and differential attenuation correction of C-band radar observations using a fully self-consistent methodology. *IEEE Geoscience and Remote Sensing Letters*, 4(2):326–330, 2007.

[15] Steven J Goodman, Richard J Blakeslee, William J Koshak, Douglas Mach, Jeffrey Bailey, Dennis Buechler, Larry Carey, Chris Schultz, Monte Bateman, Eugene McCaul Jr, et al. The GOES-R geostationary lightning mapper (GLM). *Atmospheric research*, 125:34–49, 2013.

[16] Kristen L Rasmussen, Stella L Choi, Manuel D Zuluaga, and Robert A Houze. TRMM precipitation bias in extreme storms in South America. *Geophysical Research Letters*, 40(13):3457–3461, 2013.

[17] Merrill Ivan Skolnik. Introduction to radar systems. *New York*, 1980.

[18] Grant William Petty. *A first course in atmospheric radiation*. Sundog Pub, 2006.

[19] V Chandrasekar, Luca Baldini, Nitin Bharadwaj, and Paul L Smith. Calibration procedures for global precipitation-measurement ground-validation radars. *URSI Radio Science Bulletin*, 2015(355):45–73, 2015.

[20] I Skolnik Merrill et al. Introduction to radar systems. *Mc Grow-Hill*, 7(10), 2001.

[21] Yanting Wang, V Chandrasekar, and Brenda Dolan. Development of scan strategy for dual Doppler retrieval in a networked radar system. In *IGARSS 2008-2008 IEEE International Geoscience and Remote Sensing Symposium*, volume 5, pages V–322. IEEE, 2008.

[22] Alan Shapiro, Corey K Potvin, and Jidong Gao. Use of a vertical vorticity equation in variational dual-Doppler wind analysis. *Journal of Atmospheric and Oceanic Technology*, 26(10):2089–2106, 2009.

[23] N Moisseev Dmitri. Differential reflectivity calibration without using vertical incidence observations. In *33rd Conference on Radar Meteorology*, 2007.

[24] Yadong Wang, Tian-You Yu, Alexander V Ryzhkov, and Matthew R Kumjian. Application of spectral polarimetry to a hailstorm at low elevation angle. *Journal of Atmospheric and Oceanic Technology*, 36(4):567–583, 2019.

[25] K Widener and N Bharadwaj. *C-Band Scanning ARM Precipitation Radar (C-SAPR) Handbook*. DOE/SC-ARM/TR-121, 2002.

[26] Edward J Zipser, Daniel J Cecil, Chuntao Liu, Stephen W Nesbitt, and David P Yorty. Where are the most intense thunderstorms on Earth? *Bull. Amer. Meteor. Soc.*, 87(8):1057–1072, 2006.

[27] Christian Kummerow, William Barnes, Toshiaki Kozu, James Shiue, and Joanne Simpson. The tropical rainfall measuring mission (TRMM) sensor package. *J. Atmos. Oceanic Technol.*, 15(3):809–817, 1998.

[28] Kristen L Rasmussen and Robert A Houze. Orogenic convection in subtropical South America as seen by the TRMM satellite. *Mon. Wea. Rev.*, 139(8):2399–2420, 2011.

[29] Toshiaki Kozu, Toneo Kawanishi, Hiroshi Kuroiwa, Masahiro Kojima, Koki Oikawa, Hiroshi Kumagai, Ken'ichi Okamoto, Minoru Okumura, Hirotaka Nakatsuka, and Katsuhiko Nishikawa. Development of precipitation radar onboard the Tropical Rainfall Measuring Mission (TRMM) satellite. *IEEE Trans. Geosci. Remote Sens.*, 39(1):102–116, 2001.

[30] Kristen L Rasmussen and Robert A Houze. Convective initiation near the Andes in subtropical South America. *Mon. Wea. Rev.*, 144(6):2351–2374, 2016.

[31] Gail Skofronick-Jackson, Walter A Petersen, Wesley Berg, Chris Kidd, Erich F Stocker, Dalia B Kirschbaum, Ramesh Kakar, Scott A Braun, George J Huffman, Toshio Iguchi, et al. The Global Precipitation Measurement (GPM) mission for science and society. *Bull. Amer. Meteor. Soc.*, 98(8):1679–1695, 2017.

[32] Arthur Y Hou, Ramesh K Kakar, Steven Neeck, Ardeshir A Azarbarzin, Christian D Kummerow, Masahiro Kojima, Riko Oki, Kenji Nakamura, and Toshio Iguchi. The global precipitation measurement mission. *Bull. Amer. Meteor. Soc.*, 95(5):701–722, 2014.

[33] M Kojima, T Miura, K Furukawa, Y Hyakusoku, T Ishikiri, H Kai, T Iguchi, H Hanado, and K Nakagawa. Dual-frequency precipitation radar (DPR) development on the global precipitation measurement (GPM) core observatory. In *Earth observing missions and sensors: Development, implementation, and characterization II*, volume 8528, page 85281A. International Society for Optics and Photonics, 2012.

[34] Toshio Iguchi. Dual-Frequency Precipitation Radar (DPR) on the Global Precipitation Measurement. *Satellite Precipitation Measurement: Volume 1*, 67:183, 2020.

[35] Takeshi Masaki, Toshio Iguchi, Kaya Kanemaru, Kinji Furukawa, Naofumi Yoshida, Takuji Kubota, and Riko Oki. Calibration of the dual-frequency precipitation radar onboard the

Global Precipitation Measurement Core Observatory. *IEEE Trans. Geosci. Remote Sens.*, 2020.

[36] Shinta Seto, Toshio Iguchi, Robert Meneghini, Jun Awaka, Takuji Kubota, Takeshi Masaki, and Nobuhiro Takahashi. The precipitation rate retrieval algorithms for the GPM Dual-frequency Precipitation Radar. *J. Meteor. Soc. Japan*, 99(2):205–237, 2021.

[37] Mary Jane Bartholomew. Two-Dimensional Video Disdrometer (VDIS) Instrument Handbook. Technical report, DOE Office of Science Atmospheric Radiation Measurement (ARM) Program, 18., 2020.

[38] Kaya Kanemaru, Toshio Iguchi, Takeshi Masaki, and Takuji Kubota. Estimates of Spaceborne Precipitation Radar Pulsewidth and Beamwidth Using Sea Surface Echo Data. *IEEE Trans. Geosci. Remote Sens.*, 58(8):5291–5303, 2020.

[39] Steven M Bolen and V Chandrasekar. Methodology for aligning and comparing spaceborne radar and ground-based radar observations. *J. Atmos. Oceanic Technol.*, 20(5):647–659, 2003.

[40] Steven M Bolen and V Chandrasekar. Quantitative cross validation of space-based and ground-based radar observations. *J. Appl. Meteor.*, 39(12):2071–2079, 2000.

[41] Emmanouil N Anagnostou, Carlos A Morales, and Tufa Dinku. The use of TRMM precipitation radar observations in determining ground radar calibration biases. *J. Atmos. Oceanic Technol.*, 18(4):616–628, 2001.

[42] Mathew R Schwaller and K Robert Morris. A ground validation network for the global precipitation measurement mission. *J. Atmos. Oceanic Technol.*, 28(3):301–319, 2011.

[43] Sounak Kumar Biswas and V Chandrasekar. Cross-validation of observations between the GPM dual-frequency precipitation radar and ground based dual-polarization radars. *Remote Sens.*, 10(11):1773, 2018.

[44] Robert A Warren, Alain Protat, Steven T Siems, Hamish A Ramsay, Valentin Louf, Michael J Manton, and Thomas A Kane. Calibrating ground-based radars against TRMM and GPM. *J. Atmos. Oceanic Technol.*, 35(2):323–346, 2018.

[45] Valentin Louf, Alain Protat, Robert A Warren, Scott M Collis, David B Wolff, Surendra Raunyiar, Christian Jakob, and Walter A Petersen. An integrated approach to weather radar calibration and monitoring using ground clutter and satellite comparisons. *J. Atmos. Oceanic Technol.*, 36(1):17–39, 2019.

[46] Lina Esther Rivelli Zea. RELAMPAGO-CACTI drop size distribution observations and the implications for cloud and hydrologic studies. Master's thesis, Univeristy of Illinois, 52, 2020.

[47] Matthew R Kumjian, Alexander P Khain, Nir Benmoshe, Eyal Ilotoviz, Alexander V Ryzhkov, and Vaughan TJ Phillips. The anatomy and physics of Z DR columns: Investigating a polarimetric radar signature with a spectral bin microphysical model. *Journal of Applied Meteorology and Climatology*, 53(7):1820–1843, 2014.

[48] RM Rasmussen, V Levizzani, and HR Pruppacher. A wind tunnel and theoretical study on the melting behavior of atmospheric ice particles: III. Experiment and theory for spherical ice particles of radius> 500 μm. *Journal of Atmospheric Sciences*, 41(3):381–388, 1984.

[49] Charles A Knight and Kevin R Knupp. Precipitation growth trajectories in a CCOPE storm. *Journal of Atmospheric Sciences*, 43(11):1057–1073, 1986.

[50] Ji-Young Gu, A Ryzhkov, P Zhang, P Neilley, M Knight, B Wolf, and Dong-In Lee. Polarimetric attenuation correction in heavy rain at C-band. *Journal of Applied Meteorology and Climatology*, 50(1):39–58, 2011.

[51] Rudolf Kaltenboeck and Alexander Ryzhkov. Comparison of polarimetric signatures of hail at S and C bands for different hail sizes. *Atmospheric Research*, 123:323–336, 2013.

[52] Laurent Féral, Henri Sauvageot, and Serge Soula. Hail detection using S-and C-band radar reflectivity difference. *Journal of Atmospheric and Oceanic Technology*, 20(2):233–248, 2003.

[53] Alexander V Ryzhkov, Matthew R Kumjian, Scott M Ganson, and Alexander P Khain. Polarimetric radar characteristics of melting hail. Part I: Theoretical simulations using spectral microphysical modeling. *Journal of Applied Meteorology and Climatology*, 52(12):2849–2870, 2013.

[54] V Chandrasekar and S Lim. Retrieval of reflectivity in a networked radar environment. *Journal of Atmospheric and Oceanic Technology*, 25(10):1755–1767, 2008.

[55] Ivan Arias and V Chandrasekar. Cross validation of the network of ground-based radar with GPM during the Remote sensing of Electrification, Lightning, And Mesoscale/microscale Processes with Adaptive Ground Observations (RELAMPAGO) field campaign. *Journal of the Meteorological Society of Japan. Ser. II*, 2021.

[56] Robert Jackson, Scott Collis, Timothy Lang, Corey Potvin, and Todd Munson. PyDDA: a pythonic direct data assimilation framework for wind retrievals. *Journal of Open Research Software*, 8(8), 2020.

[57] Corey K Potvin, Alan Shapiro, and Ming Xue. Impact of a vertical vorticity constraint in variational dual-Doppler wind analysis: Tests with real and simulated supercell data. *Journal of Atmospheric and Oceanic Technology*, 29(1):32–49, 2012.

[58] Stephen W Nesbitt, Paola V Salio, Eldo Ávila, Phillip Bitzer, Lawrence Carey, V Chandrasekar, Wiebke Deierling, Francina Dominguez, Maria Eugenia Dillon, C Marcelo Garcia, et al. A storm safari in subtropical South America: Proyecto RELAMPAGO. *Bulletin of the American Meteorological Society*, 102(8):E1621–E1644, 2021.

[59] Ivan Arias, V Chandrasekar, and Angela Rowe. Dual radar time sequence observation of convective initiation over sierras de cordoba during relampago field campaign, dec 13-14 case. In *19th Conference on Mountain Meteorology*. AMS, 2020.

[60] Renzo Bechini and V Chandrasekar. A semisupervised robust hydrometeor classification method for dual-polarization radar applications. *Journal of Atmospheric and Oceanic Technology*, 32(1):22–47, 2015.

[61] Dmitri N Moisseev and V Chandrasekar. Polarimetric spectral filter for adaptive clutter and noise suppression. *Journal of Atmospheric and Oceanic Technology*, 26(2):215–228, 2009.

[62] Laura Alku, Dmitri Moisseev, Tuomas Aittomäki, and V Chandrasekar. Identification and suppression of nonmeteorological echoes using spectral polarimetric processing. *IEEE Transactions on Geoscience and Remote Sensing*, 53(7):3628–3638, 2015.

[63] Jiapeng Yin, Haonan Chen, Yongzhen Li, and Xuesong Wang. Clutter mitigation based on spectral depolarization ratio for dual-polarization weather radars. *IEEE Journal of Selected Topics in Applied Earth Observations and Remote Sensing*, 14:6131–6145, 2021.

[64] Sounak Kumar Biswas, V Chandrasekar, Swaroop Sahoo, and Aiswarya K Lakshmi. Study of a Convective Event During the Relampago Field Experiment Using Spectral Polarimetry. In *IGARSS 2022-2022 IEEE International Geoscience and Remote Sensing Symposium*, pages 6534–6537. IEEE, 2022.

[65] Tian-You Yu, Xiao Xiao, and Yadong Wang. Statistical quality of spectral polarimetric variables for weather radar. *Journal of Atmospheric and Oceanic Technology*, 29(9):1221–1235, 2012.

[66] Henry Stark, John William Woods, B Thilaka, and Ashutosh Kumar. *Probability, statistics, and random processes for engineers*, volume 76. Pearson Upper Saddle River, 2012.

[67] Alan V Oppenheim, Ronald W Schafer, and Hohn R Back. "Discrete Time Signal Processing", Pearson Education, 2005., 2015.

[68] Amit Dutta. *Advanced Spectral Processing for Dual Polarization Weather Radars*. PhD thesis, Colorado State University, 2020.

[69] Marquette N Rocque and Kristen L Rasmussen. The Impact of Topography on the Environment and Life Cycle of Weakly and Strongly Forced MCSs during RELAMPAGO. *Monthly Weather Review*, 150(9):2317–2338, 2022.

[70] Haonan Chen, V Chandrasekar, and Renzo Bechini. An improved dual-polarization radar rainfall algorithm (DROPS2. 0): Application in NASA IFloodS field campaign. *Journal of Hydrometeorology*, 18(4):917–937, 2017.

[71] Gregory Thompson and Trude Eidhammer. A study of aerosol impacts on clouds and precipitation development in a large winter cyclone. *Journal of the atmospheric sciences*, 71(10):3636–3658, 2014.

[72] Edward R Mansell, Conrad L Ziegler, and Eric C Bruning. Simulated electrification of a small thunderstorm with two-moment bulk microphysics. *Journal of the Atmospheric Sciences*, 67(1):171–194, 2010.

[73] Hugh Morrison, Gregory Thompson, and V Tatarskii. Impact of cloud microphysics on the development of trailing stratiform precipitation in a simulated squall line: Comparison of one-and two-moment schemes. *Monthly weather review*, 137(3):991–1007, 2009.

[74] Gimena Casaretto, Maria Eugenia Dillon, Paola Salio, Yanina Garcia Skabar, Stephen W Nesbitt, Russ S Schumacher, Carlos Marcelo Garcia, and Carlos Catalini. High-resolution NWP forecast precipitation comparison over complex terrain of the Sierras de Cordoba during RELAMPAGO-CACTI. *Weather and Forecasting*, 37(2):241–266, 2022.